

**Precise measurement of the  $e^+e^- \rightarrow \pi^+\pi^-(\gamma)$  cross section with the initial-state radiation method at *BABAR***

- J. P. Lees,<sup>1</sup> V. Poireau,<sup>1</sup> V. Tisserand,<sup>1</sup> J. Garra Tico,<sup>2</sup> E. Grauges,<sup>2</sup> A. Palano,<sup>3a,3b</sup> G. Eigen,<sup>4</sup> B. Stugu,<sup>4</sup> D. N. Brown,<sup>5</sup> L. T. Kerth,<sup>5</sup> Yu. G. Kolomensky,<sup>5</sup> G. Lynch,<sup>5</sup> H. Koch,<sup>6</sup> T. Schroeder,<sup>6</sup> D. J. Asgeirsson,<sup>7</sup> C. Hearty,<sup>7</sup> T. S. Mattison,<sup>7</sup> J. A. McKenna,<sup>7</sup> A. Khan,<sup>8</sup> V. E. Blinov,<sup>9</sup> A. R. Buzykaev,<sup>9</sup> V. P. Druzhinin,<sup>9</sup> V. B. Golubev,<sup>9</sup> E. A. Kravchenko,<sup>9</sup> A. P. Onuchin,<sup>9</sup> S. I. Serednyakov,<sup>9</sup> Yu. I. Skovpen,<sup>9</sup> E. P. Solodov,<sup>9</sup> K. Yu. Todyshev,<sup>9</sup> A. N. Yushkov,<sup>9</sup> M. Bondioli,<sup>10</sup> D. Kirkby,<sup>10</sup> A. J. Lankford,<sup>10</sup> M. Mandelkern,<sup>10</sup> H. Atmacan,<sup>11</sup> J. W. Gary,<sup>11</sup> F. Liu,<sup>11</sup> O. Long,<sup>11</sup> G. M. Vitug,<sup>11</sup> C. Campagnari,<sup>12</sup> T. M. Hong,<sup>12</sup> D. Kovalskyi,<sup>12</sup> J. D. Richman,<sup>12</sup> C. A. West,<sup>12</sup> A. M. Eisner,<sup>13</sup> J. Kroseberg,<sup>13</sup> W. S. Lockman,<sup>13</sup> A. J. Martinez,<sup>13</sup> B. A. Schumm,<sup>13</sup> A. Seiden,<sup>13</sup> D. S. Chao,<sup>14</sup> C. H. Cheng,<sup>14</sup> B. Echenard,<sup>14</sup> K. T. Flood,<sup>14</sup> D. G. Hitlin,<sup>14</sup> P. Ongmongkolkul,<sup>14</sup> F. C. Porter,<sup>14</sup> A. Y. Rakitin,<sup>14</sup> R. Andreassen,<sup>15</sup> Z. Huard,<sup>15</sup> B. T. Meadows,<sup>15</sup> M. D. Sokoloff,<sup>15</sup> L. Sun,<sup>15</sup> P. C. Bloom,<sup>16</sup> W. T. Ford,<sup>16</sup> A. Gaz,<sup>16</sup> U. Nauenberg,<sup>16</sup> J. G. Smith,<sup>16</sup> S. R. Wagner,<sup>16</sup> R. Ayad,<sup>17</sup><sup>†</sup> W. H. Toki,<sup>17</sup> B. Spaan,<sup>18</sup> K. R. Schubert,<sup>19</sup> R. Schwierz,<sup>19</sup> D. Bernard,<sup>20</sup> M. Verderi,<sup>20</sup> P. J. Clark,<sup>21</sup> S. Playfer,<sup>21</sup> D. Bettoni,<sup>22a</sup> C. Bozzi,<sup>22a</sup> R. Calabrese,<sup>22a,22b</sup> G. Cibinetto,<sup>22a,22b</sup> E. Fioravanti,<sup>22a,22b</sup> I. Garzia,<sup>22a,22b</sup> E. Luppi,<sup>22a,22b</sup> M. Munerato,<sup>22a,22b</sup> M. Negrini,<sup>22a,22b</sup> L. Piemontese,<sup>22a</sup> V. Santoro,<sup>22a</sup> R. Baldini-Ferroli,<sup>23</sup> A. Calcaterra,<sup>23</sup> R. de Sangro,<sup>23</sup> G. Finocchiaro,<sup>23</sup> P. Patteri,<sup>23</sup> I. M. Peruzzi,<sup>23</sup><sup>‡</sup> M. Piccolo,<sup>23</sup> M. Rama,<sup>23</sup> A. Zallo,<sup>23</sup> R. Contri,<sup>24a,24b</sup> E. Guido,<sup>24a,24b</sup> M. Lo Vetere,<sup>24a,24b</sup> M. R. Monge,<sup>24a,24b</sup> S. Passaggio,<sup>24a</sup> C. Patrignani,<sup>24a,24b</sup> E. Robutti,<sup>24a</sup> B. Bhuyan,<sup>25</sup> V. Prasad,<sup>25</sup> C. L. Lee,<sup>26</sup> M. Morii,<sup>26</sup> A. J. Edwards,<sup>27</sup> A. Adametz,<sup>28</sup> U. Uwer,<sup>28</sup> H. M. Lacker,<sup>29</sup> T. Lueck,<sup>29</sup> P. D. Dauncey,<sup>30</sup> P. K. Behera,<sup>31</sup> U. Mallik,<sup>31</sup> C. Chen,<sup>32</sup> J. Cochran,<sup>32</sup> W. T. Meyer,<sup>32</sup> S. Prell,<sup>32</sup> A. E. Rubin,<sup>32</sup> A. V. Gritsan,<sup>33</sup> Z. J. Guo,<sup>33</sup> N. Arnaud,<sup>34</sup> M. Davier,<sup>34</sup> D. Derkach,<sup>34</sup> G. Grosdidier,<sup>34</sup> F. Le Diberder,<sup>34</sup> A. M. Lutz,<sup>34</sup> B. Malaescu,<sup>34</sup> P. Roudeau,<sup>34</sup> M. H. Schune,<sup>34</sup> A. Stocchi,<sup>34</sup> L. L. Wang,<sup>34,§</sup> G. Wormser,<sup>34</sup> D. J. Lange,<sup>35</sup> D. M. Wright,<sup>35</sup> C. A. Chavez,<sup>36</sup> J. P. Coleman,<sup>36</sup> J. R. Fry,<sup>36</sup> E. Gabathuler,<sup>36</sup> D. E. Hutchcroft,<sup>36</sup> D. J. Payne,<sup>36</sup> C. Touramanis,<sup>36</sup> A. J. Bevan,<sup>37</sup> F. Di Lodovico,<sup>37</sup> R. Sacco,<sup>37</sup> M. Sigamani,<sup>37</sup> G. Cowan,<sup>38</sup> D. N. Brown,<sup>39</sup> C. L. Davis,<sup>39</sup> A. G. Denig,<sup>40</sup> M. Fritsch,<sup>40</sup> W. Grndl,<sup>40</sup> K. Griessinger,<sup>40</sup> A. Hafner,<sup>40</sup> E. Prencipe,<sup>40</sup> R. J. Barlow,<sup>41,||</sup> G. Jackson,<sup>41</sup> G. D. Lafferty,<sup>41</sup> E. Behn,<sup>42</sup> R. Cenci,<sup>42</sup> B. Hamilton,<sup>42</sup> A. Jawahery,<sup>42</sup> D. A. Roberts,<sup>42</sup> C. Dallapiccola,<sup>43</sup> R. Cowan,<sup>44</sup> D. Dujmic,<sup>44</sup> G. Sciolla,<sup>44</sup> R. Cheaib,<sup>45</sup> D. Lindemann,<sup>45</sup> P. M. Patel,<sup>45</sup> S. H. Robertson,<sup>45</sup> P. Biassoni,<sup>46a,46b</sup> N. Neri,<sup>46a</sup> F. Palombo,<sup>46a,46b</sup> S. Stracka,<sup>46a,46b</sup> L. Cremaldi,<sup>47</sup> R. Godang,<sup>47,¶</sup> R. Kroeger,<sup>47</sup> P. Sonnek,<sup>47</sup> D. J. Summers,<sup>47</sup> X. Nguyen,<sup>48</sup> M. Simard,<sup>48</sup> P. Taras,<sup>48</sup> G. De Nardo,<sup>49a,49b</sup> D. Monorchio,<sup>49a,49b</sup> G. Onorato,<sup>49a,49b</sup> C. Sciacca,<sup>49a,49b</sup> M. Martinelli,<sup>50</sup> G. Raven,<sup>50</sup> C. P. Jessop,<sup>51</sup> J. M. LoSecco,<sup>51</sup> W. F. Wang,<sup>51</sup> K. Honscheid,<sup>52</sup> R. Kass,<sup>52</sup> J. Brau,<sup>53</sup> R. Frey,<sup>53</sup> N. B. Sinev,<sup>53</sup> D. Strom,<sup>53</sup> E. Torrence,<sup>53</sup> E. Feltresi,<sup>54a,54b</sup> N. Gagliardi,<sup>54a,54b</sup> M. Margoni,<sup>54a,54b</sup> M. Morandin,<sup>54a</sup> M. Posocco,<sup>54a</sup> M. Rotondo,<sup>54a</sup> G. Simi,<sup>54a</sup> F. Simonetto,<sup>54a,54b</sup> R. Stroili,<sup>54a,54b</sup> S. Akar,<sup>55</sup> E. Ben-Haim,<sup>55</sup> M. Bomben,<sup>55</sup> G. R. Bonneau,<sup>55</sup> H. Briand,<sup>55</sup> G. Calderini,<sup>55</sup> J. Chauveau,<sup>55</sup> O. Hamon,<sup>55</sup> Ph. Leruste,<sup>55</sup> G. Marchiori,<sup>55</sup> J. Ocariz,<sup>55</sup> S. Sitt,<sup>55</sup> M. Biasini,<sup>56a,56b</sup> E. Manoni,<sup>56a,56b</sup> S. Pacetti,<sup>56a,56b</sup> A. Rossi,<sup>56a,56b</sup> C. Angelini,<sup>57a,57b</sup> G. Batignani,<sup>57a,57b</sup> S. Bettarini,<sup>57a,57b</sup> M. Carpinelli,<sup>57a,57b,\*\*</sup> G. Casarosa,<sup>57a,57b</sup> A. Cervelli,<sup>57a,57b</sup> F. Forti,<sup>57a,57b</sup> M. A. Giorgi,<sup>57a,57b</sup> A. Lusiani,<sup>57a,57c</sup> B. Oberhof,<sup>57a,57b</sup> E. Paoloni,<sup>57a,57b</sup> A. Perez,<sup>57a</sup> G. Rizzo,<sup>57a,57b</sup> J. J. Walsh,<sup>57a</sup> D. Lopes Pegna,<sup>58</sup> J. Olsen,<sup>58</sup> A. J. S. Smith,<sup>58</sup> A. V. Telnov,<sup>58</sup> F. Anulli,<sup>59a</sup> R. Faccini,<sup>59a,59b</sup> F. Ferrarotto,<sup>59a</sup> F. Ferroni,<sup>59a,59b</sup> M. Gaspero,<sup>59a,59b</sup> L. Li Gioi,<sup>59a</sup> M. A. Mazzoni,<sup>59a</sup> G. Piredda,<sup>59a</sup> C. Bünger,<sup>60</sup> O. Grünberg,<sup>60</sup> T. Hartmann,<sup>60</sup> T. Leddig,<sup>60</sup> H. Schröder,<sup>60,\*</sup> C. Voss,<sup>60</sup> R. Waldi,<sup>60</sup> T. Adye,<sup>61</sup> E. O. Olaiya,<sup>61</sup> F. F. Wilson,<sup>61</sup> S. Emery,<sup>62</sup> G. Hamel de Monchenault,<sup>62</sup> G. Vasseur,<sup>62</sup> Ch. Yèche,<sup>62</sup> D. Aston,<sup>63</sup> D. J. Bard,<sup>63</sup> R. Bartoldus,<sup>63</sup> J. F. Benitez,<sup>63</sup> C. Cartaro,<sup>63</sup> M. R. Convery,<sup>63</sup> J. Dorfan,<sup>63</sup> G. P. Dubois-Felsmann,<sup>63</sup> W. Dunwoodie,<sup>63</sup> M. Ebert,<sup>63</sup> R. C. Field,<sup>63</sup> M. Franco Sevilla,<sup>63</sup> B. G. Fulsom,<sup>63</sup> A. M. Gabareen,<sup>63</sup> M. T. Graham,<sup>63</sup> P. Grenier,<sup>63</sup> C. Hast,<sup>63</sup> W. R. Innes,<sup>63</sup> M. H. Kelsey,<sup>63</sup> P. Kim,<sup>63</sup> M. L. Kocijan,<sup>63</sup> D. W. G. S. Leith,<sup>63</sup> P. Lewis,<sup>63</sup> B. Lindquist,<sup>63</sup> S. Luitz,<sup>63</sup> V. Luth,<sup>63</sup> H. L. Lynch,<sup>63</sup> D. B. MacFarlane,<sup>63</sup> D. R. Muller,<sup>63</sup> H. Neal,<sup>63</sup> S. Nelson,<sup>63</sup> M. Perl,<sup>63</sup> T. Pulliam,<sup>63</sup> B. N. Ratcliff,<sup>63</sup> A. Roodman,<sup>63</sup> A. A. Salnikov,<sup>63</sup> R. H. Schindler,<sup>63</sup> A. Snyder,<sup>63</sup> D. Su,<sup>63</sup> M. K. Sullivan,<sup>63</sup> J. Va'vra,<sup>63</sup> A. P. Wagner,<sup>63</sup> W. J. Wisniewski,<sup>63</sup> M. Wittgen,<sup>63</sup> D. H. Wright,<sup>63</sup> H. W. Wulsen,<sup>63</sup> C. C. Young,<sup>63</sup> V. Ziegler,<sup>63</sup> W. Park,<sup>64</sup> M. V. Purohit,<sup>64</sup> R. M. White,<sup>64</sup> J. R. Wilson,<sup>64</sup> A. Randle-Conde,<sup>65</sup> S. J. Sekula,<sup>65</sup> M. Bellis,<sup>66</sup> P. R. Burchat,<sup>66</sup> T. S. Miyashita,<sup>66</sup> M. S. Alam,<sup>67</sup> J. A. Ernst,<sup>67</sup> R. Gorodeisky,<sup>68</sup> N. Guttman,<sup>68</sup> D. R. Peimer,<sup>68</sup> A. Soffer,<sup>68</sup> P. Lund,<sup>69</sup> S. M. Spanier,<sup>69</sup> J. L. Ritchie,<sup>70</sup> A. M. Ruland,<sup>70</sup> R. F. Schwitters,<sup>70</sup> B. C. Wray,<sup>70</sup> J. M. Izzen,<sup>71</sup> X. C. Lou,<sup>71</sup> F. Bianchi,<sup>72a,72b</sup> D. Gamba,<sup>72a,72b</sup> L. Lanceri,<sup>73a,73b</sup> L. Vitale,<sup>73a,73b</sup> F. Martinez-Vidal,<sup>74</sup>

A. Oyanguren,<sup>74</sup> H. Ahmed,<sup>75</sup> J. Albert,<sup>75</sup> Sw. Banerjee,<sup>75</sup> F. U. Bernlochner,<sup>75</sup> H. H. F. Choi,<sup>75</sup> G. J. King,<sup>75</sup>  
 R. Kowalewski,<sup>75</sup> M. J. Lewczuk,<sup>75</sup> I. M. Nugent,<sup>75</sup> J. M. Roney,<sup>75</sup> R. J. Sobie,<sup>75</sup> N. Tasneem,<sup>75</sup> T. J. Gershon,<sup>76</sup>  
 P. F. Harrison,<sup>76</sup> T. E. Latham,<sup>76</sup> E. M. T. Puccio,<sup>76</sup> H. R. Band,<sup>77</sup> S. Dasu,<sup>77</sup> Y. Pan,<sup>77</sup> R. Prepost,<sup>77</sup> and S. L. Wu<sup>77</sup>

(*BABAR* Collaboration)

<sup>1</sup>*Laboratoire d'Annecy-le-Vieux de Physique des Particules (LAPP), Université de Savoie,  
 CNRS/IN2P3, F-74941 Annecy-Le-Vieux, France*

<sup>2</sup>*Universitat de Barcelona, Facultat de Fisica, Departament ECM, E-08028 Barcelona, Spain  
<sup>3a</sup>INFN Sezione di Bari, I-70126 Bari, Italy*

<sup>3b</sup>*Dipartimento di Fisica, Università di Bari, I-70126 Bari, Italy*

<sup>4</sup>*University of Bergen, Institute of Physics, N-5007 Bergen, Norway*

<sup>5</sup>*Lawrence Berkeley National Laboratory and University of California, Berkeley, California 94720, USA*

<sup>6</sup>*Ruhr Universität Bochum, Institut für Experimentalphysik 1, D-44780 Bochum, Germany*

<sup>7</sup>*University of British Columbia, Vancouver, British Columbia, Canada V6T 1Z1*

<sup>8</sup>*Brunel University, Uxbridge, Middlesex UB8 3PH, United Kingdom*

<sup>9</sup>*Budker Institute of Nuclear Physics, Novosibirsk 630090, Russia*

<sup>10</sup>*University of California at Irvine, Irvine, California 92697, USA*

<sup>11</sup>*University of California at Riverside, Riverside, California 92521, USA*

<sup>12</sup>*University of California at Santa Barbara, Santa Barbara, California 93106, USA*

<sup>13</sup>*University of California at Santa Cruz, Institute for Particle Physics, Santa Cruz, California 95064, USA*

<sup>14</sup>*California Institute of Technology, Pasadena, California 91125, USA*

<sup>15</sup>*University of Cincinnati, Cincinnati, Ohio 45221, USA*

<sup>16</sup>*University of Colorado, Boulder, Colorado 80309, USA*

<sup>17</sup>*Colorado State University, Fort Collins, Colorado 80523, USA*

<sup>18</sup>*Technische Universität Dortmund, Fakultät Physik, D-44221 Dortmund, Germany*

<sup>19</sup>*Technische Universität Dresden, Institut für Kern- und Teilchenphysik, D-01062 Dresden, Germany*

<sup>20</sup>*Laboratoire Leprince-Ringuet, Ecole Polytechnique, CNRS/IN2P3, F-91128 Palaiseau, France*

<sup>21</sup>*University of Edinburgh, Edinburgh EH9 3JZ, United Kingdom*

<sup>22a</sup>*INFN Sezione di Ferrara, I-44100 Ferrara, Italy*

<sup>22b</sup>*Dipartimento di Fisica, Università di Ferrara, I-44100 Ferrara, Italy*

<sup>23</sup>*INFN Laboratori Nazionali di Frascati, I-00044 Frascati, Italy*

<sup>24a</sup>*INFN Sezione di Genova, I-16146 Genova, Italy*

<sup>24b</sup>*Dipartimento di Fisica, Università di Genova, I-16146 Genova, Italy*

<sup>25</sup>*Indian Institute of Technology Guwahati, Guwahati, Assam, 781 039, India*

<sup>26</sup>*Harvard University, Cambridge, Massachusetts 02138, USA*

<sup>27</sup>*Harvey Mudd College, Claremont, California 91711*

<sup>28</sup>*Universität Heidelberg, Physikalisches Institut, Philosophenweg 12, D-69120 Heidelberg, Germany*

<sup>29</sup>*Humboldt-Universität zu Berlin, Institut für Physik, Newtonstr. 15, D-12489 Berlin, Germany*

<sup>30</sup>*Imperial College London, London, SW7 2AZ, United Kingdom*

<sup>31</sup>*University of Iowa, Iowa City, Iowa 52242, USA*

<sup>32</sup>*Iowa State University, Ames, Iowa 50011-3160, USA*

<sup>33</sup>*Johns Hopkins University, Baltimore, Maryland 21218, USA*

<sup>34</sup>*Laboratoire de l'Accélérateur Linéaire, IN2P3/CNRS et Université Paris-Sud 11, Centre Scientifique d'Orsay,  
 B. P. 34, F-91898 Orsay Cedex, France*

<sup>35</sup>*Lawrence Livermore National Laboratory, Livermore, California 94550, USA*

<sup>36</sup>*University of Liverpool, Liverpool L69 7ZE, United Kingdom*

<sup>37</sup>*Queen Mary, University of London, London, E1 4NS, United Kingdom*

<sup>38</sup>*University of London, Royal Holloway and Bedford New College, Egham, Surrey TW20 0EX, United Kingdom*

<sup>39</sup>*University of Louisville, Louisville, Kentucky 40292, USA*

<sup>40</sup>*Johannes Gutenberg-Universität Mainz, Institut für Kernphysik, D-55099 Mainz, Germany*

<sup>41</sup>*University of Manchester, Manchester M13 9PL, United Kingdom*

<sup>42</sup>*University of Maryland, College Park, Maryland 20742, USA*

<sup>43</sup>*University of Massachusetts, Amherst, Massachusetts 01003, USA*

<sup>44</sup>*Massachusetts Institute of Technology, Laboratory for Nuclear Science, Cambridge, Massachusetts 02139, USA*

<sup>45</sup>*McGill University, Montréal, Québec, Canada H3A 2T8*

<sup>46a</sup>*INFN Sezione di Milano, I-20133 Milano, Italy*

<sup>46b</sup>*Dipartimento di Fisica, Università di Milano, I-20133 Milano, Italy*

<sup>47</sup>*University of Mississippi, University, Mississippi 38677, USA*

<sup>48</sup>*Université de Montréal, Physique des Particules, Montréal, Québec, Canada H3C 3J7*

- <sup>49a</sup>INFN Sezione di Napoli, I-80126 Napoli, Italy  
<sup>49b</sup>Dipartimento di Scienze Fisiche, Università di Napoli Federico II, I-80126 Napoli, Italy  
<sup>50</sup>NIKHEF, National Institute for Nuclear Physics and High Energy Physics, NL-1009 DB Amsterdam, The Netherlands  
<sup>51</sup>University of Notre Dame, Notre Dame, Indiana 46556, USA  
<sup>52</sup>Ohio State University, Columbus, Ohio 43210, USA  
<sup>53</sup>University of Oregon, Eugene, Oregon 97403, USA  
<sup>54a</sup>INFN Sezione di Padova, I-35131 Padova, Italy  
<sup>54b</sup>Dipartimento di Fisica, Università di Padova, I-35131 Padova, Italy  
<sup>55</sup>Laboratoire de Physique Nucléaire et de Hautes Energies, IN2P3/CNRS, Université Pierre et Marie Curie-Paris6, Université Denis Diderot-Paris7, F-75252 Paris, France  
<sup>56a</sup>INFN Sezione di Perugia, I-06100 Perugia, Italy  
<sup>56b</sup>Dipartimento di Fisica, Università di Perugia, I-06100 Perugia, Italy  
<sup>57a</sup>INFN Sezione di Pisa, I-56127 Pisa, Italy  
<sup>57b</sup>Dipartimento di Fisica, Università di Pisa, I-56127 Pisa, Italy  
<sup>57c</sup>Scuola Normale Superiore di Pisa, I-56127 Pisa, Italy  
<sup>58</sup>Princeton University, Princeton, New Jersey 08544, USA  
<sup>59a</sup>INFN Sezione di Roma, I-00185 Roma, Italy  
<sup>59b</sup>Dipartimento di Fisica, Università di Roma La Sapienza, I-00185 Roma, Italy  
<sup>60</sup>Universität Rostock, D-18051 Rostock, Germany  
<sup>61</sup>Rutherford Appleton Laboratory, Chilton, Didcot, Oxon, OX11 0QX, United Kingdom  
<sup>62</sup>CEA, Ifu, SPP, Centre de Saclay, F-91191 Gif-sur-Yvette, France  
<sup>63</sup>SLAC National Accelerator Laboratory, Stanford, California 94309 USA  
<sup>64</sup>University of South Carolina, Columbia, South Carolina 29208, USA  
<sup>65</sup>Southern Methodist University, Dallas, Texas 75275, USA  
<sup>66</sup>Stanford University, Stanford, California 94305-4060, USA  
<sup>67</sup>State University of New York, Albany, New York 12222, USA  
<sup>68</sup>Tel Aviv University, School of Physics and Astronomy, Tel Aviv, 69978, Israel  
<sup>69</sup>University of Tennessee, Knoxville, Tennessee 37996, USA  
<sup>70</sup>University of Texas at Austin, Austin, Texas 78712, USA  
<sup>71</sup>University of Texas at Dallas, Richardson, Texas 75083, USA  
<sup>72a</sup>INFN Sezione di Torino, I-10125 Torino, Italy  
<sup>72b</sup>Dipartimento di Fisica Sperimentale, Università di Torino, I-10125 Torino, Italy  
<sup>73a</sup>INFN Sezione di Trieste, I-34127 Trieste, Italy  
<sup>73b</sup>Dipartimento di Fisica, Università di Trieste, I-34127 Trieste, Italy  
<sup>74</sup>IFIC, Universitat de Valencia-CSIC, E-46071 Valencia, Spain  
<sup>75</sup>University of Victoria, Victoria, British Columbia, Canada V8W 3P6  
<sup>76</sup>Department of Physics, University of Warwick, Coventry CV4 7AL, United Kingdom  
<sup>77</sup>University of Wisconsin, Madison, Wisconsin 53706, USA

(Received 14 May 2012; published 28 August 2012)

A precise measurement of the cross section of the process  $e^+e^- \rightarrow \pi^+\pi^-(\gamma)$  from threshold to an energy of 3 GeV is obtained with the initial-state radiation (ISR) method using 232 fb<sup>-1</sup> of data collected with the *BABAR* detector at  $e^+e^-$  center-of-mass energies near 10.6 GeV. The ISR luminosity is determined from a study of the leptonic process  $e^+e^- \rightarrow \mu^+\mu^-(\gamma)\gamma_{\text{ISR}}$ , which is found to agree with the next-to-leading-order QED prediction to within 1.1%. The cross section for the process  $e^+e^- \rightarrow \pi^+\pi^-(\gamma)$  is obtained with a systematic uncertainty of 0.5% in the dominant  $\rho$  resonance region. The leading-order hadronic contribution to the muon magnetic anomaly calculated using the measured  $\pi\pi$  cross section from threshold to 1.8 GeV is  $(514.1 \pm 2.2(\text{stat}) \pm 3.1(\text{syst})) \times 10^{-10}$ .

DOI: 10.1103/PhysRevD.86.032013

PACS numbers: 13.40.Em, 13.60.Hb, 13.66.Bc, 13.66.Jn

<sup>\*</sup>Deceased.<sup>†</sup>Now at the University of Tabuk, Tabuk 71491, Saudi Arabia.<sup>‡</sup>Also with Università di Perugia, Dipartimento di Fisica, Perugia, Italy.<sup>§</sup>Now at Institute of High Energy Physics, Beijing, China.<sup>||</sup>Now at the University of Huddersfield, Huddersfield HD1 3DH, UK.<sup>¶</sup>Now at University of South Alabama, Mobile, AL 36688, USA.<sup>\*\*</sup>Also with Università di Sassari, Sassari, Italy.

## I. INTRODUCTION

### A. The physics context

The theoretical precision of observables like the running of the quantum electrodynamic (QED) fine structure constant  $\alpha(s)$  or the anomalous magnetic moment of the muon is limited by second-order loop effects from hadronic vacuum polarization (VP). Theoretical calculations

are related to hadronic production rates in  $e^+e^-$  annihilation via dispersion relations. As perturbative quantum chromodynamic theory fails in the energy regions where resonances occur, measurements of the  $e^+e^- \rightarrow$  hadrons cross section are necessary to evaluate the dispersion integrals. Of particular interest is the contribution  $a_\mu^{\text{had}}$  to the muon magnetic moment anomaly  $a_\mu$ , which requires data in a region dominated by the process  $e^+e^- \rightarrow \pi^+\pi^-(\gamma)$ . The accuracy of the theoretical prediction for  $a_\mu$  is linked to the advances in  $e^+e^-$  measurements. A discrepancy of roughly 3 standard deviations ( $\sigma$ ) including systematic uncertainties between the measured [1] and predicted [2–4] values of  $a_\mu$  persisted for years before the results of this analysis became available [5], possibly hinting at new physics. An independent approach using  $\tau$  decay data leads to a smaller difference of  $1.8\sigma$  [6] in the same direction, with enlarged systematic uncertainties due to isospin-breaking corrections.

The kernel in the integrals involved in vacuum polarization calculations strongly emphasizes the low-energy part of the spectrum. About 73% of the lowest-order hadronic contribution is provided by the  $\pi^+\pi^-(\gamma)$  final state, and about 60% of its total uncertainty stems from that mode [7]. To improve on present calculations, the precision on the VP dispersion integrals is required to be better than 1%. More precise experimental data in the  $\pi^+\pi^-(\gamma)$  channel are needed, such that systematic uncertainties on the cross sections that are correlated over the relevant mass range are kept well below the percent level.

In this paper an analysis of the process  $e^+e^- \rightarrow \pi^+\pi^-(\gamma)\gamma$  based on data collected with the *BABAR* experiment is presented. In addition, as a cross-check of the analysis, we measure the  $e^+e^- \rightarrow \mu^+\mu^-(\gamma)\gamma$  cross section on the same data and compare it to the QED prediction. The reported results and their application to the  $\pi\pi$  contribution to the muon magnetic anomaly have been already published in shorter form [5].

## B. The ISR approach

The initial-state radiation (ISR) method has been proposed [8–11] as a novel way to study  $e^+e^-$  annihilation processes instead of the standard point-by-point energy-scan measurements. The main advantage of the ISR approach is that the final-state mass spectrum is obtained in a single configuration of the  $e^+e^-$  storage rings and of the detection apparatus, thus providing a cross section measurement over a wide mass range starting at threshold. Consequently, a better control of the systematic errors can be achieved compared to the energy-scan method, which necessitates different experiments and colliders to cover the same range. The disadvantage is the reduction of the measured cross section, which is suppressed by one order of  $\alpha$ . This is offset by the availability of high-luminosity  $e^+e^-$  storage rings, primarily designed as *B* and *K* factories in order to study *CP* violation.

In the ISR method, the cross section for  $e^+e^- \rightarrow X$  at the reduced energy  $\sqrt{s'} = m_X$ , where  $X$  can be any final state, is deduced from a measurement of the radiative process  $e^+e^- \rightarrow X\gamma$ , where the photon is emitted by the initial  $e^+$  or  $e^-$  particle. The reduced energy is related to the energy  $E_\gamma^*$  of the ISR photon in the  $e^+e^-$  center-of-mass (c.m.) frame by  $s' = s(1 - 2E_\gamma^*/\sqrt{s})$ , where  $s$  is the square of the  $e^+e^-$  c.m. energy. In this analysis,  $s \sim (10.58 \text{ GeV})^2$  and  $\sqrt{s'}$  ranges from the two-pion production threshold to 3 GeV. Two-body ISR processes  $e^+e^- \rightarrow X\gamma$  with  $X = \pi^+\pi^-(\gamma)$  and  $X = \mu^+\mu^-(\gamma)$  are measured, where the ISR photon is detected at large angle to the beams, and the charged particle pair can be accompanied by a final-state radiation (FSR) photon.

Figure 1 shows the Feynman diagrams relevant to this study. The lowest-order (LO) radiated photon can be either from ISR or FSR. In the muon channel, ISR is dominant in the measurement range, but the LO FSR contribution needs to be subtracted using QED. In the pion channel, the LO FSR calculation is model-dependent, but the contribution is strongly suppressed due to the large  $s$  value. In both channels, interference between ISR and FSR amplitudes vanishes for a charge-symmetric detector.

In order to control the overall efficiency to high precision, it is necessary to consider higher-order radiation. The next-to-leading-order (NLO) correction in  $\alpha$  amounts to about 4% [12] with the selection used for this analysis, while the next-to-next-to-leading-order (NNLO) correction is expected to be at least 1 order of magnitude smaller than NLO. Most of the higher-order contributions come from ISR and hence are independent of the final state. As the cross section is measured through the  $\pi\pi/\mu\mu$  ratio, as explained below, most higher-order radiation effects cancel and NLO is sufficient to reach precisions of  $10^{-3}$ . As a result, the selection keeps  $\pi\pi\gamma\gamma$  ( $\mu\mu\gamma\gamma$ ) as well as  $\pi\pi\gamma$  ( $\mu\mu\gamma$ ) final states, where the additional photon can be either ISR or FSR.

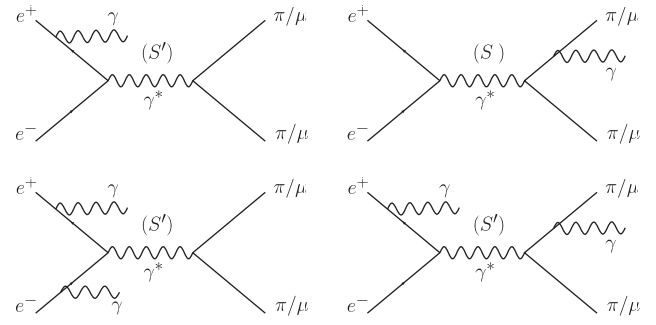


FIG. 1. The generic Feynman diagrams for the processes relevant to this study with one or two real photons: lowest-order (LO) ISR (top left), LO FSR (top right), next-to-leading order (NLO) ISR with additional ISR (bottom left), NLO with additional FSR (bottom right).

### C. Cross section measurement through the $\pi\pi/\mu\mu$ ratio

The cross section for the process  $e^+ e^- \rightarrow X$  is related to the  $\sqrt{s'}$  spectrum of  $e^+ e^- \rightarrow X\gamma_{\text{ISR}}$  events through

$$\frac{dN_{X\gamma_{\text{ISR}}}}{d\sqrt{s'}} = \frac{dL_{\text{ISR}}^{\text{eff}}}{d\sqrt{s'}} \varepsilon_{X\gamma}(\sqrt{s'}) \sigma_X^0(\sqrt{s'}), \quad (1)$$

where  $dL_{\text{ISR}}^{\text{eff}}/d\sqrt{s'}$  is the effective ISR luminosity,  $\varepsilon_{X\gamma}$  is the full acceptance for the event sample, and  $\sigma_X^0$  is the “bare” cross section for the process  $e^+ e^- \rightarrow X$  (including additional FSR photons), in which the leptonic and hadronic vacuum polarization effects are removed.

Equation (1) applies equally to  $X = \pi\pi(\gamma)$  and  $X = \mu\mu(\gamma)$  final states, so that the ratio of cross sections is directly related to the ratio of the pion to muon spectra as a function of  $\sqrt{s'}$ . Specifically, the ratio  $R_{\text{exp}}(\sqrt{s'})$  of the produced  $\pi\pi(\gamma)\gamma_{\text{ISR}}$  and  $\mu\mu(\gamma)\gamma_{\text{ISR}}$  spectra, obtained from the measured spectra corrected for full acceptance, can be expressed as

$$R_{\text{exp}}(\sqrt{s'}) = \frac{\frac{dN_{\pi\pi(\gamma)\gamma_{\text{ISR}}}^{\text{prod}}}{d\sqrt{s'}}}{\frac{dN_{\mu\mu(\gamma)\gamma_{\text{ISR}}}^{\text{prod}}}{d\sqrt{s'}}} \quad (2)$$

$$= \frac{\sigma_{\pi\pi(\gamma)}^0(\sqrt{s'})}{(1 + \delta_{\text{FSR}}^{\mu\mu})\sigma_{\mu\mu(\gamma)}^0(\sqrt{s'})} \quad (3)$$

$$= \frac{R^0(\sqrt{s'})}{(1 + \delta_{\text{FSR}}^{\mu\mu})(1 + \delta_{\text{add.FSR}}^{\mu\mu})}. \quad (4)$$

The “bare” ratio  $R^0$  (no vacuum polarization, but additional FSR included), which enters the VP dispersion integrals, is given by

$$R^0(\sqrt{s'}) = \frac{\sigma_{\pi\pi(\gamma)}^0(\sqrt{s'})}{\sigma_{\text{pt}}(\sqrt{s'})}, \quad (5)$$

where  $\sigma_{\text{pt}} = 4\pi\alpha^2/3s'$  is the cross section for pointlike charged fermions. The factor  $(1 + \delta_{\text{FSR}}^{\mu\mu})$  corrects for the lowest-order FSR contribution, including possibly additional soft photons, to the  $e^+ e^- \rightarrow \mu^+ \mu^- \gamma$  final state, as is explicitly given in Eq. (18). No such factor is included for pions because of the negligible LO FSR contribution (see Sec. IX H 1). The factor  $(1 + \delta_{\text{add.FSR}}^{\mu\mu})$  corrects for additional FSR in the  $e^+ e^- \rightarrow \mu^+ \mu^-$  process at  $\sqrt{s'}$ , as is explicitly given in Eq. (19).

In this analysis, we use a procedure strictly equivalent to taking the ratio  $R_{\text{exp}}(\sqrt{s'})$ , namely, we measure the  $\sigma_{\pi\pi(\gamma)}^0(\sqrt{s'})$  cross section using Eq. (1) in which the effective ISR luminosity is obtained from the mass spectrum of produced  $\mu\mu(\gamma)\gamma_{\text{ISR}}$  events divided by the  $\sigma_{\mu\mu(\gamma)}^0(\sqrt{s'})$  cross section computed with QED. The ISR luminosity measurement is described in detail in Sec. VIII F.

This way of proceeding considerably reduces the uncertainties related to the effective ISR luminosity function when determined through

$$\frac{dL_{\text{ISR}}^{\text{eff}}}{d\sqrt{s'}} = L_{ee} \frac{dW}{d\sqrt{s'}} \left( \frac{\alpha(s')}{\alpha(0)} \right)^2 \frac{\varepsilon_{\gamma_{\text{ISR}}}(\sqrt{s'})}{\varepsilon_{\gamma_{\text{ISR}}}^{\text{MC}}(\sqrt{s'})}. \quad (6)$$

Equation (6) relies on the  $e^+ e^-$  luminosity measurement ( $L_{ee}$ ) and on the theoretical radiator function  $dW/d\sqrt{s'}$ . The latter describes the probability to radiate an ISR photon (with possibly additional ISR photons) so that the produced final state (excluding ISR photons) has a mass  $\sqrt{s'}$ . It depends on  $\sqrt{s}$ , on  $\sqrt{s'}$ , and on the angular range ( $\theta_{\min}^*, \theta_{\max}^*$ ) of the ISR photon in the  $e^+ e^-$  c.m. system. For convenience, two factors that are common to the muon and pion channels are included in the effective luminosity definition of Eq. (6): (i) the ratio of  $\varepsilon_{\gamma_{\text{ISR}}}$ , the efficiency to detect the main ISR photon, to the same quantity  $\varepsilon_{\gamma_{\text{ISR}}}^{\text{MC}}$  in simulation, and (ii) the vacuum polarization correction  $(\alpha(s')/\alpha(0))^2$ . The latter factor is implicitly included in the effective luminosity deduced from  $\mu\mu(\gamma)\gamma_{\text{ISR}}$  data using Eq. (1), while the former, which cancels out in the  $\pi\pi$  to  $\mu\mu$  ratio, is ignored in Eq. (1). As an important cross-check of the analysis, hereafter called the QED test, we use Eq. (6), together with Eq. (1), to measure the muon cross section and compare it to the QED prediction.

Many advantages follow from taking the  $R_{\text{exp}}(\sqrt{s'})$  ratio:

- (i) the result is independent of the *BABAR* luminosity  $L_{ee}$  measurement;
- (ii) the determination of the ISR luminosity comes from the muon data, independently of the number of additional ISR photons, and thus does not depend on a theoretical calculation;
- (iii) the ISR photon efficiency cancels out;
- (iv) the vacuum polarization also cancels out.

Furthermore the Monte Carlo generator and the detector simulation are only used to compute the acceptance of the studied  $X\gamma_{\text{ISR}}$  processes, with  $X = \pi\pi(\gamma), \mu\mu(\gamma)$ . The overall systematic uncertainty on the  $\pi\pi$  cross section is reduced, because some individual uncertainties cancel between pions and muons.

## II. ANALYSIS OUTLINE

### A. The *BABAR* detector and data samples

The analysis is based on  $232 \text{ fb}^{-1}$  of data collected with the *BABAR* detector at the SLAC PEP-II asymmetric-energy  $e^+ e^-$  storage rings operated at the  $\Upsilon(4S)$  resonance. The *BABAR* detector is described in detail elsewhere [13]. Charged-particle tracks are measured with a five-layer double-sided silicon vertex tracker (SVT) together with a 40-layer drift chamber (DCH) inside a 1.5 T superconducting solenoid magnet. Photons are assumed to originate from the primary vertex defined by

the charged tracks of the event and their energy is measured in a CsI(Tl) electromagnetic calorimeter (EMC). Charged-particle identification (PID) uses the ionization losses  $dE/dx$  in the SVT and DCH, the Cherenkov radiation detected in a ring-imaging device (DIRC), the shower energy deposit in the EMC ( $E_{\text{cal}}$ ) and the shower shape in the instrumented flux return (IFR) of the magnet. The IFR system is constructed from modules of resistive plate chambers interspersed with iron slabs, arranged in a configuration with a barrel and two endcaps.

## B. Monte Carlo generators and simulation

Signal and background ISR processes  $e^+e^- \rightarrow X\gamma$  are simulated with a Monte Carlo (MC) event generator called AfkQed, which is based on the formalism of Ref. [14]. The main ISR (or main FSR in the case of  $\mu\mu\gamma$ ) photon is generated within the angular range [ $\theta_{\min}^* = 20^\circ$ ,  $\theta_{\max}^* = 160^\circ$ ] in the c.m. system, bracketing the photon detection range with a margin to account for finite resolution. Additional ISR photons are generated with the structure function method [15], and additional FSR photons with PHOTOS [16]. Additional ISR photons are emitted along the  $e^+$  or  $e^-$  beam particle direction. A minimum mass  $m_{X\gamma_{\text{ISR}}} > 8 \text{ GeV}/c^2$  is imposed at generation, which places an upper bound on the additional ISR photon energy. Samples corresponding to 5 to 10 times the number of data events are generated for the signal channels. The more accurate Phokhara generator [17] is used at the 4-vector level to study some effects (defined in Sec. IX D) related to additional ISR photons. Background processes  $e^+e^- \rightarrow q\bar{q}$  ( $q = u, d, s, c$ ) are generated with JETSET [18], and  $e^+e^- \rightarrow \tau^+\tau^-$  with KORALB [19]. The response of the *BABAR* detector is simulated with GEANT4 [20].

## C. Analysis method

The  $\pi\pi(\gamma)\gamma_{\text{ISR}}$  and  $\mu\mu(\gamma)\gamma_{\text{ISR}}$  processes are measured independently with full internal checks and the ratio  $R_{\text{exp}}(\sqrt{s'})$ , which yields the measured  $\sigma_{\pi\pi(\gamma)}^0(\sqrt{s'})$  cross section, is only examined after these checks are successfully passed. One of the most demanding tests is the absolute comparison of the  $\mu\mu(\gamma)\gamma_{\text{ISR}}$  cross section, which uses the *BABAR*  $L_{ee}$  luminosity, with the NLO QED prediction (QED test).

After preliminary results were presented from the blind analysis [21], a few aspects of the analysis were revisited to refine some effects that had been initially overlooked, mostly affecting the correlated loss of muon identification for both tracks. While the final measurement is not a strictly blind analysis, all studies are again made independently for muons and pions and combined at the very end.

The selected events correspond to a final state with two tracks and the ISR candidate, all within the detector acceptance, as described in Sec. III. Kinematic fits provide discrimination of the channels under study from other

processes. However the separation between the different two-prong final states (including  $K^+K^-(\gamma)\gamma_{\text{ISR}}$ ) relies exclusively on the identification of the charged particles. Thus particle identification plays a major role in the analysis. This is the subject of Sec. IV D. Background reduction and control of the remaining background contributions are another challenge of the analysis, in particular, in the pion channel away from the  $\rho$  resonance. This is discussed in Sec. VI.

The determination of the  $\sqrt{s'}$  spectrum is described in Sec. VII. The relevant final-state mass is  $m_{\pi\pi}$  ( $m_{\mu\mu}$ ) when there is additional ISR or no additional radiation, or  $m_{\pi\pi\gamma}$  ( $m_{\mu\mu\gamma}$ ) in the case of additional FSR. The  $\sqrt{s'}$  spectrum is obtained from the observed  $m_{\pi\pi}$  ( $m_{\mu\mu}$ ) distributions through unfolding (Sec. VII A).

Although selection of the final state of two-body ISR processes is rather simple, the main difficulty of the analysis resides in the full control of all involved efficiencies. Relying on the simulation alone cannot provide the required precision. The simulation is used in a first step in order to incorporate in a consistent way all effects entering the final event acceptance. Corrections for data-to-MC differences are obtained for each efficiency using dedicated studies performed on the data and simulation samples. The main contributions for these corrections originate from trigger, tracking, particle identification, and the  $\chi^2$  selection of the kinematic fits, so that the corrected efficiency is

$$\varepsilon = \varepsilon_{\text{MC}} \left( \frac{\varepsilon_{\text{trig}}^{\text{data}}}{\varepsilon_{\text{trig}}^{\text{MC}}} \right) \left( \frac{\varepsilon_{\text{track}}^{\text{data}}}{\varepsilon_{\text{track}}^{\text{MC}}} \right) \left( \frac{\varepsilon_{\text{PID}}^{\text{data}}}{\varepsilon_{\text{PID}}^{\text{MC}}} \right) \left( \frac{\varepsilon_{\chi^2}^{\text{data}}}{\varepsilon_{\chi^2}^{\text{MC}}} \right). \quad (7)$$

The corrections  $C_i = (\frac{\varepsilon_i^{\text{data}}}{\varepsilon_i^{\text{MC}}})$  are reviewed in turn in the following sections (Sec. IV and V). They are applied as mass-dependent corrections to the MC efficiency. They amount to at most a few percent and are known to a few permil level or better. Efficiency measurements are designed to avoid correlations between the  $C_i$ . Further data-to-MC corrections deal with second-order effects related to the description of additional ISR in the generator, which was found inadequate at the level of precision required for this analysis. As outlined in Sec. I B the chosen approach guarantees that radiative corrections are at a very small level. Residual effects are studied in Sec. IX D.

## III. EVENT SELECTION

### A. Topological selection

Two-body ISR events are selected by requiring a photon candidate with  $E_\gamma^* > 3 \text{ GeV}$  and laboratory polar angle in the range  $0.35\text{--}2.4 \text{ rad}$ , and exactly two tracks of opposite charge, each with momentum  $p > 1 \text{ GeV}c^{-1}$  and within the

---

<sup>1</sup>Unless otherwise stated, starred quantities are measured in the  $e^+e^-$  c.m. and unstarred quantities in the laboratory.

angular range 0.40–2.45 rad. A photon candidate is defined as a cluster in the EMC, with energy larger than 0.02 GeV, not associated to a charged track. If several photons are detected, the main ISR photon is assumed to be that with the highest  $E_\gamma^*$ ; this results in an incorrectly assigned ISR photon in less than  $\sim 10^{-4}$  of the events, mostly due to the ISR photon loss in inactive areas of the EMC. The track momentum requirement is dictated by the falloff of the muon-identification efficiency at low momenta. The tracks are required to have at least 15 hits in the DCH, and originate within 5 mm of the collision axis (distance of closest approach  $d_{\text{oca}}_{xy} < 5 \text{ mm}$ ) and within 6 cm from the beam spot along the beam direction ( $|\Delta_z| < 6 \text{ cm}$ ). They are required to extrapolate to the DIRC active area, whose length further restricts the minimum track polar angle to  $\sim 0.45$  rad. Tracks are also required to extrapolate to the IFR active areas that exclude low-efficiency regions. An additional veto based on a combination of  $E_{\text{cal}}$  and  $dE/dx$ ,  $((E_{\text{cal}}/p - 1)/0.15)^2 + ((dE/dx_{\text{DCH}} - 690)/150)^2 < 1$ , reduces electron contamination. Events can be accompanied by any number of “bad” tracks, not satisfying the above criteria, and any number of additional photons. To ensure a rough momentum balance at the preselection level (hereafter called “preselection cut”), the ISR photon is required to lie within 0.3 rad of the missing momentum of the tracks (or of tracks plus other photons).

## B. Kinematic fit description and $\chi^2$ selection

For both the  $\mu\mu\gamma$  and  $\pi\pi\gamma$  processes, the event definition is enlarged to include the radiation of one photon in addition to the already-required ISR photon. Two types of fits are considered, according to the following situations:

- The additional photon is detected in the EMC, in which case its energy and angles can be readily used in the fit: we call this a 3-constraint (3C) FSR fit, although the extra photon can be either from FSR or from ISR at large angle to the beams. The threshold for the additional photon is kept low (20 MeV). This can introduce some background, but with little effect as the fit in that case would not be different in practice from a standard fit to the  $\mu\mu(\gamma)\gamma_{\text{ISR}}$  ( $\pi\pi(\gamma)\gamma_{\text{ISR}}$ ) hypothesis.
- The additional photon is assumed to be from ISR at a small angle to the beams. Since further information<sup>2</sup> is not available, it is presumed that the extra photon is perfectly aligned with either the  $e^+$  or the  $e^-$  beam. The corresponding so-called 2C ISR fit ignores additional photons measured in the EMC and determines the energy of the fitted collinear ISR photon.

<sup>2</sup>This is not strictly true as the missing photon could be completely reconstructed if the ISR photon energy were used in the kinematic fit. However tests have shown that the relative quality of this new information does not permit a significant improvement for the fitted direction of the additional ISR photon over the collinear assumption.

In both cases the constrained fit procedure uses the ISR photon direction and the measured momenta and angles of the two tracks with their covariance matrix in order to solve the four energy-momentum conservation equations. The measured energy of the primary ISR photon is not used in either fit, as it adds little information for the relatively low masses involved.

Each event is characterized by two  $\chi^2$  values,  $\chi^2_{\text{FSR}}$  and  $\chi^2_{\text{ISR}}$  from the FSR and ISR fits, respectively, which are examined on a two-dimensional (2D) plot. In practice the quantities  $\ln(\chi^2 + 1)$  are used so that the long tails can be properly visualized (Figs. 2 and 3). Events without any extra measured photons have only the  $\chi^2_{\text{ISR}}$  value and they are plotted separately on a line above the  $\chi^2_{\text{FSR}}$  overflow. In case several extra photons are detected, FSR fits are

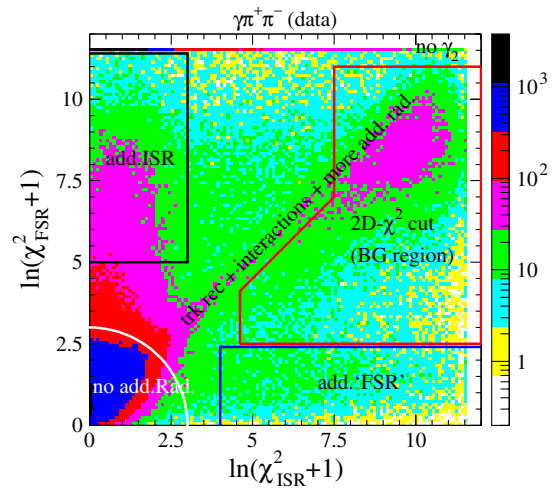


FIG. 2 (color online). The 2D- $\chi^2$  distribution for  $\pi\pi(\gamma)\gamma_{\text{ISR}}$  (data) for  $0.5 < m_{\pi\pi} < 1.0 \text{ GeV}/c^2$ , where different interesting regions are defined.

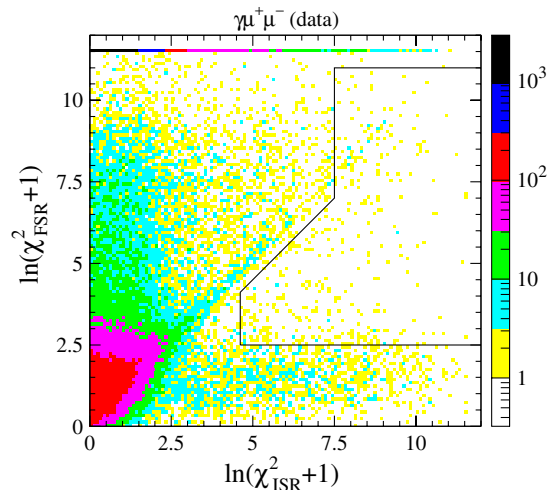


FIG. 3 (color online). The 2D- $\chi^2$  distribution for  $\mu\mu(\gamma)\gamma_{\text{ISR}}$  (data) for  $0.5 < m_{\mu\mu} < 1.0 \text{ GeV}/c^2$ , where the signal and background regions are indicated.

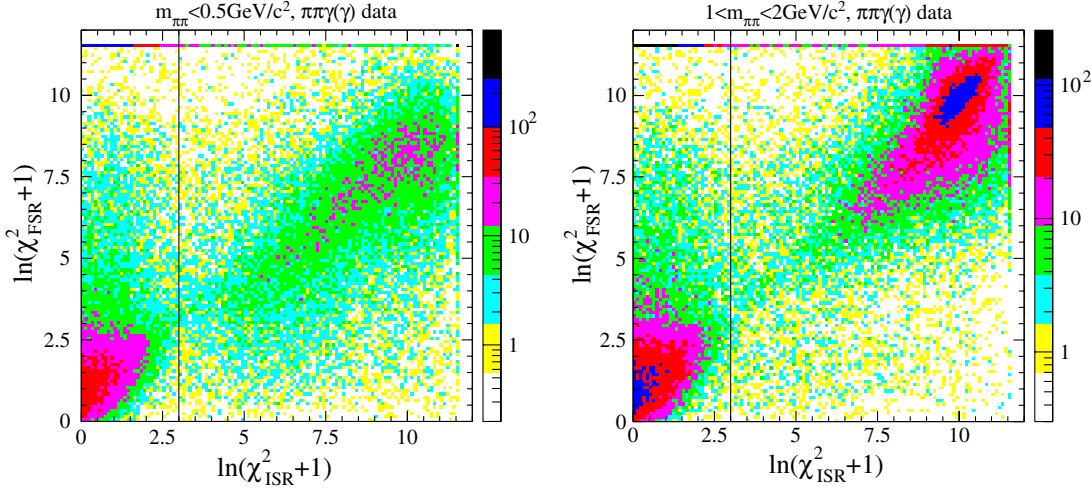


FIG. 4 (color online). The 2D- $\chi^2$  distributions in  $\pi\pi(\gamma)\gamma_{\text{ISR}}$  data: (left) below the central  $\rho$  region ( $m_{\pi\pi} < 0.5 \text{ GeV}/c^2$ ); (right) above the central  $\rho$  region ( $1. < m_{\pi\pi} < 2. \text{ GeV}/c^2$ ). The line indicates the boundary for the tight  $\chi^2$  selection.

performed using each photon in turn and the fit with the smallest  $\chi^2_{\text{FSR}}$  is retained. The muon (pion) mass is assumed for the two charged particles, according to the selected channel, and in the following studies and final distributions, the  $\mu\mu$  ( $\pi\pi$ ) mass is obtained using the fitted parameters of the two charged particles from the ISR fit if  $\chi^2_{\text{ISR}} < \chi^2_{\text{FSR}}$  and from the FSR fit in the reverse case.

It is easy to visualize the different interesting regions in the 2D- $\chi^2$  plane, as illustrated in Fig. 2 for  $\pi\pi(\gamma)\gamma_{\text{ISR}}$  data. Most of the events peak at small values of both  $\chi^2$ , but the tails along the axes clearly indicate events with additional radiation: small-angle ISR along the  $\chi^2_{\text{FSR}}$  axis (with large ISR energies at large values of  $\chi^2_{\text{FSR}}$ ), or FSR or large-angle ISR along the  $\chi^2_{\text{ISR}}$  axis (with large additional radiation energies at large values of  $\chi^2_{\text{ISR}}$ ). Events along the diagonal do not satisfy either hypothesis and result from resolution effects for the pion tracks (also secondary interactions) or the primary ISR photon, or possibly additional radiation of more than one photon. Multibody background populates the region where both  $\chi^2$  are large and consequently a background region is defined in the 2D- $\chi^2$  plane. This region is optimized as a compromise between efficiency and background contamination in the signal sample, aiming at best control of the corresponding systematic uncertainties.

The  $\chi^2$  criteria used in the pion analysis depend on the  $\pi\pi$  mass region considered. The  $m_{\pi\pi}$  region between 0.5 and 1  $\text{GeV}/c^2$  is dominated by the  $\rho$  resonance. The corresponding large cross section provides a dominant contribution to vacuum-polarization dispersion integrals, so it has to be known with small systematic uncertainties. Also background is expected to be at a small level in this region. These two considerations argue for large efficiencies, in order to keep systematic uncertainties sufficiently low. Therefore a loose  $\chi^2$  criterion is used, where the physical (accepted) region corresponds to the left of the contour outlined in Fig. 2, excluding the BG-labeled

region. The same loose  $\chi^2$  criterion is applied for the  $\mu\mu(\gamma)\gamma_{\text{ISR}}$  analysis (Fig. 3).

The pion form factor decreases rapidly away from the  $\rho$  peak, while the backgrounds vary slowly with the  $\pi\pi$  mass. The multihadronic background in the physical sample becomes excessively large if the  $\chi^2$  criterion as used in the  $\rho$  region is applied, and it is necessary to tighten the selection of  $\pi\pi(\gamma)\gamma_{\text{ISR}}$  events. Figure 4 shows the tight  $\chi^2$  selection boundary  $\ln(\chi^2_{\text{ISR}} + 1) < 3$  chosen to reduce multihadronic background, and the 2D- $\chi^2$  distributions for masses below and above the central  $\rho$  region. The tight  $\chi^2$  criterion retains events with additional ISR since this region in the  $\chi^2$  plane is free of multihadronic background. The reduced efficiency on signal from the tight selection results in a larger relative uncertainty, but this is still acceptable considering the much smaller contribution from the  $\rho$  tails to the dispersion integral.

Efficiencies and systematic uncertainties resulting from the loose and tight  $\chi^2$  selection criteria are discussed in Sec. V B.

#### IV. EFFICIENCY STUDIES (I)

To achieve the required precision for the cross section measurement, efficiencies are validated with data at every step of the event processing, and mass-dependent data/MC corrections are determined. This necessitates specific studies on data control samples whose selection criteria are designed to minimize biases on efficiency measurements. Residual effects are estimated and included in the systematic errors.

##### A. Efficiency-dedicated event selection and kinematic fit

For trigger and tracking efficiency studies, a dedicated selection of  $\mu^+\mu^-\gamma_{\text{ISR}}$  and  $\pi^+\pi^-\gamma_{\text{ISR}}$  events is devised

that only requires one reconstructed track (called “primary”), identified as a muon or pion, and the ISR photon. A 1C kinematic fit is performed and the momentum vector of the second muon (pion) is predicted from 4-momentum conservation. Standard track selection is applied to the primary track and the predicted track is required to be in the acceptance.

### B. Trigger and filtering

A number of trigger conditions are imposed at the hardware (L1) and online software (L3) levels, as well as in a final filtering, before an event is fully reconstructed and stored in the *BABAR* data sample. They are common to all *BABAR* analyses, and hence are not specifically designed to select ISR events. Since individual trigger and filter line responses are stored for every recorded event, efficiencies can be computed by comparing the response of trigger lines, after choosing lines that are as orthogonal and as efficient as possible. Trigger efficiencies are determined on data and simulation samples, after applying identical event selections and measurement methods, and data/MC corrections  $C_{\text{trig}}$  are computed from the comparison of measured efficiencies on background-subtracted data and signal MC. Once the physics origins of inefficiencies are identified, uncertainties are estimated through studies of biases and data-to-MC comparison of distributions of relevant quantities. Efficiencies and data/MC corrections are measured separately for the pion and muon channels.

Trigger efficiencies are determined on samples unbiased with respect to the number of tracks actually reconstructed, to avoid correlations between trigger and tracking efficiency measurements. In practice, one- and two-track samples are sufficient and consequently the trigger control samples are selected through the dedicated 1C kinematic fit described above. Because of the loose requirement with respect to tracking, the data samples contain backgrounds with potentially different trigger efficiencies to that of the signal. These backgrounds are studied with simulation and are then subtracted. To obtain data samples that are as pure as possible, criteria tighter than the standard track selection are applied to the primary track, including tight PID identification. Possible biases resulting from the tighter selection are studied and accounted for in the systematic errors. Background contributions are subtracted from the data spectra using properly-normalized simulated samples, and, if necessary, with data/MC correction of the trigger efficiencies in an iterative procedure.

The data/MC corrections for the L1 trigger are found to be at a few  $\times 10^{-4}$  level for muon and pion events. The L3 level involves a track trigger (at least one track is required) and a calorimetric trigger (demanding at least one high-energy cluster and one low-energy cluster). Both of them are efficient for  $\pi\pi\gamma_{\text{ISR}}$  events. For  $\mu\mu\gamma_{\text{ISR}}$  events, the small efficiency of the calorimetric trigger limits the statistical precision of the track-trigger and overall efficiency

measurements. Furthermore, a correlated change of the two trigger line responses for close-by tracks induces both a nonuniformity in the efficiency and a bias in the efficiency measurement. This originates from the overlap of tracks in the drift chamber and of showers in the EMC, which induces a simultaneous decrease in the track-trigger efficiency and an increase in the calorimetric-trigger efficiency. Overlap is a major source of overall inefficiency and difference between data and simulation, necessitating specific studies. The correction to the MC L3 trigger efficiency is small for pions, about  $2 \times 10^{-3}$  at the  $\rho$  peak, and known to a precision better than  $10^{-3}$ . The data/MC correction  $C_{\text{trig}}$  is larger in the  $\mu\mu(\gamma)\gamma_{\text{ISR}}$  channel, due to the dominant role of the track trigger, about 1% at a  $\mu\mu$  mass of  $0.7 \text{ GeV}/c^2$ , and known to a precision of  $3 \times 10^{-3}$  (Fig. 5 top). Uncertainties, which increase to  $5 \times 10^{-3}$  at the maximum overlap ( $m_{\mu\mu} \sim 0.4 \text{ GeV}/c^2$ ), are mostly statistical in nature.

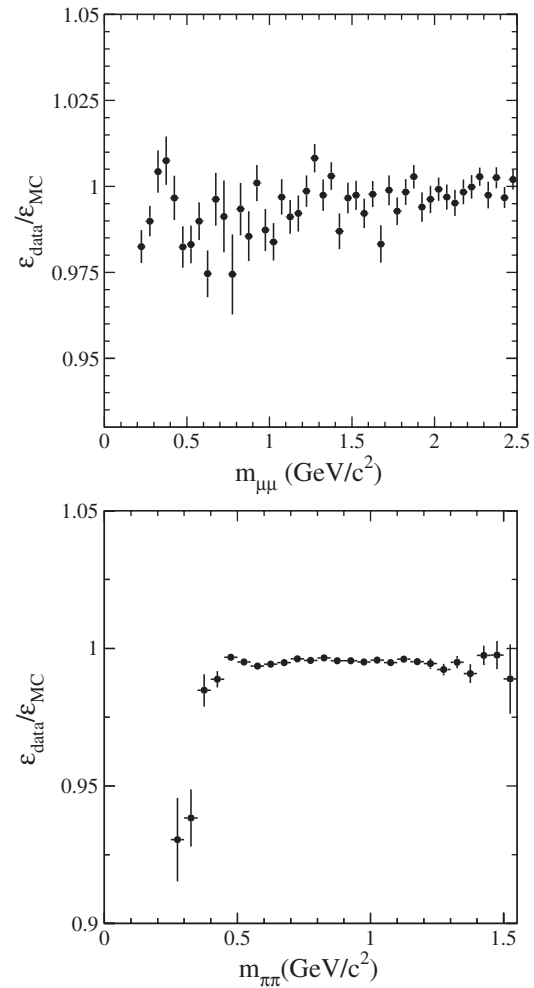


FIG. 5. The data/MC event trigger and filter correction  $C_{\text{trig}}$  for the  $\mu\mu(\gamma)\gamma_{\text{ISR}}$  (top) and  $\pi\pi(\gamma)\gamma_{\text{ISR}}$  (bottom) cross sections as a function of the  $\mu\mu$  and  $\pi\pi$  masses, respectively. Statistical errors only.

The offline event filtering involves a large number of specific selections, including dedicated  $\mu\mu\gamma$  filters. Whereas the inefficiency and its correction are negligible for muons, some inefficiency at the filtering stage is observed for pion events, mostly at low  $m_{\pi\pi}$  mass. This originates again from the overlap of tracks in the DCH and hadronic showers in the EMC. The correction  $C_{\text{trig}}$  to the  $\pi\pi(\gamma)\gamma_{\text{ISR}}$  cross section (Fig. 5, bottom) is found to be  $(1.0 \pm 0.3 \pm 0.3)\%$  at  $m_{\pi\pi} \sim 0.4 \text{ GeV}/c^2$  and  $(2.9 \pm 0.1 \pm 1.0) \times 10^{-3}$  at the  $\rho$  peak, where the first error is statistical and the second systematic. Beyond  $1.5 \text{ GeV}/c^2$ , the background level precludes a significant measurement of the efficiency with data and no correction is applied; a systematic error of  $0.4 \times 10^{-3}$  is assigned in the high mass range, equal to the inefficiency observed in MC. Because of imperfect simulation of hadronic showers, filtering is the major source of trigger systematic uncertainties in the pion channel.

Systematic errors due to the trigger and filter are reported in Tables II and V for muon and pion channels, respectively.

### C. Tracking

The tracking control samples of  $\mu\mu\gamma_{\text{ISR}}$  ( $\pi\pi\gamma_{\text{ISR}}$ ) events are selected through the efficiency-dedicated 1C fit described above. The rate of predicted tracks that are actually reconstructed in the tracking system, with a charge opposite to that of the primary track, yields the tracking efficiency.

To ensure the validity of the measurement, further criteria are applied to the tracking sample in addition to the kinematic fit. To enhance purity, a  $\pi^0$  veto is applied if a pair of additional photons in the event can form a  $\pi^0$  candidate with mass within  $15 \text{ MeV}/c^2$  of the nominal mass. This  $\pi^0$  veto is not applied to the pion tracking sample, because of the bias it would introduce on the inefficiency related to secondary interactions. The events are required to pass the triggers and online filter and are selected without specific requirements on the second reconstructed track, if any. Biases affecting the tracking-efficiency measurement introduced by the primary-track selection or event-level background-rejection criteria are identified and studied with simulation, and evaluated with data.

The predicted track is required to lie within the tracking acceptance, taking into account the effect of angular and momentum resolution. The method therefore determines the efficiency to reconstruct a given track in the SVT + DCH system within a specified geometrical acceptance, no matter how close or distant this track is with respect to the expected one, due for instance to decays or secondary interactions. However, the possible mismatch in momentum and/or angles affects the full kinematic reconstruction of the event, and its effect is included in the efficiency of the corresponding  $\chi^2$  selection applied to

the physics sample (Sec. VB4). Likewise, effects from pion decays in the detector volume are included in the pion-identification efficiency.

The individual track efficiency is determined assuming that the efficiencies of the two tracks are uncorrelated. However, the tracking efficiency is observed to be sharply reduced for overlapping tracks in the DCH, as measured by the two-track opening angle ( $\Delta\phi$ ) in the plane transverse to the beams. Not only is the individual track efficiency locally reduced, but a correlated loss of the two tracks is observed. In addition, as the final physics sample is required to have two and only two good tracks with opposite charge, the understanding of the tracking involves not only track losses, but also the probability to reconstruct extra tracks as a result of secondary interactions with the detector material or the presence of beam-background tracks. The full tracking efficiency is then the product of the square of the single-track efficiencies, the probability for not losing the two tracks in a correlated way (loss probability =  $f_0$ ), and the probability for not having an extra reconstructed track (loss probability =  $f_3$ ). The event correction  $C_{\text{track}}$  to be applied to the MC is the corresponding product of the data/MC ratios of each term. The mass-dependent quantities  $f_0$  and  $f_3$  are in the  $(0.5\text{--}2.5) \times 10^{-3}$  range.

For muons the single-track inefficiency and the data/MC correction are driven by the DCH overlap effect. At the maximum overlap ( $m_{\mu\mu} \sim 0.4 \text{ GeV}/c^2$ ) the inefficiency reaches 1.7% in simulation, but 2.5% in data, while the intrinsic reconstruction, measured for nonoverlapping tracks, accounts for an inefficiency of  $2.5 \times 10^{-3}$  in data, and  $5 \times 10^{-4}$  in simulation.

Because of backgrounds, the pion tracking efficiency can be obtained directly from data only in the  $\rho$  peak region, from  $0.6$  to  $0.9 \text{ GeV}/c^2$ . The main sources of track loss are identified: the track overlap in the DCH and the secondary interactions. The two effects are separated using the  $\Delta\phi$  distribution. This two-component model is used to extrapolate the inefficiency to mass regions outside the  $\rho$  peak. Results for pions are qualitatively similar to those for muons, with inefficiencies driven by the track overlap effects. The intrinsic track inefficiency is dominated by secondary interactions (2.2% in data and 1.7% in simulation) and is thus much larger than for muons. Near  $0.4 \text{ GeV}/c^2$  the track inefficiency is determined to be 6.2% in data and 4.7% in simulation. Above  $1.2 \text{ GeV}/c^2$  for pions, where the data/MC correction is not expected to vary significantly, a systematic uncertainty of about 0.3% is assigned.

The final corrections  $C_{\text{track}}$  to the  $\mu\mu(\gamma)\gamma_{\text{ISR}}$  and  $\pi\pi(\gamma)\gamma_{\text{ISR}}$  cross sections are presented in Fig. 6.  $C_{\text{track}}$  differs from unity by about 1.6% (3.0%) at  $0.4 \text{ GeV}/c^2$ , and by 0.8% (1.5%) at  $1 \text{ GeV}/c^2$  for muons (pions). Statistical uncertainties from the efficiency measurements are indicated by point-to-point errors.

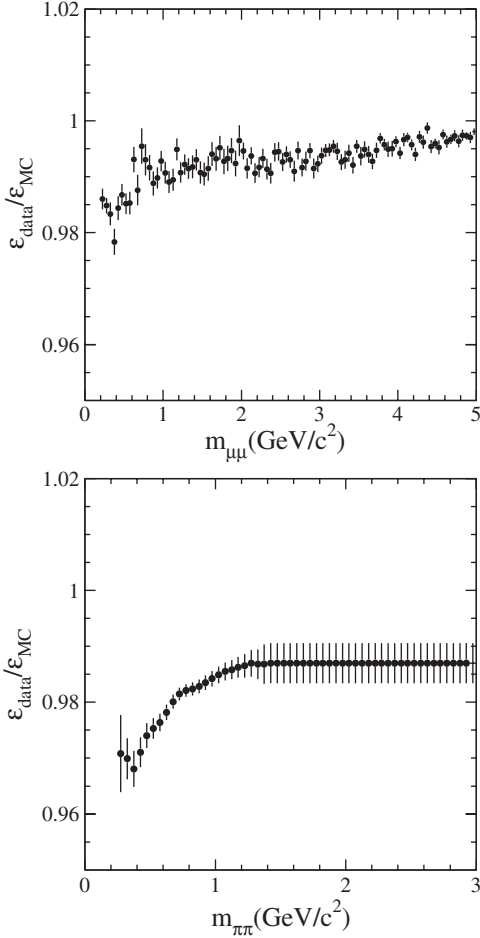


FIG. 6. The data/MC event tracking correction  $C_{\text{track}}$  for the  $\mu\mu(\gamma)\gamma_{\text{ISR}}$  (top) and  $\pi\pi(\gamma)\gamma_{\text{ISR}}$  (bottom) cross sections as a function of the  $\mu\mu$  and  $\pi\pi$  masses, respectively.

Systematic uncertainties are estimated from the study of biases in the method, determined using the simulation and calibrated with data-to-MC comparison of distributions characteristic of the physics source of the bias. Systematic uncertainties amount to  $0.8 \times 10^{-3}$  for muons in the mass range from 0.4 to 1.0  $\text{GeV}/c^2$ , and are about a factor of 2 larger outside. For pions, the systematic uncertainty of the correction is  $1.1 \times 10^{-3}$  in the 0.6–0.9  $\text{GeV}/c^2$  mass range, increasing to  $2.1 \times 10^{-3}$  (0.4–0.6  $\text{GeV}/c^2$ ),  $3.8 \times 10^{-3}$  (below 0.4  $\text{GeV}/c^2$ ),  $1.7 \times 10^{-3}$  (0.9–1.2  $\text{GeV}/c^2$ ), and  $3.1 \times 10^{-3}$  (above 1.2  $\text{GeV}/c^2$ ).

#### D. Particle identification

The method to determine the PID efficiencies makes use of the  $x^+x^-\gamma_{\text{ISR}}$  sample itself, where one of the produced charged  $x$  particles ( $x = \mu, \pi, K$ ) is tagged using strict identification criteria, and the second (“opposite”) track identification is probed (“tag-and-probe” method). The events are selected through a 1C kinematic fit that uses only the two tracks, with assumed mass  $m_x$ . The requirement  $\chi^2_{xx} < 15$  is applied to reduce multihadronic background. In this way the ensemble of opposite tracks

constitutes a pure  $x$  sample to be subjected to the identification process. The residual small impurity in the data samples is measured and corrected in the efficiency determination. The same analysis is performed on MC samples of pure  $x^+x^-\gamma_{\text{ISR}}$  events, and data/MC corrections  $C_{\text{PID}}$  are determined for each  $x$  type, as explained below. Since the PID efficiency measurement relies on two-track events that have passed the triggers,  $C_{\text{PID}}$  is not correlated with  $C_{\text{trig}}$  or  $C_{\text{track}}$ , as required by Eq. (7).

#### 1. Particle identification classes

Particle ID measurements in this analysis aim to obtain from data the values for all the elements  $\epsilon_{i \rightarrow j'}$  of the efficiency matrix, where  $i$  is the true  $e, \mu, \pi$ , or  $K$  identity and  $j'$  is the assigned ID from the PID procedure (Table I). Protons (antiprotons) are not included in the particle hypotheses because the  $p\bar{p}\gamma$  final state occurs only at a very small rate [22]. This contribution is estimated from simulation, normalized to data, and subtracted statistically from the mass spectra.

We identify muon candidates by applying criteria on several discriminant variables related to the track, such as the energy deposition  $E_{\text{cal}}$  in the EMC, and the track length, hit multiplicity, matching between hits and extrapolated track in the IFR. This defines the  $\mu_{\text{ID}}$  selector. The  $K_{\text{ID}}$  selector is constructed from a likelihood function using the distributions of  $dE/dx$  in the DCH and of the Cherenkov angle in the DIRC. The electron identification relies on a simple  $E_{\text{cal}}/p > 0.8$  requirement. As most of the electrons are vetoed at the preselection level, their fraction in the pion sample is generally small. Their contribution is completely negligible in the muon sample.

In addition to physical particle types, we assign an ID type of ‘0’ if the number of DIRC photons associated with the track ( $N_{\text{DIRC}}$ ) is insufficient to define a Cherenkov ring, thus preventing  $\pi$ - $K$  separation. The ID classes defined in Table I constitute a complete and orthogonal set that is convenient for studying cross-feed between different two-prong ISR final states.

TABLE I. Definition of particle ID types (first column) using combinations of experimental conditions (first row): “+” means “condition satisfied”, “−” means “condition not satisfied”, an empty box means “condition not applied”. The conditions  $\mu_{\text{ID}}$  and  $K_{\text{ID}}$  correspond to cut-based and likelihood-based selectors, respectively. The variables  $N_{\text{DIRC}}$  and  $E_{\text{cal}}$  correspond to the number of photons in the DIRC and the energy deposit in the EMC associated to the track, respectively.

	$\mu_{\text{ID}}$	$E_{\text{cal}}/p > 0.8$	$N_{\text{DIRC}} \leq 2$	$K_{\text{ID}}$
‘ $\mu$ ’	+			
‘ $e$ ’	−	+		
‘0’	−	−	+	
‘ $K$ ’	−	−	−	+
‘ $\pi$ ’	−	−	−	−

The  $\pi$ -ID selector is a set of negative conditions since no set of positive pion-ID criteria was found that provided both sufficient efficiency and purity. Pion candidates are tracks that do not satisfy any of the other ID class requirements. In this sense the pion-ID is sensitive to the problems affecting the identification of all the other particle types.

## 2. “Hard” pion-ID definition

The standard  $\pi$ -ID definition in Table I is part of a complete set of exclusive PID conditions that is convenient when backgrounds in the pion candidate sample are expected to be manageable. However, in some cases the standard  $\pi$ -ID algorithm does not deliver sufficient pion purity. One such case concerns the purity of the tagged pion in the tag-and-probe pion pair, which is crucial in the determination of  $\pi$ -ID efficiencies (Sec. IV D 5). Improved pion purity is also necessary to reduce backgrounds for the  $\pi\pi$  cross section measurement in mass regions in the tails of the  $\rho$  peak.

A tighter pion-ID selector is thus developed, which we call the hard pion ( $\pi_h$ ) selector, to improve the rejection of muons and electrons that are misidentified as pions with the standard definition. The  $\pi_h$ -ID is based on two likelihood functions  $P_{\pi/\mu}$  and  $P_{\pi/e}$ .  $P_{\pi/\mu}$  uses the EMC deposit  $E_{\text{cal}}$  associated with the track and the penetration of the track into the IFR, while  $P_{\pi/e}$  uses  $E_{\text{cal}}$  and the measurements of  $(dE/dx)_{\text{DCH}}$  and  $(dE/dx)_{\text{SVT}}$  as a function of momentum. Tracks with likelihoods close to 0 correspond to pions while  $P_{\pi/\mu} \sim 1$  ( $P_{\pi/e} \sim 1$ ) are muonlike (electronlike). Reference distributions used in the likelihoods are obtained from simulation, with corrections determined from data control samples in mass ranges that ensure backgrounds are negligible. The pure muon sample used for PID efficiency (see below), and the sample identified as ‘ $e\pi$ ’ in the very high mass range ( $m_{\pi\pi} > 5 \text{ GeV}/c^2$ ), provide the reference distributions for muons and electrons, respectively. The  $\pi\pi(\gamma)\gamma_{\text{ISR}}$  sample, with  $m_{\pi\pi}$  restricted to the  $\rho$  peak and with both pions satisfying the standard  $\pi$ -ID, provides the reference distributions for pions.

## 3. PID measurements with the muon samples

The method used to determine the muon ID efficiency utilizes the  $\mu\mu(\gamma)\gamma_{\text{ISR}}$  sample itself, where one of the tracks is tagged as a muon using the  $\mu_{\text{ID}}$  selector defined above, and the opposite track is probed. The sample is restricted to  $m_{\mu\mu} > 2.5 \text{ GeV}/c^2$  to reduce the non- $\mu$  background to the  $(1.1 \pm 0.1) \times 10^{-3}$  level, so that the ensemble of opposite tracks constitutes a pure muon sample.

The IFR performance at the time the data for this paper were collected was nonuniform across the detector and deteriorated with time.<sup>3</sup> In order to map the PID efficiency,

the track to be probed is extrapolated to the IFR. Local coordinates  $(v_1, v_2)$  of the impact point are defined depending on the IFR geometry (barrel or endcaps). Efficiency maps are obtained for each of the four data-taking periods used in the analysis. The granularity of the three-dimensional (3D) maps is optimized as a function of momentum and local coordinates  $(p, v_1, v_2)$ , so that local variations of efficiencies are described with significant statistical precision.

The low-efficiency regions in the IFR are removed in order to keep as active areas only the regions where the  $\mu_{\text{ID}}$  efficiency was reasonably homogeneous. Removed portions include the crack areas between modules and some parts of the nominal active region where the IFR performance was strongly degraded. The definition of removed regions is run-dependent: in the first running period only cracks are removed (about 13% of the IFR solid angle), while in the fourth period an additional  $\sim 15\%$  is eliminated.

Because of the mass restriction applied to the muon control sample, the 3D maps provide the identification efficiency for isolated muon tracks. They parametrize the local performance of the IFR at the track impact point. However, at  $\mu\mu$  masses less than  $2.5 \text{ GeV}/c^2$ , tracks can become geometrically close to each other within the IFR and their respective ID efficiencies can be significantly affected. First, the efficiency is reduced with respect to the isolated track efficiency because the combination of the two sets of hits causes some of the criteria that enter the  $\mu_{\text{ID}}$  selector to fail. Also the single-hit readout of the two-dimensional strip structure of the IFR chambers leads to losses. Second, track overlap leads to a correlated loss of PID for both tracks, not accounted for by the product of their uncorrelated single-track inefficiencies registered in the maps.

The loss of efficiency and the correlated loss effects are studied and evaluated in data and in simulation using the two-track physics sample. Since the pion background in the data sample is large in the  $\rho$  mass range, the efficiencies are measured directly only in the mass regions in the resonance tails, and are then extrapolated to the  $\rho$  peak region ( $0.6\text{--}0.9 \text{ GeV}/c^2$ ). Possible bias from this procedure is studied with simulation and a systematic uncertainty of  $2.2 \times 10^{-3}$  is assigned. The efficiency loss (compared to the isolated muon efficiency) is determined using a muon-ID tagged track as for the high-mass sample. Results are stored in mass-dependent 2D maps as a function of the differences  $(\Delta v_1, \Delta v_2)$  between the impact points of the two tracks in the local IFR coordinate system. Background from pions and kaons is subtracted using simulation with data/MC corrections for the mis-ID probabilities. The efficiency loss is maximal for  $m_{\mu\mu} \sim 0.7 \text{ GeV}/c^2$  with a reduction of 8.4% of the single-track efficiency in data and 4.8% in simulation. The resulting muon-ID inefficiencies  $(1 - \epsilon_{\mu \rightarrow \mu})$  measured in data and simulation at  $0.4(1.0) \text{ GeV}/c^2$  are 7.7% (6.6%) and 4.2% (3.5%), respectively.

<sup>3</sup>This problem was remedied for data collected subsequently, through IFR detector upgrades.

The two-track sample with no identified muon is used to measure the correlated efficiency loss. Since the pion background is overwhelming large in that sample, the small dimuon component is extracted by applying the likelihood estimator described in Sec. IV D 2 to both tracks. The correlated muon-ID loss is found to be 1.4% in data and 0.3% in simulation, at  $m_{\mu\mu} \sim 0.7 \text{ GeV}/c^2$ . A systematic uncertainty of  $1.5 \times 10^{-3}$  is assigned to the data/MC correction. Both efficiency loss and correlated loss decrease for higher masses and vanish at  $2.5 \text{ GeV}/c^2$ .

The event data/MC corrections resulting from requiring muon-ID for both tracks are obtained separately for the different running periods. The overall correction is given in Fig. 7. The plotted errors are statistical only.

Systematic errors are estimated for the different data-taking periods. The overall systematic error from muon-ID on the  $\mu\mu(\gamma)\gamma_{\text{ISR}}$  cross section amounts to  $3.3 \times 10^{-3}$ . Muon-ID is the largest source of uncertainty in the muon analysis. The dominant contribution arises from the procedures used to estimate the efficiency loss and the correlated loss of the two muons.

The pure muon sample of opposite tracks is used to measure the mis-ID probabilities. The largest one is  $\epsilon_{\mu \rightarrow \pi}$ , very close to  $1 - \epsilon_{\mu \rightarrow \mu}$ . Therefore, the preceding results for muon-ID efficiency and data/MC corrections, including those for close tracks, translate to the muon mis-ID to ' $\pi$ '. The small mis-ID probabilities into particle types other than ' $\pi$ ' are estimated from additional studies. The  $\epsilon_{\mu \rightarrow K}$  mis-ID is smaller than 0.1% for momenta below  $3 \text{ GeV}/c$ , with a steep increase for larger momenta, reaching about 1% at  $5 \text{ GeV}/c$ , with a data/MC correction of 12%. Mis-ID probabilities to  $\epsilon_{\mu \rightarrow 0}$  and  $\epsilon_{\mu \rightarrow e}$  are 0.4% and less than 0.1%, respectively.

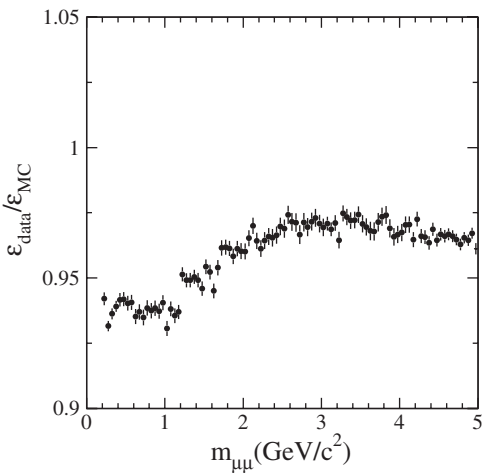


FIG. 7. The data/MC event correction  $C_{\text{PID}}$  for muon-ID efficiency as a function of  $m_{\mu\mu}$ .

#### 4. PID measurements with the kaon samples

For the kaon efficiency and mis-ID measurement, the same tag-and-probe method is used as described for the muons, this time with a primary track satisfying the  $K_{\text{ID}}$  condition. In addition to the restriction  $\chi^2_{KK} < 15$  applied to reduce multihadronic background, a requirement  $\chi^2_{KK} < \chi^2_{\pi\pi}$  is applied to reduce the pion contamination. The purity of the kaon sample is further enhanced by a restriction on the fitted  $m_{KK}$  mass, which must be in the  $\phi$  window  $1.01\text{--}1.04 \text{ GeV}/c^2$ . The electron background from photon conversions in the process  $e^+e^- \rightarrow \gamma\gamma$ , which populate the  $m_{KK}$  threshold region, is eliminated by a requirement on the distance (in the transverse plane) between the vertex of the two tracks and the beam axis. The purity achieved is  $(99.0 \pm 0.1)\%$ , determined from a fit of the  $m_{KK}$  distribution in data, with  $\phi$  signal and background shapes taken from MC.

The data/MC corrections for the  $K_{\text{ID}}$  efficiency are obtained as a function of track momentum. The restriction to the  $\phi$  sample imposes kinematic restrictions on the kaon momentum, with a lack of statistics below  $1.5 \text{ GeV}/c$  and above  $5 \text{ GeV}/c$ . This necessitates an extrapolation, which is achieved through a fit of the kinematically available data. A sampling of the momentum-dependent correction is performed using the  $KK\gamma_{\text{ISR}}$  MC simulation, in order to determine the event correction as a function of the  $m_{KK}$  invariant mass.

The mis-ID probabilities depend on momentum, especially for the  $K \rightarrow \pi$  mis-ID, which increases strongly for large momenta, where the  $K_{\text{ID}}$  selector becomes inefficient. At  $4 \text{ GeV}/c$  the values in data are 5.8% for  $K \rightarrow \mu$ , 16.1% for  $K \rightarrow \pi$ , and 0.7% for  $K \rightarrow e$ . The corresponding data/MC corrections are  $0.61 \pm 0.05$ ,  $0.87 \pm 0.04$ , and  $2.7 \pm 0.8$ .

#### 5. PID measurements with the pion samples

The tag-and-probe method is again applied to construct a pure pion sample used to measure the pion ID efficiency and misidentification probabilities. To reduce the backgrounds, the mass range of selected  $\pi\pi(\gamma)\gamma_{\text{ISR}}$  candidates is restricted to the  $\rho$  peak,  $0.6 < m_{\pi\pi} < 0.9 \text{ GeV}/c^2$ . To ensure the validity of the pion ID efficiency measurement, the purity of the pion ID sample is further increased by requiring the primary track to satisfy the hard pion tag. In the restricted mass range, the sum of  $\mu$ ,  $K$  and  $e$  backgrounds is reduced to the  $(3.7 \pm 0.5) \times 10^{-3}$  level.

While for muons it is possible to measure the ID efficiencies for isolated tracks using events with a large  $m_{\mu\mu}$  mass, for pions we use events in the  $\rho$  region. Tracks in this region may overlap in one detector or another. Thus the  $\pi$ -ID efficiencies and mis-ID probabilities contain some average of overlap effects, which are not possible to sort out in detail. However these effects are much reduced for pions compared to muons, since showering in the IFR is sufficient to distinguish hadrons from muons and the

overlap of pion showers does not degrade the pion-ID efficiency.

All  $\pi$ -ID efficiencies and mis-ID probabilities are stored in 2D maps as a function of the momentum and local  $z$  coordinate of the track extrapolated to the most relevant detector (IFR or DIRC). Biases from primary pion tagging and correlated two-track pion-ID loss are studied with simulation, and verified with data in the most critical cases. Both effects are at the  $10^{-3}$  level. The  $\pi$ -ID maps are sampled to build the full event efficiency distributions as a function of the  $m_{\pi\pi}$  mass, in data and MC. The event  $\pi$ -ID efficiency is weakly mass-dependent with typical values in data of 77.8%, 75.3%, and 77.0%, at masses of  $0.35 \text{ GeV}/c^2$ ,  $0.6 \text{ GeV}/c^2$ , and  $1 \text{ GeV}/c^2$ , respectively.

The data/MC correction to the full event  $\pi$ -ID efficiency is shown in Fig. 8. The correction is smaller than the corresponding factor for muons, which reflects a lesser sensitivity of the  $\pi$ -ID efficiency to the IFR conditions. Although it has been obtained using maps determined in the  $\rho$  region, it shows only a few percent variation with mass, consistent with the fact that correlated ID losses are small.

The systematic errors on the efficiencies come from the limited granularity of the mis-ID maps, the biases caused by the hard- $\pi$  selection of the tagged pion, and the application of maps determined in the  $\rho$  region ( $0.6\text{--}0.9 \text{ GeV}/c^2$ ) to other mass ranges. These effects are studied with simulated  $\pi\pi(\gamma)\gamma_{\text{ISR}}$  signal samples, by comparing the mass spectra of produced events when  $\pi$ -ID is either applied or not. The former spectrum is obtained by applying the PID process, then correcting the ' $\pi\pi$ ' spectrum by the  $\pi$ -ID efficiency determined as in data. The latter spectrum is obtained by not applying any PID requirement. As expected, the agreement is excellent in the  $\rho$  region with a variation of at most 2 permil, while some bias is observed in the lower and higher mass regions: 1% for  $m_{\pi\pi} < 0.4 \text{ GeV}/c^2$ ,  $6 \times 10^{-3}$  for  $0.4 < m_{\pi\pi} < 0.6 \text{ GeV}/c^2$ ,  $4 \times 10^{-3}$  for  $0.9 < m_{\pi\pi} < 1.2 \text{ GeV}/c^2$ ,

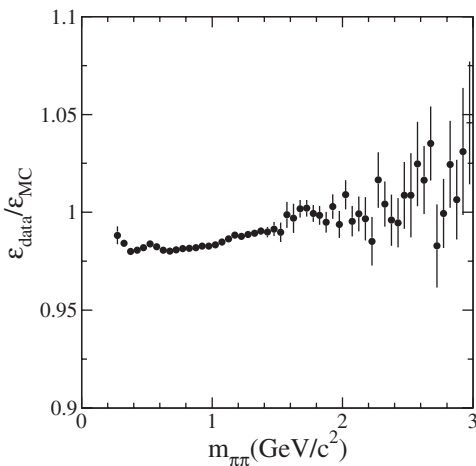


FIG. 8. The data/MC event correction  $C_{\text{PID}}$  for  $\pi$ -ID efficiency as a function of  $m_{\pi\pi}$ .

and 1% for  $m_{\pi\pi} > 1.2 \text{ GeV}/c^2$ . The full bias determined in simulation is taken as a systematic uncertainty. The global PID test in data described below supports this estimate.

In this analysis a good control of the  $\pi \rightarrow \mu$  mis-ID probability is crucial to the determination of the  $\mu\mu(\gamma)\gamma_{\text{ISR}}$  cross section in the  $\rho$  region. At track level this probability in data is found to vary with momentum between 4.5% at  $5 \text{ GeV}/c$  and 7% at  $1 \text{ GeV}/c$ , and the data/MC correction is determined to be  $0.95 \pm 0.05$  and  $1.23 \pm 0.03$ , respectively.

## 6. Global PID test with data

Since the PID classes form an exclusive and complete set, every event in the full sample before PID,  $N_{xx}$ , is assigned to a  $N_{ij}$  category ( $i, j = \mu, \pi, K, e, 0$ ). The observed  $N_{ij}$  spectra and the measured PID efficiencies are used in global consistency checks over the full  $N_{xx}$  data sample.

The  $N_{xx}$  sample is actually composed of  $N_{ii}$  pairs of particles of identical true types  $i = \mu, \pi, K$ , with small background contributions from other processes that are taken into account as follows. The contribution to  $N_{xx}$  from electrons stems from  $ee\gamma$  and  $\gamma\gamma$  followed by a pair conversion. It occurs mainly in the ' $\pi e$ ' and ' $\pi\pi$ ' topologies, while being negligible in ' $ee$ ' due to the strong rejection of electrons at the preselection and track definition levels. The small electron component of the ' $\pi\pi$ ' sample is subtracted out, after proper normalization (Sec. VI B 3). In the PID process, protons are mainly identified as ' $\pi$ ' and in the global test below, their very small contribution is included in  $N_{\pi\pi}$ . Because the  $N_{xx}$  sample is selected with a tight  $\chi^2_{\pi\pi} < 15$  requirement applied to the 1C fit, multihadronic background is reduced to a negligible level. Contributions from events with two tracks of different true types, from  $\tau$ -pair decays for instance, are found to be negligible.

Each observed ' $ii$ ' spectrum with "diagonal" ID, i.e., ' $\pi\pi$ ', ' $\mu\mu$ ', ' $KK$ ', receives contributions from the true ( $ii$ ) channel degraded by the  $\epsilon_{i \rightarrow i}$  efficiencies and from the two other channels through  $\epsilon_{j \rightarrow i}$  mis-ID. The spectra of produced events in each channel are thus obtained by solving a system of three linear equations. In each mass bin (computed with the  $\pi\pi$  mass hypothesis) of the spectra for identified pairs of type ' $i$ ',  $N_{ii}$ , the following equations:

$$\begin{aligned} N_{\pi\pi} &= N_{\mu\mu} \epsilon_{\mu\mu \rightarrow \pi\pi} + N_{\pi\pi} \epsilon_{\pi\pi \rightarrow \pi\pi} + N_{KK} \epsilon_{KK \rightarrow \pi\pi} \\ N_{\mu\mu} &= N_{\mu\mu} \epsilon_{\mu\mu \rightarrow \mu\mu} + N_{\pi\pi} \epsilon_{\pi\pi \rightarrow \mu\mu} + N_{KK} \epsilon_{KK \rightarrow \mu\mu} \\ N_{KK} &= N_{\mu\mu} \epsilon_{\mu\mu \rightarrow KK} + N_{\pi\pi} \epsilon_{\pi\pi \rightarrow KK} + N_{KK} \epsilon_{KK \rightarrow KK}, \end{aligned} \quad (8)$$

are solved for the produced numbers of particle pairs of each type,  $N_{\pi\pi}$ ,  $N_{\mu\mu}$ , and  $N_{KK}$ . In Eqs. (8), the quantities  $\epsilon_{jj \rightarrow ii}$  represent the product of the ID efficiencies  $\epsilon_{j \rightarrow i}$  and

possibly correlation factors that have been established in each PID study.

From the inferred spectra  $dN_{ii}/dm_{\pi\pi}$  of particle pairs of true type  $i$ , any ' $ij$ ' spectrum,  $dN_{ij}^{\text{pred}}/dm_{\pi\pi}$ , is derived, using the measured efficiencies and mis-ID probabilities, and is compared to the directly observed ' $ij$ ' distribution. A relative difference is computed, normalized to the spectrum  $dN_{xx}/dm_{\pi\pi}$  of the full sample before PID assignment:

$$\delta_{ij}^{\text{data}} = \frac{dN_{ij}^{\text{pred}}/dm_{\pi\pi} - dN_{ij}/dm_{\pi\pi}}{dN_{xx}/dm_{\pi\pi}}, \quad (9)$$

All differences  $\delta_{ij}^{\text{data}}$  are within a few permil.

The  $dN_{xx}/dm_{\pi\pi}$  spectrum is compared to the full inferred one,  $dN_{xx}^{\text{pred}}/dm_{\pi\pi}$ , obtained by summing the  $N_{\pi\pi}$ ,  $N_{\mu\mu}$  and  $N_{KK}$  components (and the small  $ee$  background). Figure 9, which shows their relative difference, contains all the information available in data on the validity of the ID corrections applied to the different ' $ii$ ' spectra. The band in Fig. 9 represents the limits given by the quadratic sum of the estimated systematic uncertainties on the  $\mu\mu$ ,  $\pi\pi$ , and  $KK$  ID efficiencies. Within the statistical uncertainties of the data sample, all deviations are consistent with the band, thus validating the estimates of the systematic errors.

### 7. Hard pion specific efficiency

The hard pion identification is required for one of the two tracks when computing the  $\pi^+\pi^-(\gamma)\gamma_{\text{ISR}}$  cross section off the  $\rho$  peak (Sec. IX B). The ' $\pi_h$ ' efficiency and misidentifications determined in simulation are controlled in data, and data-MC discrepancies are corrected for. The efficiency correction of the ' $\pi\pi \rightarrow \pi\pi_h$ ' identification can only be determined in the central  $\rho$  mass region where backgrounds are small in the ' $\pi\pi$ ' sample. Remaining  $\mu\mu$  backgrounds are subtracted from the ' $\pi\pi$ ' and ' $\pi\pi_h$ ' samples using the measured  $\epsilon_{\mu \rightarrow \pi}$  misidentification probability and the likelihood selector  $P_{\pi/\mu}$  defined in Sec. IV D 2, respectively.

Compared to the standard ' $\pi\pi$ ' definition, the event ID efficiency is reduced by a factor of 0.825 in data and 0.870 in simulation. The ratio of the efficiencies in data and simulation is shown in Fig. 10, exhibiting no significant mass dependence between 0.4 and 1  $\text{GeV}/c^2$ . A decrease is observed above 1  $\text{GeV}/c^2$ , which is ascribed to an imperfect representation of the large background in this region for the ' $\pi\pi$ ' sample. A linear fit is performed for  $0.6 < m_{\pi\pi} < 0.9 \text{ GeV}/c^2$  and extrapolated outside with propagation of errors.

### 8. Separation of the different channels using particle identification

As shown above for the global PID test on data, the PID efficiencies and misidentification probabilities measured on pure data samples allow one to reliably separate the different two-body ISR channels composing the full physics sample before PID assignment. Equivalently stated, by solving

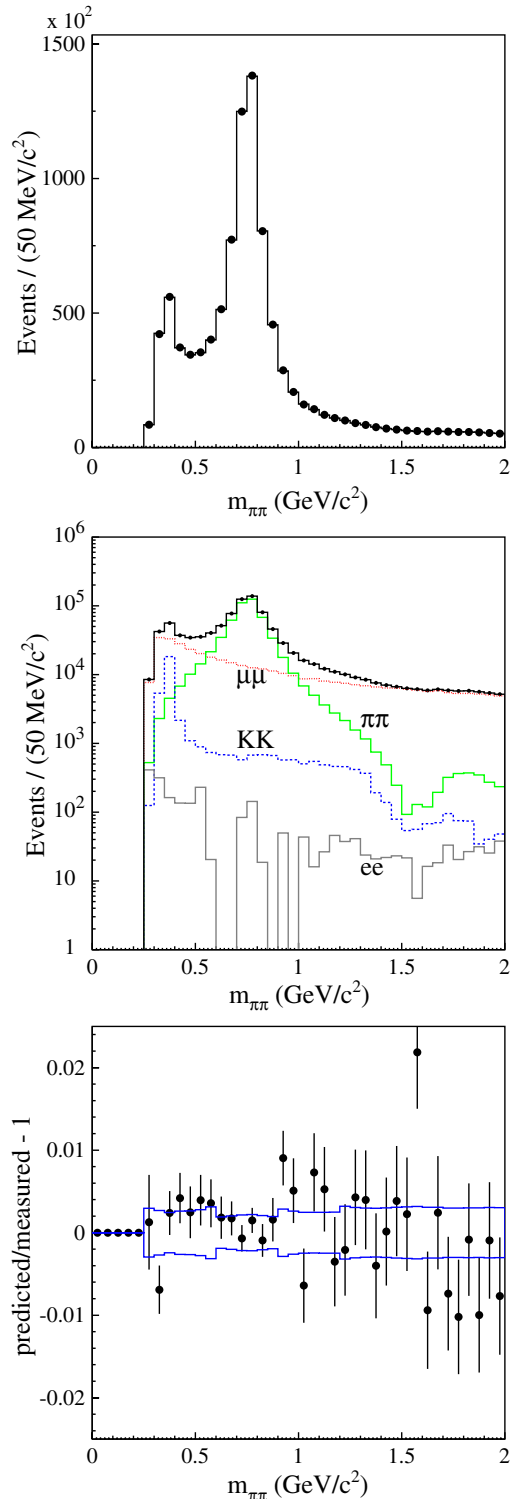


FIG. 9 (color online). Global PID test on data (see text). (top): The  $m_{\pi\pi}$  spectrum of all  $xx\gamma$  events (no PID applied, data points) compared to  $dN_{xx}^{\text{pred}}/dm_{\pi\pi}$  (histogram). (middle): The different components  $N_{xx}$  of the histogram in the top plot, with  $xx$  labels indicated, and their sum (top histogram with dots). (bottom): The relative difference between the two spectra in the top plot: predicted/measured  $-1$ . The independently estimated systematic uncertainty is shown by the band.

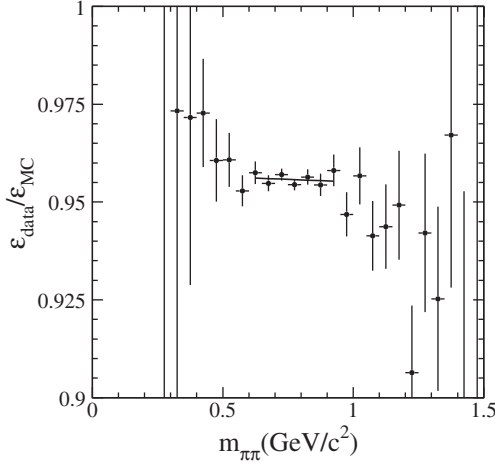


FIG. 10. The ratio of the efficiencies for ' $\pi\pi_h$ ' identification of  $\pi\pi(\gamma)\gamma_{\text{ISR}}$  events for data and MC, the line is the linear fit result in the  $\rho$  region.

Eqs. (8) on the total physical sample, one obtains the produced spectrum  $dN_{\pi\pi}/dm_{\pi\pi}$  free of misidentified  $\mu\mu(\gamma)\gamma_{\text{ISR}}$  and  $KK(\gamma)\gamma_{\text{ISR}}$  backgrounds. Likewise, the produced muon spectrum  $dN_{\mu\mu}/dm_{\mu\mu}$  is obtained free of hadronic backgrounds by solving Eqs. (8) per bin of  $m_{\mu\mu}$ .

The measured ' $\pi\pi$ ' and ' $KK$ ' spectra contain contributions from multihadronic background, from higher-multiplicity ISR or  $q\bar{q}$  processes, which are subtracted after solving Eqs. (8). There is a contribution from the ISR  $p\bar{p}\gamma$  process, which appears dominantly in the ' $\pi\pi'$  spectrum. In this procedure it is treated like pion pairs and is removed later. Mistreatment of multihadron events where the final state involves a  $K\pi$  pair is also considered, although they are reduced by PID.

The procedure of solving Eqs. (8) to separate the two-body ISR channels is applied to isolate the  $\mu\mu(\gamma)\gamma_{\text{ISR}}$

channel over the full mass range, and the  $\pi\pi(\gamma)\gamma_{\text{ISR}}$  channel in the  $\rho$  peak region. As the method relies on the completeness of PID class assignment of Table I, it does not apply when the ' $\pi\pi_h$ ' selection is required off the  $\rho$  peak in the  $\pi\pi(\gamma)\gamma_{\text{ISR}}$  channel. In the latter mass regions, the  $\mu\mu(\gamma)\gamma_{\text{ISR}}$  and  $KK(\gamma)\gamma_{\text{ISR}}$  background subtraction is achieved differently as described in Sec. IV.

## V. EFFICIENCY STUDIES (II)

Although the ISR and FSR kinematic fits described in Sec. III B take into account potential additional photons, inadequate description of NLO radiation by the simulation might induce incorrect estimates of the 2D- $\chi^2$  efficiency by MC. Comparisons of additional radiation in data and MC are performed and data-to-MC corrections of efficiencies are applied, as detailed below.

### A. Additional radiation

#### 1. Additional small-angle ISR

Additional radiation by the incoming electrons and positrons is evidenced by the tail seen along the  $\chi^2_{\text{FSR}}$  vertical axis in Fig. 2 for pions and Fig. 3 for muons. In order to study the  $\chi^2_{\text{ISR}}$  distributions in data and simulation, events are selected above the diagonal ( $\ln(\chi^2_{\text{FSR}} + 1) > \ln(\chi^2_{\text{ISR}} + 1)$ ) and the restriction  $E_{\gamma_{\text{add},\text{ISR}}}^* > 0.2$  GeV is applied to ensure a significant level of extra radiation. The quantity  $E_{\gamma_{\text{add},\text{ISR}}}^*$  is obtained from the 2C ISR fit described in Sec. III B.

The  $\chi^2_{\text{ISR}}$  distributions for the selected events are shown in Fig. 11. As expected for an ISR effect, the situation is found to be identical in the muon and pion channels. The data distributions are wider than the MC ones. This is a consequence of the ISR fit hypothesis that additional ISR photons are collinear to the beams as assumed in the AfkQed simulation, as opposed to the angular distribution of additional ISR in data.

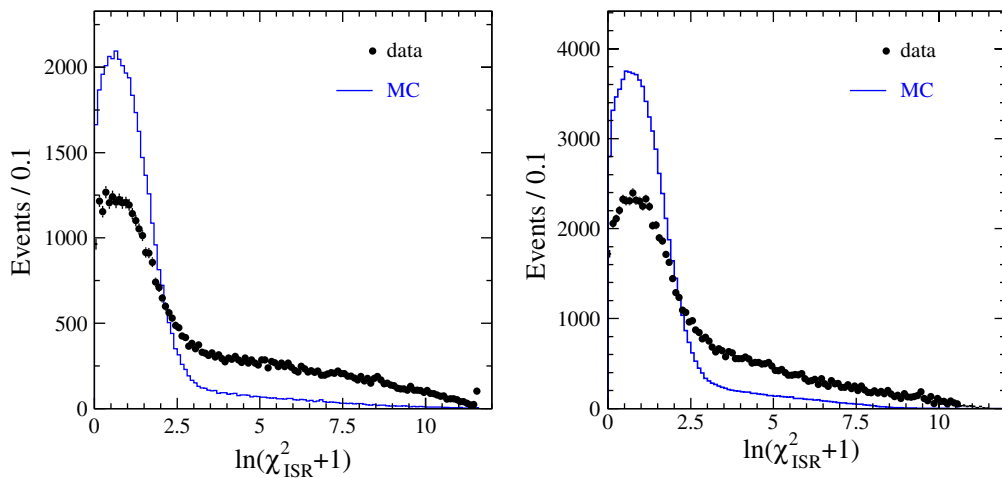


FIG. 11 (color online). Distributions of  $\ln(\chi^2_{\text{ISR}} + 1)$  for  $\mu\mu(\gamma)\gamma_{\text{ISR}}$  (left) and  $\pi\pi(\gamma)\gamma_{\text{ISR}}$  (right) events in the  $0.2$ – $1$   $\text{GeV}/c^2$  ( $0.5$ – $1$   $\text{GeV}/c^2$ ) mass region for muons (pions), selected with  $\ln(\chi^2_{\text{FSR}} + 1) > \ln(\chi^2_{\text{ISR}} + 1)$  and  $E_{\gamma_{\text{add},\text{ISR}}}^* > 0.2$  GeV for data (black points with errors) and MC (blue histogram). The distributions are normalized to the data luminosity.

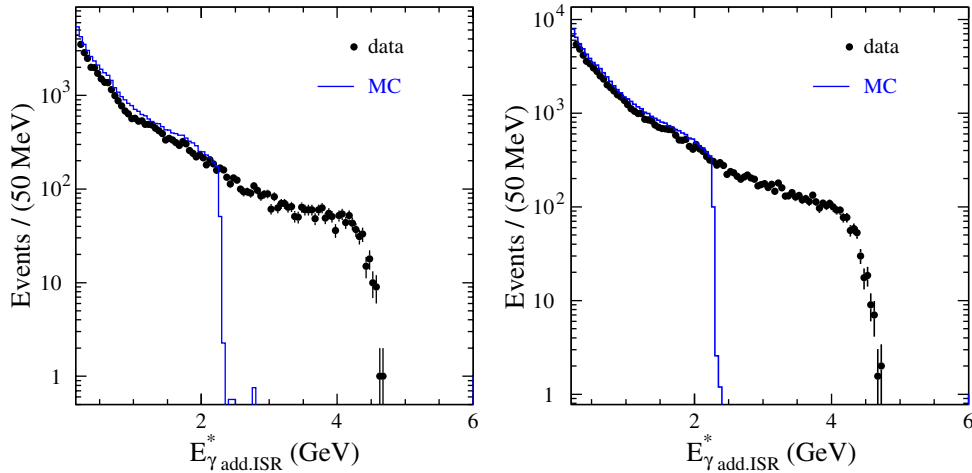


FIG. 12 (color online). Distributions of  $E_{\gamma \text{add.ISR}}^*$  for  $\mu\mu(\gamma)\gamma_{\text{ISR}}$  (left) and  $\pi\pi(\gamma)\gamma_{\text{ISR}}$  (right) events in the  $0.2\text{--}1\text{ GeV}/c^2$  ( $0.5\text{--}1\text{ GeV}/c^2$ ) mass region for muons (pions), selected with  $\ln(\chi_{\text{FSR}}^2 + 1) > \ln(\chi_{\text{ISR}}^2 + 1)$  and  $E_{\gamma \text{add.ISR}}^* > 0.2\text{ GeV}$  for data (black points with errors) and MC (blue histogram). The distributions are normalized to the data luminosity.

The corresponding distributions of  $E_{\gamma \text{add.ISR}}^*$ , normalized to the data luminosity, are given in Fig. 12 for muon and pion channels. The MC spectra stop at 2.3 GeV as a result of the  $m_{X\gamma_{\text{ISR}}} > 8\text{ GeV}/c^2$  requirement used in AfkQed at generation, while the data distributions extend to the kinematic limit. Below 2.3 GeV the data and MC distributions agree well in shape, but MC is a little higher than data. This is expected since MC includes all additional ISR photons, while events in data where the additional ISR photon is at large angle have good  $\chi_{\text{FSR}}^2$  and therefore are not present in the sample considered in this section.

The results found for additional ISR in  $\pi\pi(\gamma)\gamma_{\text{ISR}}$  and  $\mu\mu(\gamma)\gamma_{\text{ISR}}$  channels are in agreement, as expected from the factorization of additional ISR. The lack of angular distribution in AfkQed is studied at the 4-vector level using Phokhara, and acceptance corrections estimated,

but its effect essentially cancels in the  $\pi\pi/\mu\mu$  ratio (Sec. VIII A 4).

## 2. Additional FSR and large-angle ISR

Similarly, we select a sample of events with an extra photon in the detector acceptance and compares additional FSR in data and in the simulation where it is generated using PHOTOS. Events are selected with  $\ln(\chi_{\text{FSR}}^2 + 1) < \ln(\chi_{\text{ISR}}^2 + 1)$  and the fitted energy of the additional large-angle photon is restricted to  $E_{\gamma \text{add.FSR}} > 0.2\text{ GeV}$  in the laboratory frame. The request for a large-energy additional FSR photon effectively restricts the 2D- $\chi^2$  plane to a region  $\ln(\chi_{\text{FSR}}^2 + 1) \geq 3$ .

The corresponding  $\chi_{\text{FSR}}^2$  distributions for  $\mu\mu\gamma\gamma_{\text{ISR}}$  data and MC shown in Fig. 13 (left) are in reasonable agreement. Distributions for the selected  $\pi\pi\gamma\gamma_{\text{ISR}}$  events show

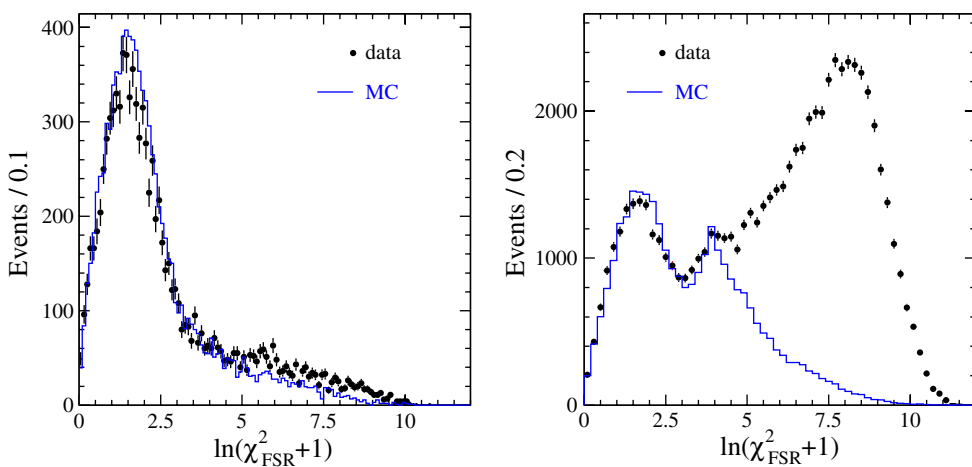


FIG. 13 (color online). Distributions of  $\ln(\chi_{\text{FSR}}^2 + 1)$  for  $\mu\mu\gamma\gamma_{\text{ISR}}$  (left) and  $\pi\pi\gamma\gamma_{\text{ISR}}$  (right) events, selected with  $\ln(\chi_{\text{FSR}}^2 + 1) < \ln(\chi_{\text{ISR}}^2 + 1)$  and  $E_{\gamma \text{add.FSR}} > 0.2\text{ GeV}$  for data (black points with errors) and MC (blue histogram). The mass regions are chosen to be similar for muons ( $0.2\text{--}1\text{ GeV}/c^2$ ) and pions ( $0.5\text{--}1\text{ GeV}/c^2$ ); the MC distribution is normalized to the number of events in data for muons and with  $\ln(\chi_{\text{FSR}}^2 + 1) < 2$  for pions.

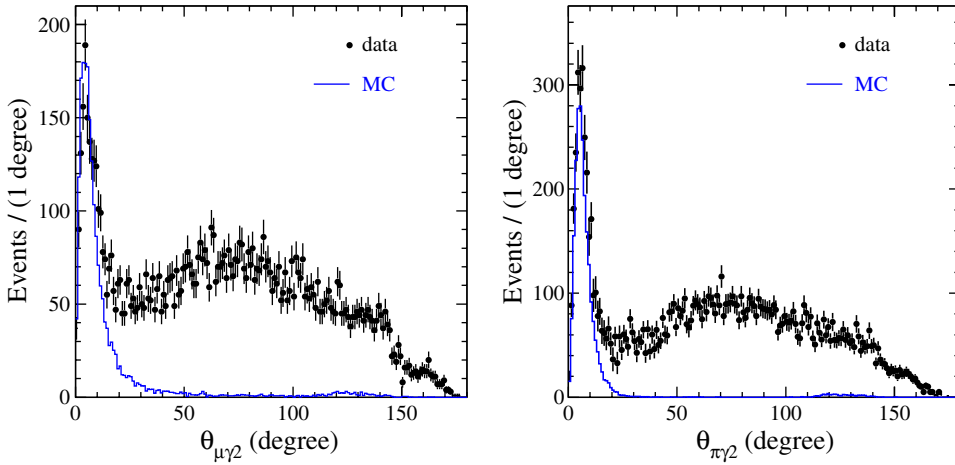


FIG. 14 (color online). The additional “FSR” photon angular distribution with respect to the closer outgoing muon for the  $\mu\mu\gamma\gamma_{\text{ISR}}$  (left) and background-subtracted  $\pi\pi\gamma\gamma_{\text{ISR}}$  (right) events with  $\ln(\chi^2_{\text{FSR}} + 1) < \ln(\chi^2_{\text{ISR}} + 1)$ ,  $E_{\gamma \text{ add.FSR}} > 0.2 \text{ GeV}$ ,  $\ln(\chi^2_{\text{FSR}} + 1) < 2.5$ , and in the mass intervals  $0.2 < m_{\mu\mu} < 1 \text{ GeV}/c^2$ ,  $0.5 < m_{\pi\pi} < 1 \text{ GeV}/c^2$  (data: black points with errors, MC: blue histogram). The mass regions are chosen to be similar for the muon and pion samples and the MC is normalized to data luminosity.

a similar agreement, Fig. 13 (right), except in the large  $\chi^2$  tail where there are contributions from background in the data. A contribution from secondary interactions is seen both in data and simulation.

The components of large-angle ISR and FSR are identified looking at the extra photon angular distribution with respect to the outgoing charged particles. Figure 14 (left) shows the distribution of  $\theta_{\mu\gamma_2}$ , the smallest of the two angles with either muon for  $m_{\mu\mu} < 1 \text{ GeV}/c^2$ . A clear peak is observed at small photon-muon angle, thus indicating a true FSR signal in data in agreement with the simulation. Evidence for large-angle ISR is also seen in data, at variance with AfkQed. This major discrepancy is expected, as additional ISR in AfkQed is constrained to be collinear

with the beams. The same situation is observed for pions. After subtraction of a residual background from the ISR  $\pi^+\pi^-\pi^0\gamma$  process, the FSR peaks in data and MC are in fair agreement [Fig. 14 (right)].

The photon energy distributions for the  $\mu\mu\gamma\gamma_{\text{ISR}}$  data and MC samples are given in Fig. 15 (left) for the subsamples satisfying the requirement  $\theta_{\mu\gamma_2} < 20^\circ$ . The main component of this subsample is from FSR but a contribution from large-angle ISR is estimated from the  $\theta_{\mu\gamma_2}$  distribution and taken with a 25% systematic uncertainty. Absolute rates in data and MC are compared, showing a good agreement up to  $E_{\gamma \text{ add.FSR}} \sim 2 \text{ GeV}$ , and a small excess in data in the tail above. After correction for the remaining ISR contribution below  $20^\circ$ , the ratio data/MC

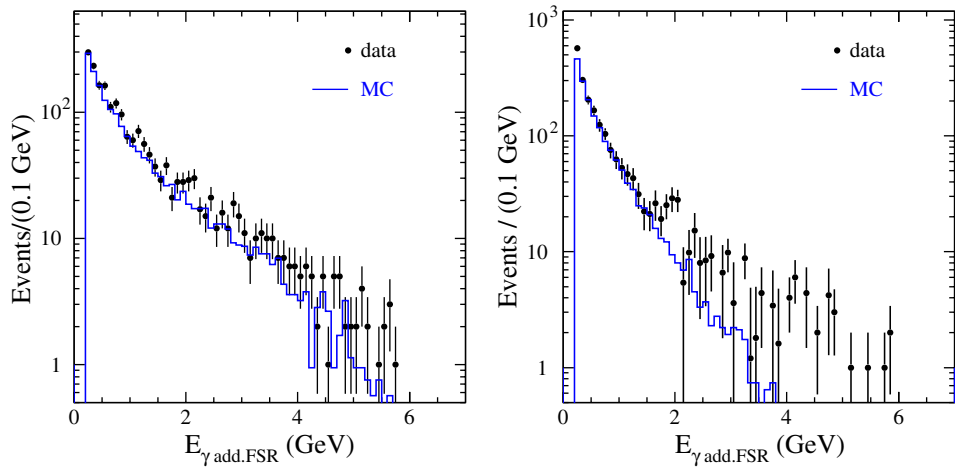


FIG. 15 (color online). The additional FSR photon energy distributions for the  $\mu\mu\gamma\gamma_{\text{ISR}}$  (left) and background-subtracted  $\pi\pi\gamma\gamma_{\text{ISR}}$  (right) events with  $\ln(\chi^2_{\text{FSR}} + 1) < \ln(\chi^2_{\text{ISR}} + 1)$ ,  $E_{\gamma \text{ add.FSR}} > 0.2 \text{ GeV}$ ,  $\ln(\chi^2_{\text{FSR}} + 1) < 2.5$ , in the mass intervals  $0.2 < m_{\mu\mu} < 1 \text{ GeV}/c^2$ ,  $0.5 < m_{\pi\pi} < 1 \text{ GeV}/c^2$ , and  $\theta_{\mu\gamma_2} < 20^\circ$ ,  $\theta_{\pi\gamma_2} < 10^\circ$  (data: black points with errors, MC: blue histogram). The mass regions are chosen to be similar for the muon and pion samples and the MC is normalized to data luminosity.

for the fraction of additional FSR amounts to  $0.96 \pm 0.06$ . Therefore the use of PHOTOS to generate FSR photons is in good agreement with data and adequate for our precision goal, since the uncertainty on the FSR rate represents about  $8 \times 10^{-4}$  of the total  $\mu\mu(\gamma)\gamma_{\text{ISR}}$  sample.

Figure 15 (right) shows the same distributions for pions after subtraction of the residual  $\pi^+\pi^-\pi^0\gamma$  background. From the comparison of data and MC events in the FSR region defined by  $\ln(\chi^2_{\text{FSR}} + 1) < \ln(\chi^2_{\text{ISR}} + 1)$ ,  $E_{\gamma \text{add,FSR}} > 0.2 \text{ GeV}$ , and  $\theta_{\pi\gamma_2} < 10^\circ$ , some excess is observed in  $\pi\pi(\gamma)\gamma_{\text{ISR}}$  data with respect to the PHOTOS expectation. In the  $0.5\text{--}1.0 \text{ GeV}/c^2$  mass range, the excess is  $(21 \pm 5)\%$ , taking into account subtraction of background and the large-angle ISR contribution. This difference is accounted for in the determination of the  $\chi^2$  selection efficiency, as discussed below.

## B. $\chi^2$ selection efficiency

### 1. Overview for $\pi\pi(\gamma)\gamma_{\text{ISR}}$ and $\mu\mu(\gamma)\gamma_{\text{ISR}}$

After the hadronic channels are removed using the PID (Sec. IV D 8), the remaining background contributions to the  $\mu\mu(\gamma)\gamma_{\text{ISR}}$  sample are essentially from  $\tau\tau(\gamma)$  events with two muons in the final state, or one muon and a pion misidentified as “muon”. This contribution is small and well simulated, so it can be handled easily even in the background (BG) region of the 2D- $\chi^2$  plane (Sec. VI A). Thus the determination of the loose  $\chi^2$  selection efficiency is straightforward in the muon channel. In contrast, for the pion channel, it is not possible to directly measure the efficiency of the 2D- $\chi^2$  selection in data because of an overwhelming background in the rejected region (controlling the loose selection), even in the intermediate region (controlling the tight selection).

The rejected signal events with large  $\chi^2$  have several sources: (i) bad input to the kinematic fits, mostly from the direction of the ISR photon, (ii) tails of the  $\chi^2$  distributions of events with additional ISR or FSR, (iii) more than one additional photon (mostly ISR), and (iv) secondary interactions. Except for the last type that is specific to pions, the other sources are common to pions and muons. A very small difference is also expected for the tail of the FSR fit  $\chi^2$ , as the FSR level is slightly different for pions and muons. However the level of additional FSR is measured in data and MC and the loss of events due to FSR can be controlled.

The strategy is hence to rely on the  $\chi^2$  selection studies performed on muon data to account for the common losses and to further investigate the losses specific to pions. Therefore the  $\chi^2$  selection efficiency in data is derived from the following expression:

$$\varepsilon_{\chi^2}^{\pi\pi(\gamma)\gamma_{\text{ISR}} \text{ data}} = \varepsilon_{\chi^2}^{\mu\mu(\gamma)\gamma_{\text{ISR}} \text{ data}} + \delta\varepsilon_{\chi^2}^{\pi/\mu}, \quad (10)$$

where the  $\mu/\pi$  correction term  $\delta\varepsilon_{\chi^2}^{\pi/\mu}$  accounts for two effects: (i) the difference in additional FSR between pions

and muons, and (ii) pion interactions. The contributions of the two components are separated, measured in the simulation, and corrected for data/MC discrepancies, according to the procedures outlined below.

### 2. Determination of the $\chi^2$ selection efficiency for $\mu\mu(\gamma)\gamma_{\text{ISR}}$

The efficiency of the 2D- $\chi^2$  selection is measured by the rate of  $\mu\mu(\gamma)\gamma_{\text{ISR}}$  events in the rejected region. The spectrum in the signal region is obtained in data by solving Eqs. (8) in each mass bin. The same procedure applied in the BG region yields directly the mass spectrum of produced muon events rejected by the loose  $\chi^2$  selection. A small contribution from  $\tau\tau$  must be explicitly subtracted using the simulation. The efficiency is directly deduced from the ratio of the two spectra.

Figure 16 gives the measured  $\chi^2$  efficiency as a function of  $m_{\mu\mu}$ . It is lower in data than the prediction from the simulation by 1.2%. Most of the discrepancy arises from

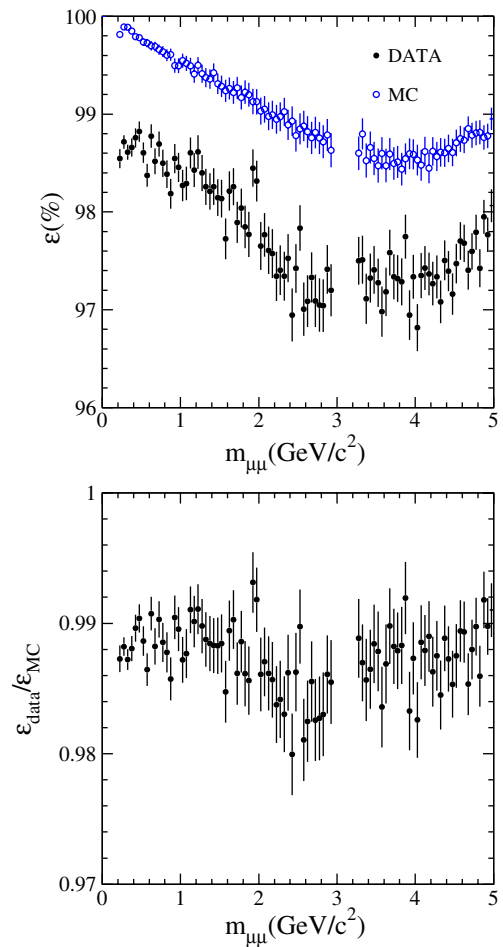


FIG. 16 (color online). The  $\chi^2$  efficiency (top) for  $\mu\mu(\gamma)\gamma_{\text{ISR}}$  data (after background subtraction), MC (AfkQed), and the ratio  $C_{\chi^2}$  of data to MC (bottom), as a function of  $m_{\mu\mu}$ . The gap at  $3.0\text{--}3.2 \text{ GeV}/c^2$  corresponds to the excluded  $J/\psi$  window (Sec. VI A).

the absence of large-angle ISR in AfkQed, which is present in data and generates some loss when the large- $\chi^2$  tails are removed, as expected from Fig. 11. Evidence for this loss appears at  $\mu\mu$  threshold where FSR vanishes, while in simulation the efficiency deviates from one by only  $5 \times 10^{-4}$ . The efficiency decrease with  $m_{\mu\mu}$  is due to the loss of large- $\chi^2$  FSR events and reflects the increasing rate of additional FSR photons with large energy ( $E_{\gamma, \text{add,FSR}} > 0.2 \text{ GeV}$ ). The same behavior is observed in data and simulation, consistent with the fact that additional FSR is well described in the simulation.

The systematic uncertainty on the determination of the  $\chi^2$  efficiency comes exclusively from the estimate of the background in the muon channel, due to the uncertainty on the  $\tau\tau$  cross section and on the PID  $\varepsilon_{j\rightarrow i}$  efficiencies. These uncertainties amount to a few  $\times 10^{-4}$  and are incorporated in the point-to-point errors.

### 3. Effect of additional FSR for pions

The first component in  $\delta\varepsilon_{\chi^2}^{\pi/\mu}$  comes from the difference in additional FSR between pions and muons. The difference in the FSR rate due to the  $\pi - \mu$  mass difference is observed in simulation at the expected level ( $\sim 25\%$ ) and the expected loss of efficiency due to additional FSR is consequently lower by that amount in  $\pi\pi(\gamma)\gamma_{\text{ISR}}$  with respect to  $\mu\mu(\gamma)\gamma_{\text{ISR}}$ .

The contribution of additional FSR to the  $\chi^2$  inefficiency is the product of the fraction of FSR events lost by the  $\chi^2$  selection times the rate of FSR events in the full pion data sample. To estimate this loss, one relies on the  $\chi^2_{\text{FSR}}$  distributions of the events with additional FSR as shown in Fig. 13. The shapes are similar in the muon and pion channels up to  $\ln(\chi^2_{\text{FSR}} + 1) = 2.5$  (which coincides with the lower edge of the “BG” region defined in Fig. 2), at which value the pion interaction component turns on. The shapes in data agree well with the MC shapes, over the entire distribution in  $\mu\mu(\gamma)\gamma_{\text{ISR}}$ , and, in  $\pi\pi(\gamma)\gamma_{\text{ISR}}$ , until the distribution in data is affected by background in addition to interactions. The fraction of FSR events lost in the pion channel is consequently estimated from the fraction of FSR events that fall beyond the  $\chi^2_{\text{FSR}}$  selection boundary in the muon data ( $(35 \pm 5)\%$ ). This fraction of lost FSR events is normalized to the rate of additional FSR events observed in the full pion MC sample in the  $\ln(\chi^2_{\text{FSR}} + 1) < 2.5$  region (0.64%). The loss is further corrected to account for the observed ( $21 \pm 5\%$ ) data/MC difference in FSR rates (Sec. V A 2).

The resulting data/MC correction to the loose  $\chi^2$  efficiency due to the pion-muon FSR difference is estimated to be  $(0.6 \pm 0.2) \times 10^{-3}$ . This correction is slightly overestimated as a fraction of the additional FSR events is in the signal region of the loose  $\chi^2$  criterion. The correction to the tight  $\chi^2$  selection efficiency is larger,  $(1.9 \pm 0.8) \times 10^{-3}$ , since all the FSR events with photon energy larger than

about 0.2 GeV are lost with the tight criterion ( $\ln(\chi^2_{\text{ISR}} + 1) < 3$ ).

### 4. Effect of pion interactions

The effects of secondary interactions are mostly seen in the tracking efficiency because of the tight requirements imposed on the track pointing to the interaction region. The small residual effect in the 2D- $\chi^2$  selection efficiency is estimated using the simulation, essentially by comparing the behavior of muon and pion events, and corrected for data-MC difference in interaction rates.

It is found in simulation that the difference of 2D- $\chi^2$  selection efficiencies,  $\delta\varepsilon_{\chi^2}^{\pi/\mu}$ , between  $\pi\pi(\gamma)\gamma_{\text{ISR}}$  and  $\mu\mu(\gamma)\gamma_{\text{ISR}}$  is about  $-1.2 \times 10^{-3}$  at  $0.75 \text{ GeV}/c^2$ . As we know that the loss of additional FSR events is smaller for pions, since the FSR rate is lower, the smaller efficiency in  $\pi\pi(\gamma)\gamma_{\text{ISR}}$  is ascribed to pion interactions. The  $\chi^2$  selection efficiency loss from secondary interactions estimated this way in simulation is  $(2.8 \pm 0.2) \times 10^{-3}$  for the loose criteria, flat with mass, and  $(1.4 \pm 0.1) \times 10^{-2}$  for the tight criteria, with some  $\pm 20\%$  relative variation with mass.

Two methods are considered to isolate interacting events in both data and MC, and data/MC corrections to the  $\chi^2$  efficiencies obtained above in simulation are estimated from the respective rates of pion interactions. The corresponding events populate the diagonal region in the 2D- $\chi^2$  plane, extending through the  $\chi^2$  selection boundary, and therefore affect the  $\chi^2$  selection efficiency.

In the first method, interactions are tagged by the presence of “bad” tracks (i.e., tracks not satisfying the track requirements of the ISR two-body analysis) in addition to the two good tracks of the selected events, provided a secondary vertex can be found between a bad track and one of the two good tracks. Because of the strict requirements on good tracks, most tagged interactions occur in the beam pipe, with further contributions from the first SVT layers. The data/MC ratio of interacting events estimated with this method is found to be  $1.44 \pm 0.10$  in the intermediate  $\chi^2$  region, and  $1.43 \pm 0.13$  in the background region. However the efficiency of this procedure to tag interacting pions is rather low since it keeps about 10% of the events with secondary interactions in the signal (loose) region and 25% in the background region.

The second method tags a much larger fraction of interacting events. The quantity  $\text{doca}_{xy}^{\max}$  is defined to be the largest of the  $\text{doca}_{xy}$  for the two tracks in the event, each limited by the requirement  $\text{doca}_{xy} < 0.5 \text{ cm}$  used in the good track definition (Sec. III). The sensitivity of this variable to secondary interactions can be appreciated in Fig. 17, showing a striking difference in the tail of the distributions for pions and muons. The same behavior is also observed between pions in events satisfying the tight or loose  $\chi^2$  criteria. The selection of events with

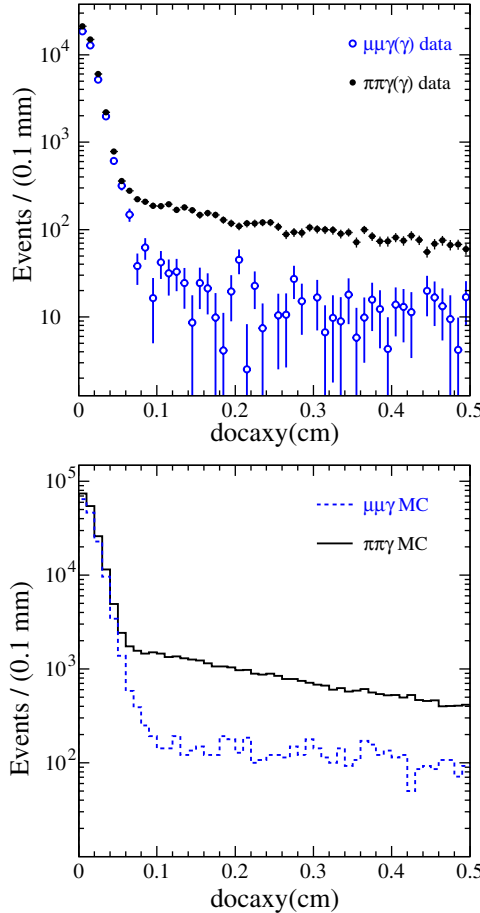


FIG. 17 (color online). (top): The distribution of the largest of the two transverse distances of closest approach to the interaction point  $\text{doca}_{xy}^{\text{max}}$  for pions and muons in data, for the intermediate  $\chi^2$  region. (bottom): Same distributions in simulation.

$\text{doca}_{xy}^{\text{max}} > 0.1 \text{ cm}$  retains about 50% of interactions, with a background from noninteracting events that is estimated from the muon distribution. Again it is found that the level of secondary interactions is underestimated in the simulation, with a data/MC ratio of  $1.52 \pm 0.03$  in the intermediate  $\chi^2$  region. A reliable determination cannot be achieved in the background region with this method, because of multihadronic background.

The second determination is more accurate and dominates the average data/MC ratio of interaction rates, which is  $1.51 \pm 0.03$ .

### 5. Summary of corrections to the $\chi^2$ selection efficiency for pions

Adding the two components of the  $\chi^2$  selection inefficiency in  $\pi\pi(\gamma)\gamma_{\text{ISR}}$  that are not common to the muon channel, the extra data/MC correction to apply to  $\delta\varepsilon_{\chi^2}^{\pi/\mu}$  for the loose  $\chi^2$  selection amounts to  $(1.4 \pm 0.1) \times 10^{-3}$  for secondary interactions and  $(0.6 \pm 0.2) \times 10^{-3}$  for FSR. The total correction is  $(2.0 \pm 0.3) \times 10^{-3}$ .

For the tight  $\chi^2$  selection, both corrections are larger:  $(7.1 \pm 0.4) \times 10^{-3}$  for interactions and  $(1.9 \pm 0.8) \times 10^{-3}$  for FSR. The total data/MC correction on the tight  $\chi^2$  selection efficiency amounts to  $(9.0 \pm 0.9) \times 10^{-3}$ .

## VI. BACKGROUNDS

### A. Backgrounds in the $\mu\mu(\gamma)\gamma_{\text{ISR}}$ channel

Contributions from hadrons to the ' $\mu\mu$ ' sample are removed by PID through solving Eqs. (8), as described in Sec. IV D 8, but one must still consider background from processes producing real muons.

ISR-produced  $J/\psi$  followed by decay to  $\mu\mu$  is not a background to the complete  $\mu\mu(\gamma)\gamma_{\text{ISR}}$  process, but is a background to the purely QED reaction used for the determination of the ISR luminosity. The  $\psi(2S)$  contributes as a background through its decays to  $J/\psi$ , either following the  $\pi^0\pi^0 J/\psi$  transition or radiative decays through charmonium states. Both direct and indirect  $J/\psi$  production is observed. These contributions are removed by excluding events where the measured invariant  $\mu\mu$  mass is in the  $3.0\text{--}3.2 \text{ GeV}/c^2$  window.<sup>4</sup>

Another hidden background from  $J/\psi$  comes from the radiative decay  $J/\psi \rightarrow \mu^+\mu^-\gamma$ , which is indeed barely observed in the  $\mu\mu\gamma$  mass spectrum in data. Its contribution to the  $\mu\mu$  mass spectrum between  $2$  and  $3 \text{ GeV}/c^2$  is of order  $10^{-3}$  and neglected.

The process  $e^+e^- \rightarrow \tau^+\tau^-(\gamma)$  can contribute to the ' $\mu\mu$ ' sample through  $\tau \rightarrow \mu\nu_\mu\nu_\tau$  and misidentified  $\tau \rightarrow \pi\nu_\tau$  decays. The contribution is estimated by MC and found to be negligibly small, except at masses above  $2 \text{ GeV}/c^2$  where it reaches a fraction of  $10^{-3}$ . It is subtracted using the simulation.

### B. Backgrounds in the $\pi\pi(\gamma)\gamma_{\text{ISR}}$ channel

#### 1. Background from $\mu\mu(\gamma)\gamma_{\text{ISR}}$

Separation of each component of the two-prong ISR sample is achieved through solving Eqs. (8) in each  $m_{\pi\pi}$  mass bin. This procedure yields the produced spectrum  $dN_{\pi\pi}/dm_{\pi\pi}$  and the background contributions to the observed ' $\pi\pi'$ -identified spectrum. The muon background level is less than  $4 \times 10^{-3}$  at the  $\rho$  peak but increases rapidly away from the resonance and reaches a few percent at the  $\rho$  tail boundaries (Table III).

As the ' $\pi\pi_h$ ' selection applied in mass ranges away from the  $\rho$  precludes using the above procedure, the reduced  $\mu\mu(\gamma)\gamma_{\text{ISR}}$  background contribution is determined directly from the ' $\pi\pi_h$ ' sample using the track identified as a ' $\pi$ ' with the standard pion identification. The fit of the distribution, for that track, of the  $\pi/\mu$  likelihood estimator  $P_{\pi/\mu}$  (introduced in Sec. IV D 2) yields the respective true

<sup>4</sup>In the final  $m_{\mu\mu}$  mass spectrum, this rejection does not however produce a sharp hole as  $m_{\mu\mu}$  is determined after the  $\mu\mu(\gamma)\gamma_{\text{ISR}}$  kinematic fits described in Sec. III B.

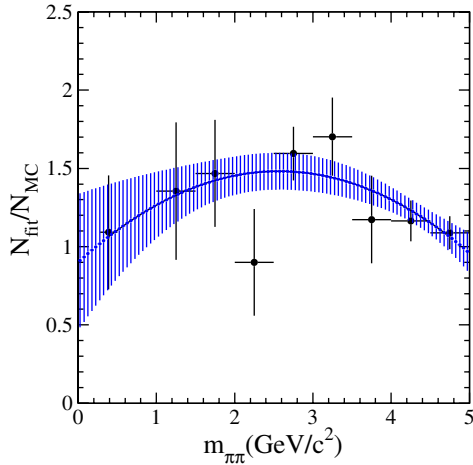


FIG. 18 (color online). The rate of  $\mu\mu$  events misidentified as ' $\pi\pi_h$ ' in data relative to the MC expectation, measured in mass intervals below and above the  $\rho$  region. The curve with the error band is a second-order polynomial fit to the data points, used to interpolate through the  $\rho$  mass region ( $0.6$ – $0.9$   $\text{GeV}/c^2$ ).

muon and pion components of the ' $\pi$ '-identified tracks, hence of the ' $\pi\pi_h$ ' sample. Fits are performed in  $0.5 \text{ GeV}/c^2$ -wide mass bins and, except for the  $0.5$ – $1 \text{ GeV}/c^2$  interval ( $\rho$  peak region), the  $\mu\mu$  component can be well determined. Above  $3 \text{ GeV}/c^2$  the muon contribution becomes dominant, despite the ' $\pi\pi_h$ ' ID, and the pion signal is lost above  $4 \text{ GeV}/c^2$ . The results of the fits are summarized in Fig. 18, which shows, for each mass interval, the  $\mu\mu \rightarrow \pi\pi_h$  fraction in data relative to the prediction from the simulated muon sample after luminosity scaling. A second-order polynomial fit to all points allows one to smoothly interpolate between the low and high-mass regions. The band indicates the error envelope of the fit.

## 2. Background from $KK(\gamma)\gamma_{\text{ISR}}$

When the standard  $\pi$ -ID identification is applied to both tracks in the ' $\pi\pi$ ' sample, the kaon background is implicitly subtracted through solving Eqs. (8) and stays below the permil level in the  $\rho$  peak region (Table III).

This background is essentially insensitive to the further selections applied to the ' $\pi\pi_h$ ' sample. Since the  $KK(\gamma)\gamma_{\text{ISR}}$  events are dominated by the narrow  $\phi$  resonance, one can use this feature to determine the  $KK$  component directly in data. The procedure is illustrated in Fig. 19, which shows the  $m_{KK}$  mass distribution of the ' $\pi\pi_h$ ' sample when the  $K$  mass is assigned to both tracks. A  $\phi$  signal is fitted with the signal line shape taken from simulation and a linear term to describe the dominant true  $\pi\pi$  component. The  $\phi$  signal yield provides the normalization of the remaining  $KK(\gamma)\gamma_{\text{ISR}}$  background contribution to be subtracted from the ' $\pi\pi_h$ ' data. The wide and distorted shape of the  $\phi$  peak reflection in the  $m_{\pi\pi}$  mass spectrum is taken from simulation.

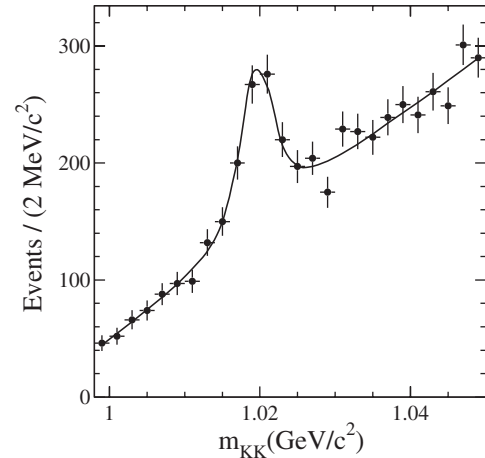


FIG. 19. The  $m_{KK}$  mass distribution in the ' $\pi\pi_h\gamma$ ' data sample. The solid line represents the result of the fit (see text).

## 3. Background from $ee\gamma$ events

Radiative Bhabha events are very strongly suppressed in the event selection because of the track definition that contains a veto on electrons. Remaining events of this type are from distribution tails and various pathologies. Because of this large selection bias there are very few events actually identified as ' $ee$ '  $\gamma$  in the identification process. Radiative Bhabha background appears in the ' $e\pi$ ' and ' $\pi\pi$ ' ID topologies. This background is identifiable near threshold and at high masses. Its small contribution cannot be detected in the  $\rho$  region and its mass shape and magnitude are estimated from a downscaled sample of radiative Bhabha events normalized near threshold.

The radiative Bhabha background normalization is achieved using the angular distribution in the  $\pi\pi$  center-of-mass system, assuming the pion mass for the particles. The angle  $\theta_\pi^*$  of the  $\pi^+$  is measured relative to the ISR photon direction in that frame. In the mass range  $0.28 < m_{\pi\pi} < 0.32 \text{ GeV}/c^2$  just above threshold, the remaining  $ee\gamma$  background contribution, still noticeable with the ' $\pi\pi_h$ ' identification, is obtained by fitting the  $|\cos\theta_\pi^*|$  distribution. Backgrounds from  $\mu\mu(\gamma)\gamma_{\text{ISR}}$  and  $KK(\gamma)\gamma_{\text{ISR}}$  are subtracted before fitting, with shapes taken from simulation with correction from the data, and normalized to data luminosity. The  $|\cos\theta_\pi^*|$  distribution is fitted with two components:  $\pi\pi(\gamma)\gamma_{\text{ISR}}$ , with the shape taken from the simulation, and  $ee\gamma$  background with the shape obtained from the down-scaled radiative Bhabha sample. The latter contribution has a characteristic sharp peak near one with a long tail while the  $\pi\pi(\gamma)\gamma_{\text{ISR}}$  signal behaves as  $\sin^2\theta_\pi^*$ . The fit shown in Fig. 20 on the ' $\pi\pi_h$ ' sample at threshold provides the normalization factor to be applied to the radiative Bhabha sample to describe the  $ee\gamma$  background. A similar fit performed at threshold on the ' $\pi\pi$ ' sample yields a consistent normalization factor.

The mass dependence of the  $ee\gamma$  background is checked using the sample of events identified as ' $e\pi$ '. The latter is a

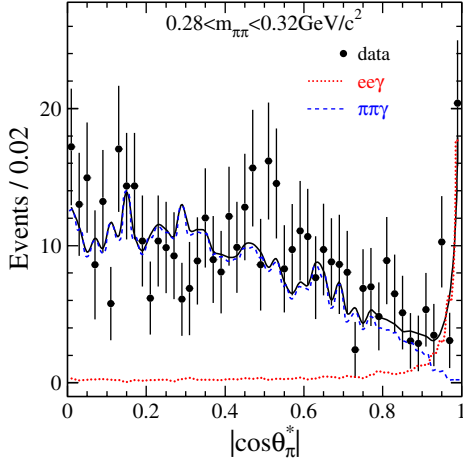


FIG. 20 (color online). The  $|\cos\theta_{\pi}^*|$  distribution of ' $\pi\pi_h$ ' data in the  $0.28$ – $0.32$   $\text{GeV}/c^2$   $m_{\pi\pi}$  range, fitted (black curve) to two free components:  $\pi\pi(\gamma)\gamma_{\text{ISR}}$  from MC (blue dashed line) and  $ee\gamma$  background from downscaled radiative Bhabha events (red dotted line). The small  $\mu\mu(\gamma)\gamma_{\text{ISR}}$  contribution is subtracted out.

rather pure  $ee\gamma$  sample outside the  $\rho$  region, and is more representative of events misidentified as ' $\pi\pi_h$ ' than the genuine radiative Bhabha downscaled sample. The ratio of the mass spectra of ' $e\pi$ ' events to the radiative Bhabha sample is found to be constant within uncertainties, for masses away from the  $\rho$  peak, i.e., just above threshold and in the  $1.5$ – $3$   $\text{GeV}/c^2$  range.

The  $ee\gamma$  background is only noticeable at threshold and near the edges of the  $\rho$  central region: 6% for  $m_{\pi\pi} < 0.32$   $\text{GeV}/c^2$  and less than 0.05% for larger masses for the ' $\pi\pi_h$ ' selection, and 0.63(0.27)% at  $m_{\pi\pi} = 0.525(0.975)$   $\text{GeV}/c^2$  for the ' $\pi\pi$ ' selection. At the  $\rho$  peak the fraction drops to only 0.03%.

A systematic uncertainty of 100% is assigned to the  $ee$  normalization factor determined at threshold, which is applied up to  $3$   $\text{GeV}/c^2$ . This precision is adequate in the  $\rho$  region as well as in the resonance tails.

#### 4. Conversions and rejection of displaced vertices

Purely electromagnetic processes may induce backgrounds when one of the final-state particles interacts with the detector material, allowing the selection criteria to be satisfied. This is the case at threshold from the  $e^+e^- \rightarrow \gamma\gamma$  process followed by a photon conversion, and at large masses from Bhabha scattering where one of final electrons (positrons) undergoes bremsstrahlung in the beam pipe. In either case, one or both of the detected tracks can be misidentified as pions. However, as they do not originate from the interaction point, this contamination is reduced by requiring the distance in the transverse plane  $V_{xy}$  of the vertex of the two tracks and the average interaction point to be small.

The background from conversions is expected to yield a rather wide  $V_{xy}$  distribution, while prompt particles (from  $ee\gamma$  and  $\pi\pi(\gamma)\gamma_{\text{ISR}}$ ) produce a peak at zero. The requirement  $V_{xy} < 0.5$  cm is applied in the  $\rho$  tails, which are the mass regions affected by the background from conversions. The conversions are reduced to a negligible level ( $< 5 \times 10^{-4}$ ) by the selection. The efficiency of the  $V_{xy}$  requirement for  $\pi\pi(\gamma)\gamma_{\text{ISR}}$  events is controlled by the two-track vertexing and pion secondary interactions. The former effect is studied in data and simulation using the  $\mu\mu(\gamma)\gamma_{\text{ISR}}$  sample. The effect of the pion secondary interactions is studied in the  $\rho$  region, both in data and MC. The overall correction to the MC efficiency is  $(1.1 \pm 0.1)\%$  at  $0.4$   $\text{GeV}/c^2$  and smaller for larger masses.

#### 5. $p\bar{p}\gamma_{\text{ISR}}$ process

Proton ID is not considered in the particle identification process, since the process  $p\bar{p}\gamma_{\text{ISR}}$  contributes at a very small level. With the chosen ID classes protons are classified as pions, and antiprotons sometimes as electrons. The cross section for the  $p\bar{p}\gamma_{\text{ISR}}$  process has been measured by *BABAR* [22] and the results are used to reweight the MC prediction. The overall contamination is taken from the reweighted simulation and subtracted statistically. It amounts to less than 0.5% in the  $\rho$  central region (Table III) and exceeds the percent level at large masses only ( $m_{\pi\pi} > 1.1$   $\text{GeV}/c^2$ , Table IV).

#### 6. Multihadrons from the $q\bar{q}$ process

Hadronic processes, either direct or ISR-produced, introduce a background in the pion sample that is considerably reduced by the requirement of only two good tracks and the  $\chi^2$  selection of the kinematic fits. This contribution is estimated using simulated samples of the  $e^+e^- \rightarrow q\bar{q}$  process. However, the JETSET prediction for  $q\bar{q}$  fragmentation into low-multiplicity final states is not necessarily reliable, so the MC rate is normalized using data.

In backgrounds from the  $q\bar{q}$  process, the ISR photon candidate actually originates from the decay of an energetic  $\pi^0$ . Such a signature is searched for, both in data and in MC, by pairing the ISR photon candidate with all detected additional photons and the MC normalization is obtained from the observed  $\pi^0$  rates. The pair with  $\gamma\gamma$  mass closest to the nominal  $\pi^0$  mass is retained. Fits to  $\gamma\gamma$  mass distributions are performed in data and MC assuming a Gaussian shape for the  $\pi^0$  signal and taking into account “background” from  $\pi\pi(\gamma)\gamma_{\text{ISR}}$  events and contributions from other processes, like  $e^+e^- \rightarrow \tau\tau(\gamma)$  events, both taken from the simulation.

The  $\pi^0$  fits are carried out in wide  $\pi\pi$  mass bins ( $0.5$   $\text{GeV}/c^2$ ) between threshold and  $3$   $\text{GeV}/c^2$ , covering the practical range for the analysis. Fits are also performed in background enriched regions to check the sensitivity to the final-state multiplicity. An example of fits is shown in Fig. 21. JETSET is found to overestimate the

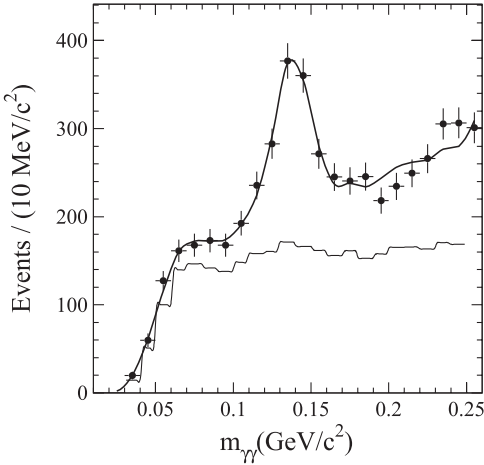


FIG. 21. The  $\gamma_{\text{ISR}}\gamma$  mass distribution for data events in a background enriched region. The  $\pi^0$  signal is fitted with a Gaussian while additional contributions are represented by a linear term. The histogram is the  $\pi\pi(\gamma)\gamma_{\text{ISR}}$  MC distribution. Contribution from  $\tau\tau$  events has been subtracted.

background contributions by a factor of 1.3, almost independent of the  $\pi\pi$  mass and whether it is determined in the signal or background enriched regions.

We check that the  $\pi^0$  finding efficiency does not depend on the final state produced by fragmentation in JETSET. The results are consistent within 5% for  $\pi^+\pi^-\pi^0$ ,  $\pi^+\pi^-2\pi^0$ , and the full  $q\bar{q}$  contribution. The final state with lowest multiplicity,  $\pi^+\pi^-\pi^0$ , which is topologically and kinematically identical to the signal, is further controlled on data. As the  $\pi\pi$  mass distribution for these events in JETSET peaks between 1 and 2  $\text{GeV}/c^2$ , well above the  $\rho$  peak, we search for a  $\pi^0$  signal in that mass range where the  $e^+e^- \rightarrow \pi\pi(\gamma)\gamma_{\text{ISR}}$  contribution is small. The weak signal observed in data is consistent with the negligible JETSET expectation within a 50% uncertainty.

After renormalization, the  $q\bar{q}$  background fraction is below 1.8% in the loose  $\chi^2$  region (Table III) and much smaller when the tight  $\chi^2$  criterion is applied, except above 1.3  $\text{GeV}/c^2$  where it reaches a few percent (Table IV).

The MC statistical errors are included in the subtracted  $q\bar{q}$  background spectra, while the uncertainty in the normalization (from  $\pi^0$  fits), typically 10%, is taken as a systematic error.

### 7. Multihadronic ISR processes

The background is estimated using simulated processes  $e^+e^- \rightarrow X\gamma_{\text{ISR}}$  where  $X$  stands for the final states:  $\pi^+\pi^-\pi^0$ ,  $\pi^+\pi^-2\pi^0$ ,  $2\pi^+2\pi^-$ ,  $2\pi^+2\pi^-\pi^0$ ,  $\eta\pi^+\pi^-$ , and  $K_S K_L$ . The dominant contributions are from  $e^+e^- \rightarrow \pi^+\pi^-\pi^0\gamma$  and  $e^+e^- \rightarrow \pi^+\pi^-2\pi^0\gamma$ . They sum to about 10% at the lower edge of the  $\rho$  peak (Table III) but are strongly reduced by the tight  $\chi^2$  criterion.

An approach similar to  $q\bar{q}$  comparing data and MC is followed for the  $\pi^+\pi^-\pi^0$  ISR normalization. This process is dominated by the production of the  $\omega$  and  $\phi$  narrow resonances, which are used as calibration signals. A kinematic fit to the  $\pi^+\pi^-3\gamma$  final state is performed using a  $\pi^0$  constraint, and the  $\pi^+\pi^-\pi^0$  mass distribution is fitted. The ratio of the contributions in data and MC is found to be  $0.99 \pm 0.04$ . The error on the normalization factor is taken as a systematic uncertainty.

The remaining ISR processes are higher-multiplicity  $\pi^0$  hadronic states such as  $2\pi 3\pi^0\gamma$ . These cross sections have not yet been measured by BABAR but we estimate that the contributions of these channels to the total background do not exceed the  $10^{-3}$  level. It is estimated from MC alone, assuming a normalization uncertainty of 10%.

### 8. Background from other processes

The  $e^+e^- \rightarrow \tau^+\tau^-(\gamma)$  process contributes significantly only at  $\pi\pi$  masses higher than the range of interest for this analysis. Although at a very small level, this background is subtracted using simulation. Two-photon processes with hard radiation such as  $e^+e^- \rightarrow (e^+e^-)\pi^+\pi^-\gamma$  and the similar reaction with muons have been specifically looked for in kinematic regions where they are expected to contribute, but without finding a significant effect.

A summary of backgrounds and related errors are given in Tables III and IV.

### 9. Overall test of the multihadronic background

The multihadron background fraction estimated above reaches sizeable values near the boundaries of the central  $\rho$  region, but with a quite small uncertainty,  $4.8 \times 10^{-3}$  at 0.5  $\text{GeV}/c^2$  and  $3.0 \times 10^{-3}$  at 1  $\text{GeV}/c^2$ , the value at the  $\rho$  peak being negligible. In the  $\rho$  tails, the estimated

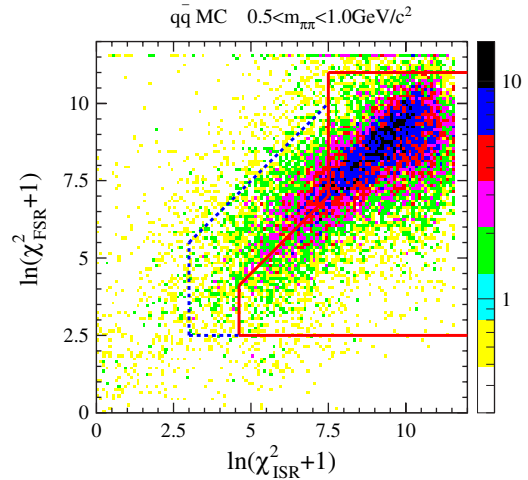


FIG. 22 (color online). 2D- $\chi^2$  distribution of  $q\bar{q}$  MC events normalized to the data luminosity for  $0.5 < m_{\pi\pi} < 1 \text{ GeV}/c^2$ . The solid broken line indicates the loose  $\chi^2$  criterion, while the dashed line defines a “sleeve” in the signal region where most of the background is concentrated.

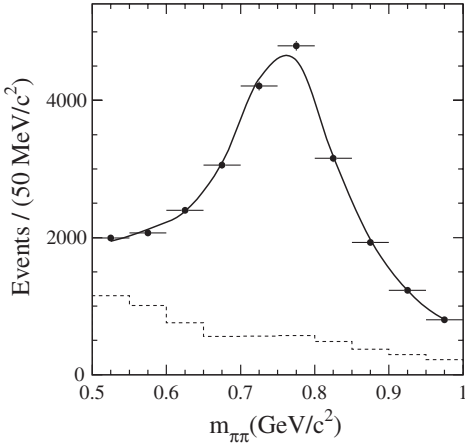


FIG. 23. The  $m_{\pi\pi}$  distribution in the background-rich “sleeve” region. The solid line represents a fit to the data with  $\pi\pi$  signal and multihadron background components, with their shapes both taken from simulation.

systematic errors due to multihadron backgrounds, which are strongly reduced by the tight  $\chi^2$  criterion, do not exceed a few permil.

We assess both the rate and the mass distribution of the multihadron background in data, in the 2D- $\chi^2$  region where it is the largest, i.e., in the “sleeve” outlined in Fig. 22. We fit the  $\pi\pi$  mass distribution in this region (Fig. 23) to background and signal components, with shapes taken from MC. The ratio of the fitted background to the one estimated in the above sections is found to be  $0.968 \pm 0.037$ , consistent with unity. This is translated into an uncertainty of  $4.5 \times 10^{-3}$  at  $0.5 \text{ GeV}/c^2$  and  $1.5 \times 10^{-3}$  at  $1 \text{ GeV}/c^2$  on the background fraction in the full  $\pi\pi$  sample. These values are below the quoted uncertainties, which validates the multihadron background estimate and confirms that the mass distribution of the background from the simulation is appropriate.

## VII. MASS SPECTRA DETERMINATION

The spectra of  $\mu\mu(\gamma)\gamma_{\text{ISR}}$  and  $\pi\pi(\gamma)\gamma_{\text{ISR}}$  events after event selection are obtained as functions of the two-track mass  $m_{\mu\mu}$  ( $m_{\pi\pi}$ ) given by the best  $\chi^2_{\mu\mu}$  ( $\chi^2_{\pi\pi}$ ) fit. These spectra are background-subtracted, and mass-dependent corrections for data/MC efficiency differences are applied as described above. To account for FSR effects and resolution smearing due to the detector response, unfolding is required to obtain the  $dN/d\sqrt{s'}$  spectra as functions of the final-state mass including FSR, which are used to measure the cross sections through Eq. (1).

### A. Unfolding of the mass spectra

#### 1. The unfolding method

The unfolding technique used in the present analysis is a simplified version of a method developed for more complex unfolding problems [23]. The folding probability

$P_{ij}$  of an event produced in a true ( $\sqrt{s'}$ ) bin  $j$  to be reconstructed in a ( $m_{xx}$ ) bin  $i$  is computed directly in simulation from the transfer matrix  $A_{ij}$  (the number of events produced in a true bin  $j$  that are reconstructed in bin  $i$ ).<sup>5</sup> Conversely, the matrix of unfolding probabilities  $P'_{ij}$  indicates the probability for an event reconstructed in a bin  $i$  to originate from the true bin  $j$ , and is also computed from the transfer matrix.  $A_{ij}$  and  $P'_{ij}$  depend on the assumed true spectrum while  $P_{ij}$ , which describes detector and FSR effects, does not. The method used to unfold the  $m_{xx}$  spectra is based on the idea that if the MC describes well enough the true spectrum in data and if the folding probabilities are well simulated, the matrix of unfolding probabilities determined in simulation can be applied to data.

If the first condition is not fulfilled, that is if the data spectrum after unfolding differs significantly from the true MC spectrum, several steps are considered where the transfer matrix is improved by reweighting the true MC, keeping the folding probabilities unchanged. Differences between data and folded (“reconstructed”) MC spectra are ascribed to differences in the unfolded (“true”) spectra. At each step of the iterative reweighting process, the data-MC differences of reconstructed spectra are unfolded and added to the true MC spectrum. Such iterative procedures can result in a significant bias to the final results if statistical fluctuations are misinterpreted as true differences between data and MC distributions. The stability of the method is provided in this analysis by the use of a regularization function to avoid unfolding large fluctuations in the data, due, for example, to a large background subtraction. Details on the method are given in Ref. [23].

#### 2. Procedure

Unfolding is applied to the reconstructed  $m_{xx}$  spectrum, after background subtraction and data/MC corrections for efficiencies, obtained as described in the previous sections. The unfolding procedure handles detector resolution and distortion effects, and corrects for FSR. Thus the process delivers the “true” distribution of events in the detector acceptance as a function of  $\sqrt{s'}$ , and a covariance matrix containing the statistical uncertainties and their bin-to-bin correlations. The covariance matrix is obtained from pseudoexperiments (toys), where both the spectrum and the transfer matrix are statistically fluctuated.

For the  $\pi\pi(\gamma)\gamma_{\text{ISR}}$  analysis, the same energy range 0–3 GeV is chosen for data and the MC transfer matrix. The spectra obtained under the central  $\rho$  region conditions (loose  $\chi^2$  criterion) and under the  $\rho$  tails conditions (tight  $\chi^2$  criterion) are unfolded separately over the full mass

<sup>5</sup>The matrix of folding probabilities is related to the transfer matrix  $A_{ij}$  by  $P_{ij} = A_{ij}/\sum_{k=1}^N A_{kj}$  while the matrix of unfolding probabilities is  $P'_{ij} = A_{ij}/\sum_{k=1}^N A_{ik}$ , where  $A_{ij}$  is the number of events produced in a true bin  $j$  that are reconstructed in bin  $i$ .

range. The unfolded spectra are combined afterwards, each being used in its respective mass region. Different bin sizes are used: 10 MeV/c<sup>2</sup> for the tails and 2 MeV/c<sup>2</sup> for the central part.

Since the loose condition retains events in the intermediate 2D- $\chi^2$  region, resolutions in data and simulation are compared in specific ranges across this region. It is noteworthy that, although the large-angle additional ISR events, absent in MC, populate the intermediate region, they do not contribute to resolution tails in data as the mass in that case is given by the (good) FSR fit. Mass spectra shapes are found to be well simulated, but the rate of events in the degraded mass resolution regions is underestimated by MC. A reweighting of the MC sample in the corresponding  $\chi^2$  regions is applied, thus modifying the MC transfer matrix. The relative distortion of the mass spectrum due to reweighting is less than 1% (see Fig. 41), hence the systematic uncertainty from the imperfect knowledge of the transfer matrix is estimated to be a fraction of 10<sup>-3</sup>.

The unfolding of the monotonic featureless mass distribution in the  $\mu\mu(\gamma)\gamma_{\text{ISR}}$  sample is much less sensitive to resolution effects and the transfer of events involves mostly FSR. Here a larger mass range (0–6 GeV/c<sup>2</sup>) is considered in 50 MeV/c<sup>2</sup> intervals (120 × 120 matrix), although only the first half is needed for luminosity purposes.

The initial mass-transfer matrices for  $\mu\mu(\gamma)\gamma_{\text{ISR}}$  events, and  $\pi\pi(\gamma)\gamma_{\text{ISR}}$  under the loose and tight conditions, are shown in Fig. 24. The large diagonal component corresponds to a mass resolution<sup>6</sup> of 3.2 MeV/c<sup>2</sup> at  $m_{\pi\pi} = 0.78$  GeV/c<sup>2</sup> (loose  $\chi^2$  criterion), and 4.6 MeV/c<sup>2</sup> at  $m_{\pi\pi} = 1.5$  GeV/c<sup>2</sup> (tight  $\chi^2$  criterion).

The most significant difference between data and reconstructed MC in relative terms occurs in the region 1.7–2 GeV/c<sup>2</sup>, where the pion form factor is not well simulated. Smaller differences, not exceeding the statistical errors for 2-MeV bins, are observed in the  $\rho$  line shape, in the tails and in the peak region with the  $\rho - \omega$  interference [Fig. 25 (top)]. These differences are assigned to the generated mass distribution in the MC, as resolution effects between data and MC are studied separately: the resolution broadening in the intermediate  $\chi^2$  region was discussed above and the resolution for the tight  $\chi^2$  condition is presented in Sec. VII C. The differences are corrected for in the iterative way described above, but it is observed that already after the first step of the reweighting procedure, they are reduced to a negligible level. The residual systematic differences have indeed very little effect on the result of the unfolding. The first unfolding result is very close to the initial data (well within the statistical error), except in the  $\rho - \omega$  interference region, as expected since the mass resolution is not small compared to the  $\omega$  width (8.5 MeV).

<sup>6</sup>For illustration here we use an effective mass resolution obtained by taking the weighted-average of the standard deviations from a two-Gaussian fit of the resolution function in simulation.

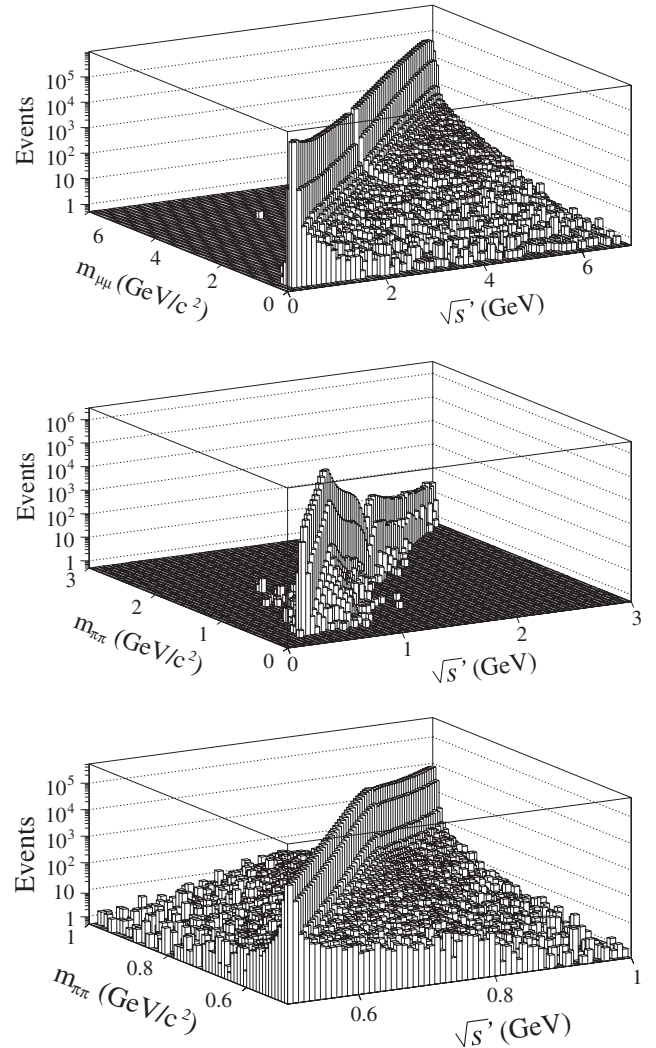


FIG. 24. The initial mass-transfer matrix  $A_{ij}$  from the simulation giving the number of events generated with a (true) mass  $\sqrt{s'}$  in a bin  $j$  and reconstructed with a (measured) mass  $m_{xx}$  in a bin  $i$ :  $\mu\mu(\gamma)\gamma_{\text{ISR}}$  (top),  $\pi\pi(\gamma)\gamma_{\text{ISR}}$  with tight  $\chi^2$  criterion (middle) and with loose  $\chi^2$  criterion (bottom). For the latter case only the relevant range 0.5–1.0 GeV/c<sup>2</sup> is shown. The  $\sqrt{s'}$  dependence comes from QED and a model of the pion form factor used in the AfkQed generator, respectively.

Adding one iteration in the unfolding does not result in further improvement, as shown in Fig. 25 (bottom).

### 3. Tests of the unfolding method

Tests of the unfolding procedure are performed, in the  $\mu\mu$  and  $\pi\pi$  channels, investigating potential systematic biases introduced by the method. The test uses toy distributions of true spectra and their corresponding reconstructed distributions obtained by folding using the nominal transfer matrix  $A$ . The reconstructed toy spectrum is then unfolded with a transfer matrix ( $\tilde{A}$ ) obtained after statistically fluctuating  $A$ . Finally the unfolded result is compared to the true toy spectrum.

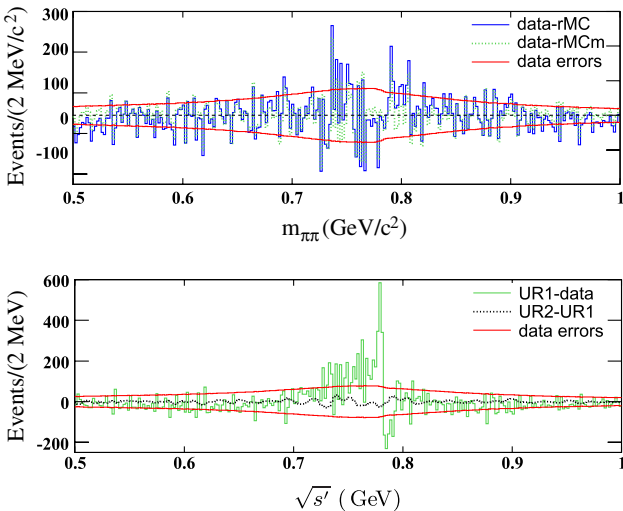


FIG. 25 (color online). (top): The difference between the  $\pi^+\pi^-$  mass distributions of data and reconstructed MC before unfolding (data – rMC) and after one iteration (data – rMCm), for the loose  $\chi^2$  selection used in the central  $\rho$  region. The data statistical errors ( $\pm 1\sigma$ ) are shown for comparison. The correction to the initial MC distribution is small, but significant in the peak and tail regions. (bottom): The difference between the result of the first unfolding (UR1) and the initial data for the same loose  $\chi^2$  criterion. It exceeds the data statistical error (band) only in the  $\rho - \omega$  interference region. No significant improvement is observed between the first (UR1) and second (UR2) unfolding results.

The true toy distribution is constructed from the true MC with a bias added. In order to build a test as close as possible to the real situation, the bias is taken as the difference between data and the normalized initial reconstructed MC. Two variations of the test are considered, where the reconstructed spectrum is additionally fluctuated statistically or not. The first situation is closer to the real unfolding operation and could reveal spurious effects due to the limited statistics in the data (and MC). The second test allows one to search for potential systematic effects of the method itself.

It is found that the systematic bias on the  $\sqrt{s'}$  spectrum from the unfolding technique is negligible in the  $\mu\mu$  channel. In the  $\pi\pi$  channel, it is below the  $10^{-3}$  level, except in the ranges  $0.5\text{--}0.6$   $\text{GeV}$  ( $1.9 \times 10^{-3}$ ) and  $0.9\text{--}1.0$   $\text{GeV}$  ( $1.2 \times 10^{-3}$ ). The latter two values are anticorrelated with the rest of the spectrum, hence the systematic uncertainty that affects the dispersion integral used in the  $a_\mu$  calculation remains smaller than  $10^{-3}$ .

#### 4. Distortion of the mass spectrum due to excess FSR

The small excess of events with additional FSR in data compared to the simulation produces a distortion of the mass spectrum not taken into account in the mass-transfer matrix. By appropriately reweighting the energy distribution of FSR photons by the energy-dependent excess

fraction one obtains the resulting systematic uncertainty on the mass distribution. The maximum deviation in the  $\rho$  region occurs at  $0.5\text{--}0.6$   $\text{GeV}/c^2$  at the  $2 \times 10^{-3}$  level, while it decreases to  $-0.8 \times 10^{-3}$  at the  $\rho$  peak and  $-0.5 \times 10^{-3}$  at  $1 \text{ GeV}/c^2$ . These values are taken as systematic uncertainties on the cross section. Because of the anticorrelation occurring below and above the peak, this effect produces a systematic uncertainty on the dispersion integral well below  $10^{-3}$ .

#### B. Mass scale calibration

The absolute  $\pi\pi$  mass scale depends on the momenta and angular measurements and the kinematic fit. Unlike at threshold where the mass scale is governed by the angular measurements, the uncertainty from the momentum scale is dominant at the  $\rho$  mass and above. Therefore systematic effects are studied using ISR-produced  $J/\psi \rightarrow \mu\mu$  events, which are treated in the same way as the dipion sample.

The  $\mu\mu$  mass distribution is fitted in the  $3.0\text{--}3.2 \text{ GeV}/c^2$  range across the  $J/\psi$  peak with a linear term for the QED background and a signal shape obtained by convoluting the sum of the natural  $J/\psi$  Breit-Wigner and the QED- $J/\psi$  interference with a Gaussian resolution shape. The free parameters are the amplitude of the signal, the  $J/\psi$  mass  $m_{J/\psi}$ , the resolution  $\sigma_m$  and the two constants of the linear background term. Three bins (1–3; 3–5; 5–8  $\text{GeV}/c$ ) are defined for the two track momenta  $p_{\min}$  and  $p_{\max}$  ( $p_{\min} < p_{\max}$ ) and fits are performed in 6 boxes in the  $(p_{\min}, p_{\max})$  plane, not distinguishing charges.

Whereas  $\sigma_m$  increases for larger momenta as expected, the fitted values for  $m_{J/\psi}$  are consistent for all boxes, showing no evidence for a momentum-dependent calibration change. Therefore the whole sample is considered, the corresponding fit being shown in Fig. 26. The small

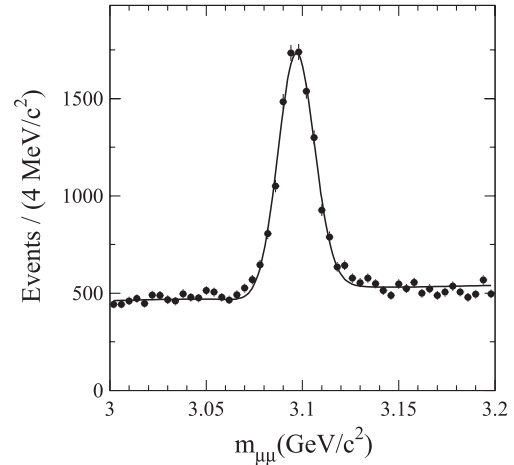


FIG. 26. Fit of the ' $\mu\mu$ ' mass distribution in the  $J/\psi$  region including the QED- $J/\psi$  interference as a momentum calibration test.

symmetric excess observed in the tails does not affect significantly the central value. The result

$$m_{J/\psi} = (3096.30 \pm 0.13) \text{ MeV}/c^2 \quad (11)$$

$$\sigma_m = (9.38 \pm 0.04) \text{ MeV}/c^2, \quad (12)$$

is compared with the world-average value [24],  $(3096.92 \pm 0.01) \text{ MeV}/c^2$ . The difference,  $(-0.62 \pm 0.13) \text{ MeV}/c^2$ , is interpreted as a momentum scale shift of  $(-2.00 \pm 0.04) \times 10^{-4}$ .

This momentum-calibration scale factor translates into a shift for the  $\rho$  mass of  $(-0.16 \pm 0.16) \text{ MeV}/c^2$  where the full correction is taken as a systematic uncertainty.

### C. Mass resolution

Since detector resolution effects are corrected for through the unfolding procedure using the mass transfer matrix from simulation, we check that simulation reproduces data in this respect. This problem is not crucial since the  $\pi^+ \pi^-$  annihilation cross section is dominated by the wide  $\rho$  resonance, except in the  $\rho - \omega$  interference region because of the small  $\omega$  width (8.5 MeV compared to the 7.6 MeV FWHM resolution).

In the  $\rho$  region the mass resolution is dominated by momentum, rather than angular measurements. Thus the  $J/\psi$  study described in Sec. VII B is again relevant. The mass resolution found in data [Eq. (12)] is slightly better than the result from the simulation of continuum  $\mu\mu(\gamma)\gamma_{\text{ISR}}$  events in the 3.0–3.2 GeV/ $c^2$  range (no  $J/\psi$  contribution is generated in AfkQed), which is found to be  $(10.0 \pm 0.1) \text{ MeV}/c^2$ .

The contribution of the decay angle measurement to the mass resolution is obtained for data and simulation from a study of the decays  $K_S^0 \rightarrow \pi^+ \pi^-$ , from a sample of ISR-produced  $\phi$  mesons decaying into  $K_S^0 K_L^0$ . In this case the angular measurement plays the dominant role compared to momentum, thus this is a situation complementary to the  $J/\psi$  one. Taking into account the smaller contribution from momentum taken from the  $J/\psi$  case, the study yields the average resolutions on the decay opening angle of  $(1.65 \pm 0.03) \text{ mrad}$  in data and  $(1.59 \pm 0.03) \text{ mrad}$  in simulation.

Combining the momentum and angular contributions one obtains the full mass resolutions of  $(3.03 \pm 0.03) \text{ MeV}/c^2$  and  $(3.20 \pm 0.03) \text{ MeV}/c^2$  for data and simulation, respectively. This resolution difference results in a bias on the measured resonance widths after unfolding of the mass spectrum, given by

$$\Delta\Gamma_\rho = (+0.016 \pm 0.004) \text{ MeV}, \quad (13)$$

$$\Delta\Gamma_\omega = (+0.27 \pm 0.07) \text{ MeV}. \quad (14)$$

As for the mass scale calibration the full biases are taken conservatively as the corresponding systematic uncertainties on the measured  $\rho$  and  $\omega$  widths.

## VIII. RESULTS ON $e^+e^- \rightarrow \mu^+\mu^-(\gamma)\gamma_{\text{ISR}}$ CROSS SECTION AND ISR LUMINOSITY

Simultaneous measurement of the  $e^+e^- \rightarrow \mu^+\mu^-(\gamma)\gamma_{\text{ISR}}$  and  $e^+e^- \rightarrow \pi^+\pi^-(\gamma)\gamma_{\text{ISR}}$  channels is a major feature of this analysis. In this section, we report the results on the absolute  $e^+e^- \rightarrow \mu^+\mu^-(\gamma)\gamma_{\text{ISR}}$  cross section measurement and the comparison to QED. The measured  $m_{\mu\mu}$  mass spectrum is corrected for all efficiencies described in the preceding sections and unfolded. Further corrections are specific to the absolute cross section measurement, which necessitate dedicated studies described in this section. We then express the results on the  $e^+e^- \rightarrow \mu^+\mu^-(\gamma)\gamma_{\text{ISR}}$  spectrum in terms of the effective ISR luminosity used in the  $e^+e^- \rightarrow \pi^+\pi^-(\gamma)$  cross section measurement.

### A. Acceptance effects specific to the $\mu\mu(\gamma)\gamma_{\text{ISR}}$ analysis

#### 1. Relevance of these studies

As stressed in the Introduction, the measurement of the  $e^+e^- \rightarrow \pi\pi(\gamma)$  cross section relies on the measurement of the  $\pi\pi/\mu\mu$  ratio  $R_{\exp}(\sqrt{s'})$ . A major advantage is that the effect from additional ISR essentially cancels in the ratio, leaving only second-order effects that are studied specifically.

However, for the QED test, we use the absolute measurement of the  $\mu\mu(\gamma)\gamma_{\text{ISR}}$  cross section in order to perform a direct comparison to QED at NLO. This is a stringent check of the full understanding of all involved systematic effects. Dedicated studies are conducted in order to assess the importance of NLO effects in the MC generator. The QED test, if successful, demonstrates that these effects are properly taken into account and that their residual impact on the  $\pi\pi/\mu\mu$  ratio measurement, in which they largely cancel, is indeed very small.

#### 2. Extra radiation in the MC generators

We use AfkQed as the  $\mu\mu(\gamma)\gamma_{\text{ISR}}$  event generator to produce a large sample (5.3 times the data) of fully-simulated events. The radiator function  $dW/d\sqrt{s'}$  and vacuum polarization correction  $\alpha(s')/\alpha(0)$  entering Eq. (6) are included in the generator. However, although AfkQed describes correctly the lowest-order process, it has some shortcomings in the generation of extra radiation: (i) additional ISR photons are generated with the structure function method in the collinear approximation, with a photon energy cutoff near 2.3 GeV in the  $e^+e^-$  c.m. (coming from the requirement  $m_{X\gamma_{\text{ISR}}} > 8 \text{ GeV}/c^2$  applied at generation), (ii) generation of additional FSR photons follows the PHOTOS algorithm.

The effects of these limitations are studied with the Phokhara 4.0 generator [17]. The advantage of Phokhara is that it uses the almost-exact QED NLO calculation (without ISR-FSR interference). However, contrary to

AfkQed, it does not include the contribution from two FSR photons nor higher-order ISR emission. Both effects are expected to be at a very small level. The contribution of two FSR photons is suppressed by the smallness of LO FSR (about 1% at 1 GeV and 15% at 3 GeV) and NLO FSR (< 1% at 1 GeV and 2.7% at 3 GeV) corrections for photon energies  $E_{\gamma \text{ add.FSR}} > 0.2$  GeV. Even at 3 GeV the expected contribution of  $4 \times 10^{-3}$  has a negligible effect on the acceptance. The contribution of higher-order ISR emission is relevant only if the third photon has a significant energy. From the acceptance change between Phokhara and AfkQed, and the fraction of NLO ISR above photon energies of 1 GeV in the  $e^+e^-$  c.m., one estimates a maximum acceptance bias of  $2 \times 10^{-3}$  at threshold and  $10^{-3}$  at 1 GeV.

### 3. Fast simulation studies with Phokhara and AfkQed

Since any number of additional photons are accepted at event selection, an imperfect simulation of NLO ISR does not affect the event topology selection but alters the event acceptance through kinematic effects.

The main criteria affecting the geometrical acceptance are: both muon tracks in the polar angle range  $0.4 < \theta_\mu < 2.45$  rad, with momenta larger than  $1 \text{ GeV}/c$ ; the most energetic photon in the c.m. (ISR candidate) with  $E_\gamma^* > 3 \text{ GeV}$  and in the polar angle range  $0.35 < \theta_\gamma < 2.4$  rad. The full acceptance involves all the event selection criteria.

As calculated using the AfkQed generator and the full simulation, the acceptance needs to be corrected for the effects resulting from the imperfect description of NLO ISR. For this correction Phokhara and AfkQed are compared at the generator level. Since the effect of the NLO differences is to give different longitudinal boosts to the events, one expects deviations in the geometrical and momentum acceptance. This justifies the use of the generators at 4-vector level. To improve on this, track and photon parameters are smeared using resolution functions obtained from data. The acceptance is defined at this level by the polar angle ranges for the ISR photon and the two muons, and the  $p > 1 \text{ GeV}/c$  requirement on the muons.

We test the sensitivity of the results to using only fast simulation. Smearing generates a relative shift of  $1.0 \times 10^{-3}$  for the acceptance correction. So any inadequacy of the resolution functions is expected to be at a lower level. Some effects are not included in the fast simulation while they enter the full MC. The main components of the overall efficiency for the full simulation are shown in Fig. 27. While the loss of acceptance is estimated to be 92% near the  $\rho$  mass, the fast simulation accounts for 78% only. The major contribution to the difference between full and fast simulation comes from the DIRC crack removal and the IFR active area (cracks and bad areas). These azimuthal effects are essentially insensitive to the longitudinal boosts from additional ISR photons. Fast simulation is consequently adequate to describe the event

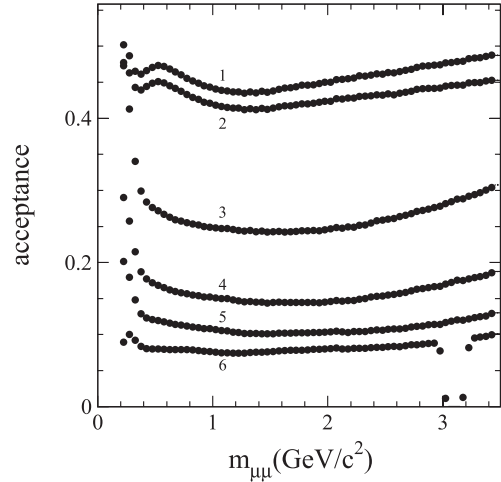


FIG. 27. Breakdown of the full simulation acceptance with respect to the generated events in the ISR photon angular range in the  $e^+e^-$  center of mass  $20^\circ$ – $160^\circ$  for  $\mu\mu(\gamma)\gamma_{\text{ISR}}$  events. The numbers refer to the sequential application of the selection requirements: (1) trigger + acceptance selection for reconstructed ISR photon and tracks; (2) preselection of ISR events +  $E_\gamma^* > 3 \text{ GeV}$ ; (3)  $p > 1 \text{ GeV}/c$  for both tracks; (4) tracks in IFR active area; (5) tracks in DIRC active area; (6) ‘ $\mu\mu$ -ID +  $\chi^2$  selection +  $J/\psi$  rejection + minor selections.

acceptance changes generated by the additional ISR photon kinematics.

### 4. Effect of collinear additional ISR in AfkQed

The angular distribution of hard additional ISR photons can produce a significant transverse momentum that affects the event acceptance and preselection efficiency. The change of acceptance for collinear and non-collinear additional ISR is investigated with Phokhara as it provides an MC sample with additional ISR following the QED angular distribution. A significant decrease of the acceptance is observed as a function of the polar angle of the additional hard ( $>0.2$  GeV) ISR photon. The difference between Phokhara and AfkQed is aggravated by the  $m_{X\gamma_{\text{ISR}}} > 8 \text{ GeV}/c^2$  requirement used at generation in AfkQed, which suppresses hard additional ISR. Both of these effects are kinematic in nature, and are well studied at the 4-vector level.

The observed differences between data and AfkQed for the angular and energy distributions for NLO ISR (Sec. VA 2) are overcome in Phokhara, which provides a much better description of the data. The geometrical acceptances computed with the smeared 4-vectors in Phokhara and AfkQed differ by about 2% in most of the mass range, Phokhara leading understandably to a lower acceptance (Fig. 28). The global efficiency  $\epsilon_{\mu\mu(\gamma)\gamma_{\text{ISR}}}$  obtained with AfkQed is corrected by this factor when computing the  $\mu\mu(\gamma)\gamma_{\text{ISR}}$  cross section.

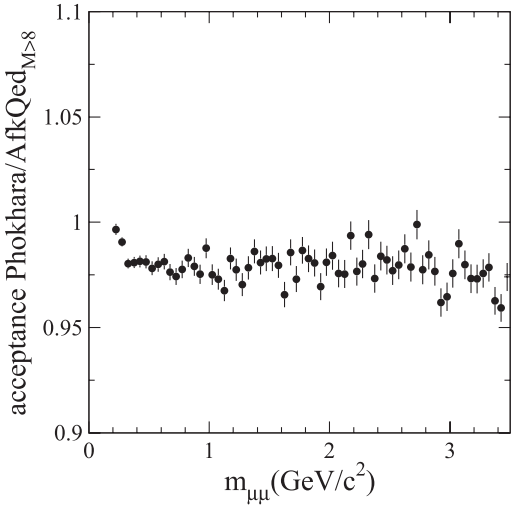


FIG. 28. The ratio of the  $\mu\mu(\gamma)\gamma_{\text{ISR}}$  acceptances determined in Phokhara and AfkQed at the generator level with fast simulation.

### B. ISR photon efficiency correction

A coarse  $\gamma_{\text{ISR}}$  detection efficiency map in the  $(E_{\gamma}^*, \theta_{\gamma})$  plane is derived from  $\mu^+\mu^-\gamma_{\text{ISR}}$  events selected on the basis of the muons only in data and full MC simulation. The data/MC correction for the ISR photon efficiency is obtained as a function of  $m_{\mu\mu}$  by sampling the efficiency maps using the simulated sample. The efficiency is found to be lower in data by  $(1.5 \pm 0.1)\%$  below  $2 \text{ GeV}/c^2$ , with a difference slightly smaller above. A systematic uncertainty of  $3 \times 10^{-3}$  is assigned to cover the effects originating from the limited map granularity.

### C. Distributions of kinematic variables

The comparison of distributions of relevant kinematic variables (polar angle  $\theta_{\gamma}$  of the ISR photon, angular and momentum distributions of the muons) observed in data and simulation is an important cross-check of the analysis, as the true distributions are predicted by QED. Not all detailed corrections that are applied to the full simulation as a function of the  $\mu\mu$  mass are available for these variables, and we only consider corrections from PID for this test. Knowing some deficiencies of AfkQed for additional ISR, the comparison is made for events without excessive extra radiation, requiring the  $\chi^2_{\mu\mu}$  of the 1C fit that uses only the two tracks to be less than 15.

Figures 29 and 30 show the distributions of  $\theta_{\gamma}$  and  $p_{\mu}$  in three mass intervals. In each case, MC is normalized to data as we are interested in testing the shapes. The agreement between data and the simulation is good, except for the ISR photon distribution at small angles where the data lies below the simulation. This effect, which cancels in the  $\pi\pi/\mu\mu$  ratio, is imputed to a data/MC difference for the photon efficiency at small angles.

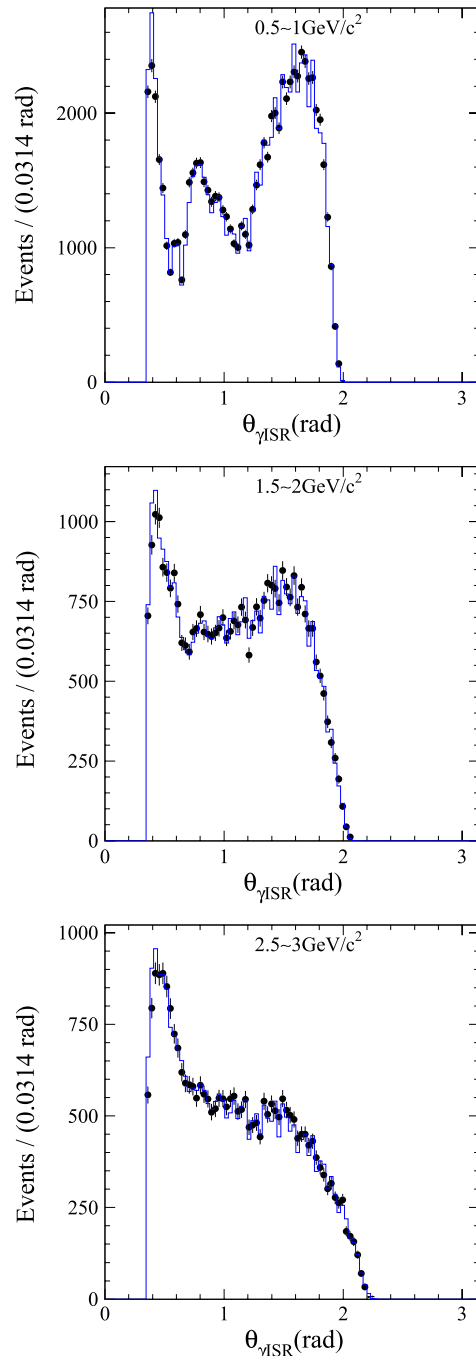


FIG. 29 (color online). The comparison between the distributions of data (points with errors) and simulation corrected for data/MC differences in PID (blue histogram), for  $\theta_{\gamma}$  in radians in the  $m_{\mu\mu}$  intervals  $0.5\text{--}1 \text{ GeV}/c^2$  (top),  $1.5\text{--}2 \text{ GeV}/c^2$  (middle),  $2.5\text{--}3 \text{ GeV}/c^2$  (bottom).

The angular distribution ( $\theta_{\mu}^*$ ) of the muons in the  $\mu\mu$  c.m. with respect to the ISR photon direction in this frame is of particular interest since it is predicted by QED to behave as

$$\frac{dN}{d \cos \theta_{\mu}^*} \sim 1 + \cos^2 \theta_{\mu}^* + (1 - \beta^2) \sin^2 \theta_{\mu}^*. \quad (15)$$

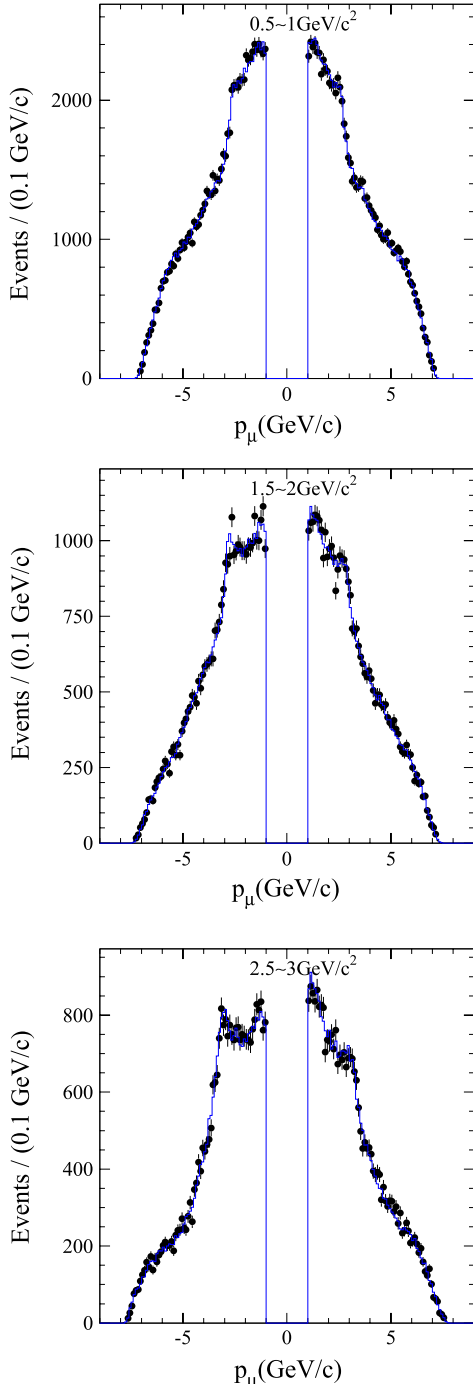


FIG. 30 (color online). The comparison between the distributions of data (points with errors) and simulation corrected for data/MC differences in PID (blue histogram), for  $\pm p_{\mu^\pm}$  in  $\text{GeV}/c$  in the  $m_{\mu\mu}$  intervals  $0.5-1 \text{ GeV}/c^2$  (top),  $1.5-2 \text{ GeV}/c^2$  (middle),  $2.5-3 \text{ GeV}/c^2$  (bottom).

for pure ISR production, with the muon velocity  $\beta = \sqrt{1-4m_\mu^2/s'}$ . So we expect the distribution to be flat at threshold and to follow a  $1 + \cos^2\theta_\mu^*$  distribution at intermediate mass. At higher masses a larger fraction of the

“ISR”-selected photon comes in fact from FSR, increasingly modifying the  $\cos\theta_\mu^*$  distribution.

The distributions of  $|\cos\theta_\mu^*|$  for different mass intervals agree well with expectation as seen in Fig. 31. Although they are strongly biased by the  $p > 1 \text{ GeV}/c$  requirement,

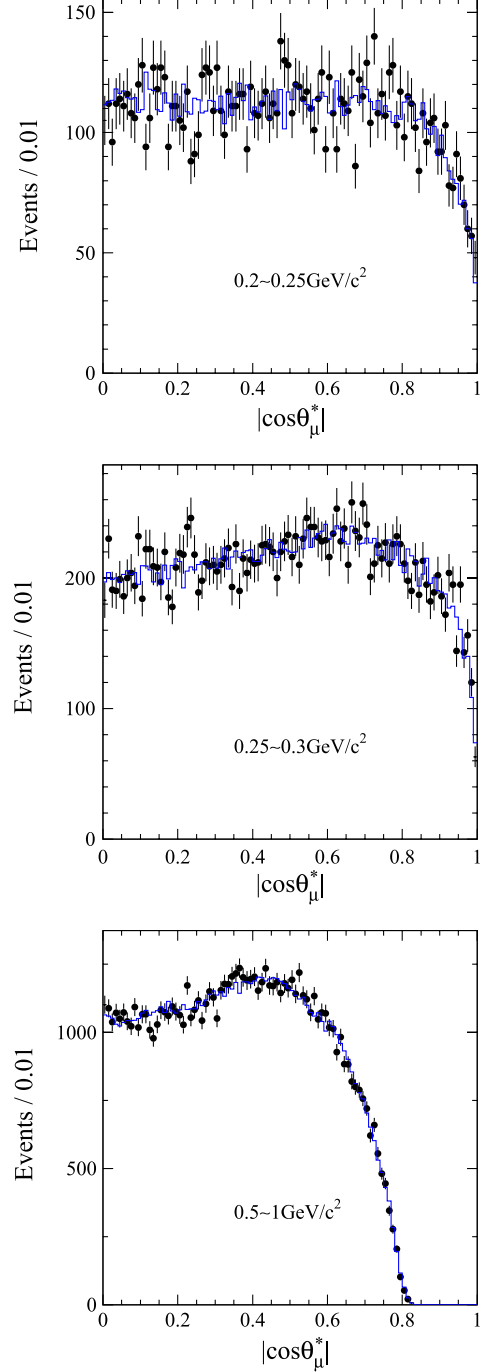


FIG. 31 (color online). The comparison between the distributions of data (points with errors) and simulation corrected for data/MC differences in PID (blue histogram), for  $|\cos\theta_\mu^*|$  in the  $m_{\mu\mu}$  intervals: (from top to bottom)  $0.20-0.25 \text{ GeV}/c^2$ ,  $0.25-0.30 \text{ GeV}/c^2$ , and  $0.5-1 \text{ GeV}/c^2$ .

which depletes the region near one, distributions in the threshold region indeed show the behavior expected from Eq. (15), in agreement with the MC.

Thus the distributions of the main kinematic variables of the selected  $\mu\mu(\gamma)\gamma_{\text{ISR}}$  sample are in good agreement with expectations from QED as implemented in the MC generator.

### D. Systematic uncertainties on the absolute $\mu\mu(\gamma)\gamma_{\text{ISR}}$ cross section

The statistical errors of the measured efficiencies are included with the main statistical uncertainty on the  $\mu\mu$  mass spectrum. However, in some cases, remaining systematic uncertainties are attached to the efficiency measurement process. Estimated systematic uncertainties on the measured cross section are summarized in Table II for the mass range from threshold to 2 GeV/ $c^2$ . Above 2 GeV/ $c^2$  the uncertainties are smaller, essentially because of the more straightforward determination of the muon-ID efficiencies. In some cases no systematic error is quoted when all uncertainties proceed from measurements and are already included in the point-to-point statistical errors.

We find that Phokhara at the fast simulation level is adequate to correct the AfkQed generator and that the systematic uncertainty on the acceptance resulting from the fast simulation is  $10^{-3}$ . The effect of the momentum calibration uncertainty is only at the  $10^{-4}$  level.

The absolute  $\mu\mu(\gamma)\gamma_{\text{ISR}}$  cross section makes use of the effective luminosity function defined by Eq. (6) that includes the *BABAR* luminosity  $L_{ee}$ . The latter is obtained for all the analyzed data using measurements of  $ee \rightarrow ee$ ,  $\mu\mu$  and  $\gamma\gamma$ , and amounts to  $230.8 \text{ fb}^{-1}$ . The corresponding systematic uncertainty is 0.94%.

TABLE II. Systematic uncertainties (in  $10^{-3}$ ) on the absolute  $\mu\mu(\gamma_{\text{FSR}})$  cross section from the determination of the various efficiencies in the  $\mu\mu$  mass range up to 2 GeV/ $c^2$ . The statistical part of the efficiency measurements is included in the total statistical error in each mass bin. For those contributions marked “–” all the relevant uncertainties come from measurements and are already counted in the statistical errors.

Sources	Systematic errors ( $10^{-3}$ )
Triggers and background filter	0.3
Tracking	1.3
Muon ID	3.3
$\pi\pi$ and $KK$ backgrounds	–
Multihadronic background	–
$\chi^2$ cut efficiency	–
Angle and momentum acceptance	1.0
ISR photon efficiency	3.4
$e^+e^-$ luminosity	9.4
NNLO corrections to $\sigma_{\text{QED}}$	2.0
Sum	10.9

The uncertainty assigned to the QED cross section comes from the neglect of the NNLO contribution. The latter is estimated from the NLO fraction as given by Phokhara, equal to  $(4.33 \pm 0.11)\%$  within the selection used in this analysis. Assuming a geometric growth of the coefficients of the expansion in  $\alpha$ , the NNLO fraction is estimated to be  $2 \times 10^{-3}$ , which is taken as the systematic uncertainty.

Summarizing, the overall systematic uncertainty on the absolute  $\mu\mu(\gamma)\gamma_{\text{ISR}}$  cross section is 1.1%, dominated by the *BABAR* luminosity error.

### E. QED test with the $\mu\mu(\gamma)\gamma_{\text{ISR}}$ events

The comparison of the  $\mu\mu(\gamma)\gamma_{\text{ISR}}$  cross section with QED is made through the ratio of the distribution in the data as a function of  $m_{\mu\mu}$  to the same distribution of the simulation. Specifically, the distribution of the data is background-subtracted, and the distribution of the AfkQed-based full simulation, normalized to the data luminosity, is corrected for all data/MC detector and reconstruction effects and for the generator NLO limitations using the Phokhara/AfkQed comparison with fast simulation. Because of the latter adjustments, discussed in detail in Sec. VIII A, the corrected ratio of  $m_{\mu\mu}$  spectra is equivalent to a direct comparison of data with the NLO QED cross section.

The QED prediction for the  $m = m_{\mu\mu}$  distribution is obtained in the following way:

$$\frac{dN_{\text{QED}}}{dm} = L_{ee} \sigma_{\text{Phokhara}}^{\text{NLO}} \left( \frac{1}{N_0} \frac{dN}{dm} \right)^{\text{AfkQed,M>8}}_{\text{fullsim}} \times \frac{\left( \frac{1}{N_0} \frac{dN}{dm} \right)^{\text{Phokhara}}_{\text{fastsim}}}{\left( \frac{1}{N_0} \frac{dN}{dm} \right)^{\text{AfkQed,M>8}}_{\text{fastsim}}} \times C_{\text{data/MC}}, \quad (16)$$

where for each case  $N_0$  is the generated number of events,  $dN/dm$  the mass spectrum of events satisfying all criteria. The ratio of spectra at the generator level with fast simulation are labeled “fastsim”, while “fullsim” denotes the spectrum of events with full detector simulation. The notation “M > 8” recalls that AfkQed was run with a requirement limiting hard additional ISR,  $m_{X\gamma_{\text{ISR}}} > 8 \text{ GeV}/c^2$ . Finally, the  $C_{\text{data/MC}}$  factor incorporates all data/MC corrections for detector efficiencies, such as trigger, tracking, muon ID,  $\chi^2$  selection, and ISR photon efficiency.

Because the PID efficiency varied with time due to the degradation of the IFR detector, the ratio data/QED is determined separately splitting the running period in two. Both distributions are flat from threshold to 3.5 GeV/ $c^2$  and consistent with unity within errors with satisfactory  $\chi^2$  values. The difference of the ratios for the two data sets is  $(6.0 \pm 4.0 \pm 3.5 \pm 4.4) \times 10^{-3}$ , where the first error is statistical, the second from noncommon systematics (uncorrelated parts of the  $\mu$ -ID systematic uncertainties),

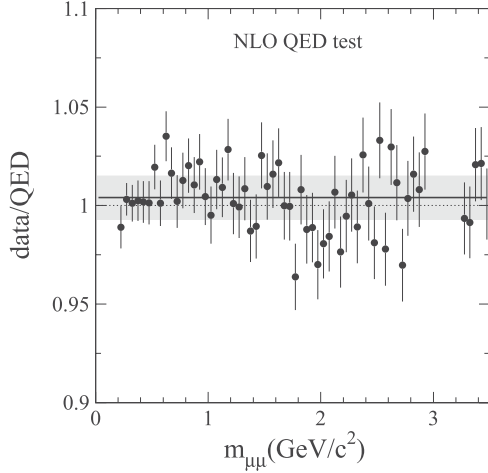


FIG. 32. The ratio of the  $\mu\mu$  mass spectrum in data over the absolute prediction from QED using the *BABAR* luminosity. The NLO QED prediction is obtained from the data-corrected (for detector simulation) and Phokhara-corrected (for NLO effects) AfkQed mass spectrum. The band is drawn around the fit of the 0.2–3.5  $\text{GeV}/c^2$  region to a free constant, with a width given by  $\pm$  the total expected systematic uncertainty.

and the third from the *BABAR* luminosity. Since the two samples correspond to different performances of the IFR detector, this test provides a confirmation that the muon-ID efficiency has been handled adequately.

The fit to the full data set is shown in Fig. 32 and yields

$$\frac{\sigma_{\mu\mu(\gamma)\gamma_{\text{ISR}}}^{\text{data}}}{\sigma_{\mu\mu(\gamma)\gamma_{\text{ISR}}}^{\text{NLO QED}}} = 1 + (4.0 \pm 1.9 \pm 5.5 \pm 9.4) \times 10^{-3}, \quad (17)$$

where the first error is statistical, the second from systematics, and the third from the *BABAR* luminosity. The value found for the ratio is consistent with unity over the full mass range explored in this analysis. We conclude that the measurement of the  $e^+e^- \rightarrow \mu^+\mu^-(\gamma)\gamma_{\text{ISR}}$  cross section using the *BABAR* luminosity agrees with NLO QED in the  $\mu\mu$  mass range from threshold to 3.5  $\text{GeV}/c^2$  within an overall accuracy of 1.1%.

## F. Determination of ISR luminosity

In this section we express the results obtained for the  $\mu\mu(\gamma)\gamma_{\text{ISR}}$  sample in terms of the effective ISR luminosity, following Eq. (1). As discussed in Sec. VIIA the  $\mu\mu(\gamma)\gamma_{\text{ISR}}$  event acceptance,  $\epsilon_{\mu\mu(\gamma)\gamma_{\text{ISR}}}$ , appearing in Eq. (1) is obtained from the large simulated sample generated with AfkQed with corrections for detector and reconstruction effects. Corrections specific to the QED test, i.e., NLO and ISR photon efficiency corrections that cancel in the  $\pi\pi/\mu\mu$  ratio, are not applied.

Several factors need to be considered in addition: (i) the LO FSR correction, (ii) unfolding of the data from  $m_{\mu\mu}$  to  $\sqrt{s'}$  to include the possible emission of an additional FSR photon, and (iii) the QED cross section

$\sigma^0(e^+e^- \rightarrow \mu^+\mu^-(\gamma_{\text{FSR}}))(s')$  at the Born level concerning ISR, but including FSR. Except for (ii), which has been discussed in Sec. VIIA, we address these points in turn before giving the final result on the ISR luminosity.

### 1. Lowest-order FSR correction

The most energetic detected photon is assumed to be emitted by the initial state. This is largely true at low mass, but there is an increasing probability at larger  $s'$  values that this photon originates from muon radiation. Thus the observed  $\mu\mu$  mass spectrum has to be corrected in order to keep only ISR production, since for all practical purposes at *BABAR* where  $\sqrt{s} \sim 10.58 \text{ GeV}$  and  $\sqrt{s'} < 5 \text{ GeV}$ , LO FSR production is negligible for hadronic processes.

Figure 33 shows the  $\delta_{\text{FSR}}^{\mu\mu}$  correction to the cross section, defined as

$$\delta_{\text{FSR}}^{\mu\mu} = \frac{|\mathcal{A}_{\text{FSR}} + \mathcal{A}_{\text{add.ISR,add.FSR}}|^2}{|\mathcal{A}_{\text{ISR}} + \mathcal{A}_{\text{add.ISR,add.FSR}}|^2}, \quad (18)$$

as a function of  $\sqrt{s'}$ , where  $\mathcal{A}_{\text{FSR}}$  ( $\mathcal{A}_{\text{ISR}}$ ) is the LO FSR (ISR) amplitude and  $\mathcal{A}_{\text{add.ISR,add.FSR}}$  is the NLO contribution.  $\delta_{\text{FSR}}^{\mu\mu}$  is obtained with AfkQed at the generator level. It would be preferable to use Phokhara instead, as we know additional ISR generation is approximate in AfkQed, but by construction the FSR or ISR origin of photons is not available in Phokhara, hence  $s'$  is not accessible on an event-by-event basis. However the difference in  $\delta_{\text{FSR}}^{\mu\mu}$  is expected to be at a negligible level, about  $10^{-4}$  and  $2 \times 10^{-3}$  at 1  $\text{GeV}$  and 3  $\text{GeV}$ , respectively.

### 2. Born QED cross section with additional FSR

The cross section for  $e^+e^- \rightarrow \mu^+\mu^-(\gamma_{\text{FSR}})$ , at the Born level for the initial state and without vacuum polarization, can be calculated exactly in QED at NLO. It has the form:

$$\sigma_{\mu\mu(\gamma)}^0(s') = \sigma_{\text{pt}}(s')(1 + \delta_{\text{add.FSR}}^{\mu\mu}), \quad (19)$$

with

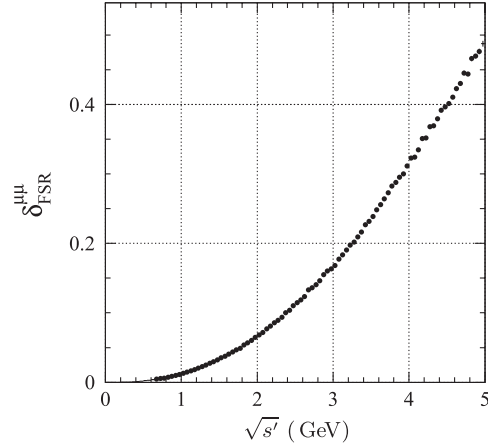


FIG. 33. The FSR correction  $\delta_{\text{FSR}}^{\mu\mu}$  obtained with AfkQed.

$$\sigma_{\text{pt}}(s') = \frac{4\pi\alpha^2(0)}{3s'} \frac{\beta(3-\beta^2)}{2} \quad (20)$$

$$\delta_{\text{add.FSR}}^{\mu\mu} = \frac{\alpha(0)}{\pi} \eta(s') \quad (21)$$

$$\eta(s') = \eta_h(s') + \eta_s(s') + \eta_v(s'), \quad (22)$$

where  $\beta$  is the muon velocity and  $\eta_{h,s,v}$  are the  $O(\alpha)$  contributions to the final state from hard and soft bremsstrahlung, and the one-loop/Born interference (“virtual” contribution), respectively.

The sum of  $\eta_v$  and  $\eta_s$  is infrared-finite, while the total sum is independent of the choice of the energy used to separate soft and hard photons (within reasonable limits). Expressions for all three components can be found in many papers, for example, in Refs. [25,26]. By virtue of the Kinoshita-Lee-Nauenberg theorem [27], the dominant logarithmic terms cancel in the sum of the (soft + virtual) and hard contributions. Although the two terms reach a level of a few percent, they have opposite signs and the sum  $\delta_{\text{add.FSR}}^{\mu\mu}$  stays in the few  $\times 10^{-3}$  range. This explains why a sizeable hard additional FSR signal is seen in data, despite the fact that the total additional FSR contribution is very small.

### 3. The effective ISR luminosity for the $\pi\pi(\gamma)\gamma_{\text{ISR}}$ analysis

For the  $\pi\pi(\gamma)\gamma_{\text{ISR}}$  analysis, the luminosity  $dL_{\text{ISR}}^{\text{eff}}$  integrates all configurations up to two ISR photons, where at least one photon has  $E_\gamma^* > 3$  GeV and is in the angular range  $(\theta_{\min}^*, \theta_{\max}^*)$  in the  $e^+e^-$  c.m. with  $\theta_{\min}^* = 180^\circ - \theta_{\max}^* = 20^\circ$ .

The full effective ISR luminosity  $dL_{\text{ISR}}^{\text{eff}}/d\sqrt{s'}$  is derived from the measured  $\mu\mu(\gamma)\gamma_{\text{ISR}}$  spectrum according to Eq. (1). The event acceptance is taken from AfkQed, with corrections for detector and reconstruction effects. Unfolding of the background-subtracted  $\mu\mu$  mass spectrum is performed as explained in Sec. VII A. The result is shown in Fig. 34. The effective luminosity derived this way implicitly includes the VP factor since the  $\mu\mu(\gamma)\gamma_{\text{ISR}}$  data include vacuum polarization effects, while the bare cross section  $\sigma_{\mu\mu(\gamma)}^0(\sqrt{s'})$  entering Eq. (1) does not.

The measured effective luminosity is compared to the standard estimate of Eq. (6) using LO QED, given by

$$\frac{dL_{\text{LO}}}{d\sqrt{s'}} = L_{ee} \frac{dW_{\text{LO}}}{d\sqrt{s'}} \left( \frac{\alpha(s')}{\alpha(0)} \right)^2, \quad (23)$$

where the LO radiator function is [10,11]

$$\frac{dW_{\text{LO}}}{d\sqrt{s'}} = \frac{\alpha(0)}{\pi x} \left[ (2 - 2x + x^2) \ln \frac{1+c}{1-c} - x^2 c \right] \frac{2\sqrt{s'}}{s},$$

with  $x = 1 - s'/s$  and  $c = \cos\theta_{\min}^*$ . We insert the VP term  $\alpha(s')/\alpha(0)$  in Eq. (23) for a convenient comparison with the effective luminosity. The computed VP factor includes

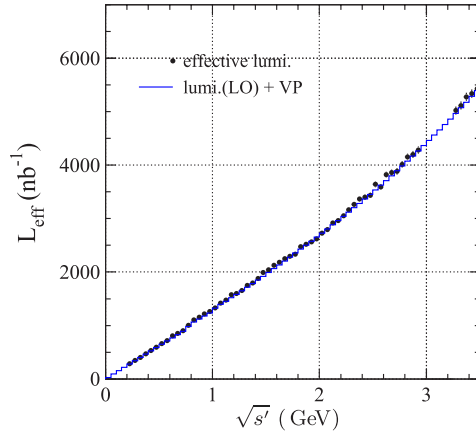


FIG. 34 (color online). The effective ISR luminosity for the  $\pi\pi$  analysis: the data points give  $L_{\text{ISR}}^{\text{eff}}$  in  $\Delta\sqrt{s'} = 50$  MeV bins. The conditions for the detected/identified ISR photon are  $E_\gamma^* > 3$  GeV and  $20^\circ < \theta_\gamma^* < 160^\circ$  in the  $e^+e^-$  c.m. frame, while one additional ISR photon is allowed without any restriction. The superimposed histogram is the lowest-order ISR prediction following Eq. (23). The  $J/\psi$  mass region is removed for the luminosity determination.

both leptonic and hadronic contributions. The hadronic contribution is taken from the parametrization used in AfkQed and is found to agree well with an independent determination using the tools of Ref. [7].

The LO + VP prediction is superimposed on the measured effective luminosity in Fig. 34. The measured luminosity is found to be about 2% larger than the LO + VP QED result. This difference varies slowly with mass and includes systematic effects on the *BABAR* luminosity determination, the effect of the NLO contribution in data, the difference between the ISR photon efficiency in data and MC and any residual effect in the detection efficiency. The latter contribution is small, in accordance with the successful QED test performed with the  $\mu\mu(\gamma)\gamma_{\text{ISR}}$  cross section.

The effective luminosity shown in Fig. 34 is measured in 50 MeV bins. This interval size is too wide near narrow resonances ( $\omega$  and  $\phi$ ) because of the rapid variation of hadronic vacuum polarization. Therefore, we compute the local variation inside each 50 MeV interval as the product of the lowest-order QED radiator function times the vacuum polarization factor. The result is normalized to the effective luminosity in the interval. In this way the detailed local features are described, while preserving the measured effective luminosity as a function of mass.

The statistical error of the  $\pi\pi$  cross section is limited in the  $\rho$  resonance region by the number of events available to determine the ISR luminosity. Bin-to-bin statistical fluctuations are reduced by a suitable averaging of the ratio of measured to LO ISR luminosities. The ratio distribution in 50 MeV bins is smoothed by averaging five consecutive bins in a sliding way. This value is chosen as a compromise between smoothing and the validity of the assumption of slow variation. This method does not improve in principle

the ISR luminosity statistical error because the reduced local error is compensated by the correlation between neighboring bins. A slight improvement in the dispersion integral is however observed due to the weighting in different mass regions.

The statistical errors on the ISR effective luminosity from the measurement of efficiencies are included in the statistical covariance matrix, while the systematic errors from the different procedures are accounted for separately. These errors are  $0.3 \times 10^{-3}$  for the trigger,  $1.3 \times 10^{-3}$  for tracking,  $2.9 \times 10^{-3}$  for  $\mu$ -ID, and  $1.0 \times 10^{-3}$  for acceptance, for a total systematic uncertainty of  $3.4 \times 10^{-3}$ . The uncertainty from the correlated loss of  $\mu$ -ID for both tracks is not included here, since it is anticorrelated with the pion rate. It is counted in the systematic errors on the  $\pi\pi$  cross section.

## IX. MEASUREMENT OF THE $e^+e^- \rightarrow \pi^+\pi^-(\gamma)$ CROSS SECTION

The  $e^+e^- \rightarrow \pi^+\pi^-(\gamma)$  bare cross section is measured from the  $\sqrt{s'}$  distribution of produced  $\pi^+\pi^-(\gamma)\gamma_{\text{ISR}}$  events divided by the effective ISR luminosity obtained from  $\mu^+\mu^-(\gamma)\gamma_{\text{ISR}}$  on the same data. The  $\sqrt{s'}$  distribution is obtained from the observed  $m_{\pi\pi}$  mass spectrum, after background subtraction, corrections for data/MC efficiency differences, unfolding, and MC acceptance corrections, as described in detail in the preceding sections. Because the cross section spans several orders of magnitude over the energy region considered, from threshold to 3 GeV, the analysis strategy depends on the mass region. Event selection and background subtraction are optimized separately for the  $\rho$  resonance central region or for the resonance tails, with corresponding efficiency corrections and unfolding matrix. To facilitate comparison with other experiments, the results are also shown in terms of the pion form factor fitted with a vector-dominance model (VDM).

### A. The central $\rho$ region ( $0.5 < m_{\pi\pi} < 1 \text{ GeV}/c^2$ )

#### 1. Strategy

The mass region between 0.5 and 1  $\text{GeV}/c^2$ , dominated by the  $\rho$  resonance, provides the dominant contribution to the vacuum-polarization dispersion integrals and their errors. The need for small systematic uncertainties, congruous with the small statistical errors, together with the low background level in that region, lead to an event selection with the largest efficiency. Therefore the loose  $\chi^2$  criterion, the same as for the  $\mu\mu(\gamma)\gamma_{\text{ISR}}$  analysis, and standard  $\pi$ -ID for both tracks are used.

#### 2. Summary of backgrounds

The backgrounds are obtained as described in Sec. VI. The dominant contribution is from multihadronic processes, mostly ISR ( $\pi^+\pi^-\pi^0\gamma$ ,  $\pi^+\pi^-2\pi^0\gamma$ ) and  $q\bar{q}$ , with a fraction amounting to  $8.4 \times 10^{-3}$  at the  $\rho$  peak. The  $p\bar{p}\gamma$  contribution is much smaller ( $< 10^{-3}$ ).

TABLE III. Estimated background fractions (in %) in the ' $\pi\pi$ ' sample for  $m_{\pi\pi} = 0.525, 0.775, 0.975 \text{ GeV}/c^2$ . The quoted errors include both statistical and systematic uncertainties.

Process	$0.525 \text{ GeV}/c^2$	$0.775 \text{ GeV}/c^2$	$0.975 \text{ GeV}/c^2$
$\mu\mu$	$3.48 \pm 0.36$	$0.37 \pm 0.23$	$2.71 \pm 0.31$
$KK$	$0.08 \pm 0.01$	$0.01 \pm 0.01$	$0.08 \pm 0.01$
$\gamma 2\pi\pi^0$	$8.04 \pm 0.41$	$0.39 \pm 0.05$	$0.88 \pm 0.19$
$q\bar{q}$	$1.11 \pm 0.17$	$0.26 \pm 0.03$	$1.81 \pm 0.19$
$\gamma 2\pi 2\pi^0$	$1.29 \pm 0.16$	$0.06 \pm 0.01$	$0.46 \pm 0.09$
$\gamma 4\pi$	$0.20 \pm 0.04$	$0.09 \pm 0.01$	$0.24 \pm 0.06$
$\gamma p\bar{p}$	$0.22 \pm 0.02$	$0.04 \pm 0.01$	$0.52 \pm 0.06$
$\gamma\eta 2\pi$	$0.02 \pm 0.01$	$0.03 \pm 0.01$	$0.09 \pm 0.01$
$\gamma K_SK_L$	$0.18 \pm 0.03$	$0.01 \pm 0.01$	$0.10 \pm 0.02$
$\gamma 4\pi 2\pi^0$	$<0.01$	$<0.01$	$<0.01$
$\tau\tau$	$0.17 \pm 0.03$	$0.04 \pm 0.01$	$0.31 \pm 0.05$
$\gamma ee$	$0.63 \pm 0.63$	$0.03 \pm 0.03$	$0.27 \pm 0.27$
Total	$15.38 \pm 0.87$	$1.31 \pm 0.24$	$7.37 \pm 0.51$

The fractions of all the considered backgrounds are given in Table III at three mass values. For convenience, we also show the level of the  $\mu\mu$  and  $KK$  background contributions in the ' $\pi\pi$ '-identified sample, although they are implicitly subtracted when solving Eqs. (8) for the produced spectrum  $N_{\pi\pi}$ .

The total background fraction as a function of  $m_{\pi\pi}$  is shown in Fig. 35. It is 1.3% at the  $\rho$  peak, but reaches  $\sim 15\%$  at  $0.5 \text{ GeV}/c^2$  and  $\sim 7\%$  at  $1 \text{ GeV}/c^2$ . These sharp increases justify the limits chosen to define the “central region”. At the worst place, near  $0.5 \text{ GeV}/c^2$ , the total uncertainty from the estimated non- $\mu\mu/KK$  background fraction is 0.8%, which is still tolerable. At the peak the uncertainty is less than 0.1%.

#### 3. Background-subtracted $m_{\pi\pi}$ mass distribution

The background-subtracted  $m_{\pi\pi}$  spectrum obtained in the  $\rho$  region before unfolding, with loose  $\chi^2$  criterion and

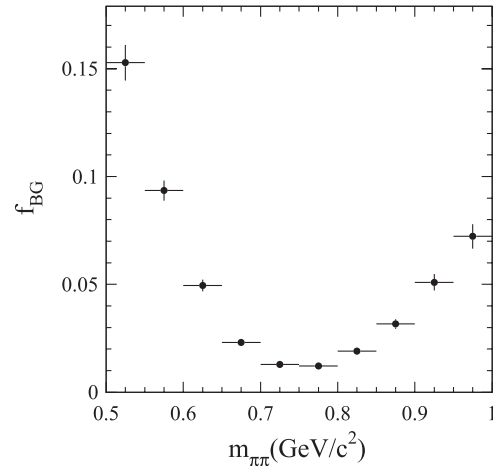


FIG. 35. The total background fraction for the  $\pi\pi(\gamma)\gamma_{\text{ISR}}$  sample in the central  $\rho$  region (loose  $\chi^2$  selection).

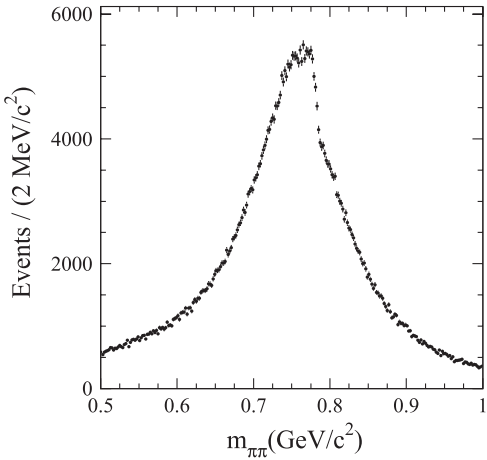


FIG. 36. The  $m_{\pi\pi}$  spectrum of  $\pi\pi(\gamma)\gamma_{\text{ISR}}$  events in the  $\rho$  region, in  $2 \text{ MeV}/c^2$  bins.

' $\pi$ '-ID for both pions, is shown in Fig. 36. Only the statistical errors in the  $2 \text{ MeV}/c^2$  mass intervals are given, amounting to 1.4% on peak and 4.4% near the boundaries. Apart from the  $\rho$  resonance shape, a clear  $\rho - \omega$  interference pattern is observed.

## B. The $\rho$ tail regions ( $m_{\pi\pi} < 0.5$ , $m_{\pi\pi} > 1 \text{ GeV}/c^2$ )

### 1. Strategy

The pion cross section decreases very rapidly away from the  $\rho$  resonance, while the backgrounds from  $\mu\mu(\gamma)\gamma_{\text{ISR}}$ ,  $KK(\gamma)\gamma_{\text{ISR}}$ ,  $p\bar{p}\gamma_{\text{ISR}}$ , and multihadron events show a smooth variation with the  $\pi\pi$  mass. To keep the background levels under control in the  $\rho$  tail regions, the selection of  $\pi\pi(\gamma)\gamma_{\text{ISR}}$  events is tightened with respect to the criteria used in the  $\rho$  region. Two handles are simultaneously used: (i) the tight  $\chi^2$  criterion  $\ln(\chi^2_{\text{ISR}} + 1) < 3$  is chosen to reduce multihadronic backgrounds, and (ii) the pion-ID is strengthened to improve muon (and also electron) rejection. In addition, the  $V_{xy}$  requirement described in Sec. VI B 4 is applied to remove backgrounds from photon conversions and bremsstrahlung in the beam pipe.

### 2. Summary of backgrounds

For two-body ISR and  $ee$  backgrounds, the tighter  $\chi^2$  criterion is not useful, so the harder  $\pi$  identification, ' $\pi_h$ ' (Sec. IV D 2) is required for at least one of the two ' $\pi$ '-identified tracks, giving a further rejection of  $\mu$  and  $e$ . The downside is that, because the ' $\pi_h$ ' identification breaks the completeness of PID classes, the  $\mu\mu$  and  $KK$  backgrounds cannot be subtracted anymore from the ' $\pi\pi_h$ ' sample by solving the Eqs. (8) system.

The  $\mu\mu(\gamma)\gamma_{\text{ISR}}$  background is estimated according to Sec. VI B 1. With the ' $\pi\pi_h$ ' selection, it is reduced by a factor  $\sim 7$  with respect to the background remaining after the standard pion-ID. However the corresponding factor

for the background fraction in the final pion sample is smaller because the ' $\pi\pi_h$ ' efficiency also reduces the signal (Sec. IV D 7).

Neither the tight  $\chi^2$  criterion nor the ' $\pi\pi_h$ ' ID brings significant reduction of the  $KK(\gamma)\gamma_{\text{ISR}}$  background compared to the selection used in the  $\rho$  peak region. Its small contribution is estimated from data by using the procedure described in Sec. VI B 2 and subtracted.

The backgrounds from  $q\bar{q}$  and multihadronic ISR events are estimated as discussed in Secs. VI B 6 and VI B 7, respectively. They are much reduced compared to the central  $\rho$  region because of the tight  $\chi^2$  condition.

The different fractions of background in the region of the  $\rho$  tails, with ' $\pi\pi_h$ ' ID and  $\ln(\chi^2_{\text{ISR}} + 1) < 3$ , are given in Fig. 37. Fractions at specified masses are listed in Table IV. The total background contribution is obtained by summing all the individual contributions obtained above.

## 3. Background-subtracted $m_{\pi\pi}$ mass distribution

The background-subtracted  $m_{\pi\pi}$  distribution of  $\pi\pi(\gamma)\gamma_{\text{ISR}}$  events before unfolding, using ' $\pi\pi_h$ ' identification and  $\ln(\chi^2_{\text{FSR}} + 1) < 3$  is plotted from threshold to  $3 \text{ GeV}/c^2$  in  $50 \text{ MeV}/c^2$  mass intervals in Fig. 38. A dynamic range of  $10^3$ – $10^4$  is observed between the  $\rho$  peak and either the first bin above threshold or at  $3 \text{ GeV}/c^2$ . The dip structure at  $1.6 \text{ GeV}/c^2$  seen by the DM2 experiment [28] is confirmed with high statistics and a new structure shows up near  $2.2 \text{ GeV}/c^2$ .

## C. Angular distribution in the $\pi\pi$ center of mass

The distributions of kinematic variables such as the ISR photon polar angle and the pion momenta and angles depend on the hadronic structure we seek to measure. Thus the detailed comparisons between data and MC distributions expected from theory, which are performed in the  $\mu\mu(\gamma)\gamma_{\text{ISR}}$  channel with QED (Sec. VIII C), are meaningless in the pion channel. However, one distribution, namely, the pion angular distribution in the  $\pi\pi$  center of mass, with respect to the ISR photon direction in that frame, is model independent. The  $\cos\theta_\pi^*$  distribution is consistent with  $\sin^2\theta_\pi^*$  as expected in the  $e^+e^- \rightarrow \pi^+\pi^-$  process, but it is strongly distorted at  $|\cos\theta_\pi^*|$  values near one by the  $p > 1 \text{ GeV}/c$  requirement on the tracks.

The  $|\cos\theta_\pi^*|$  distributions for background-subtracted data and MC are compared in Fig. 39 for the  $0.5$ – $1 \text{ GeV}/c^2$  mass range: they agree with each other within the statistical errors, as expected for a pure pion sample.

## D. Acceptance and corrections

The overall efficiency  $\varepsilon_{\pi\pi(\gamma)\gamma_{\text{ISR}}}$  entering Eq. (1) for the pion channel is calculated using the AfkQed generator and full simulation in the same way as for the muon channel. It is corrected for differences in efficiencies between data and MC, which are introduced as mass-dependent corrections applied to the event spectrum [Eq. (7)].

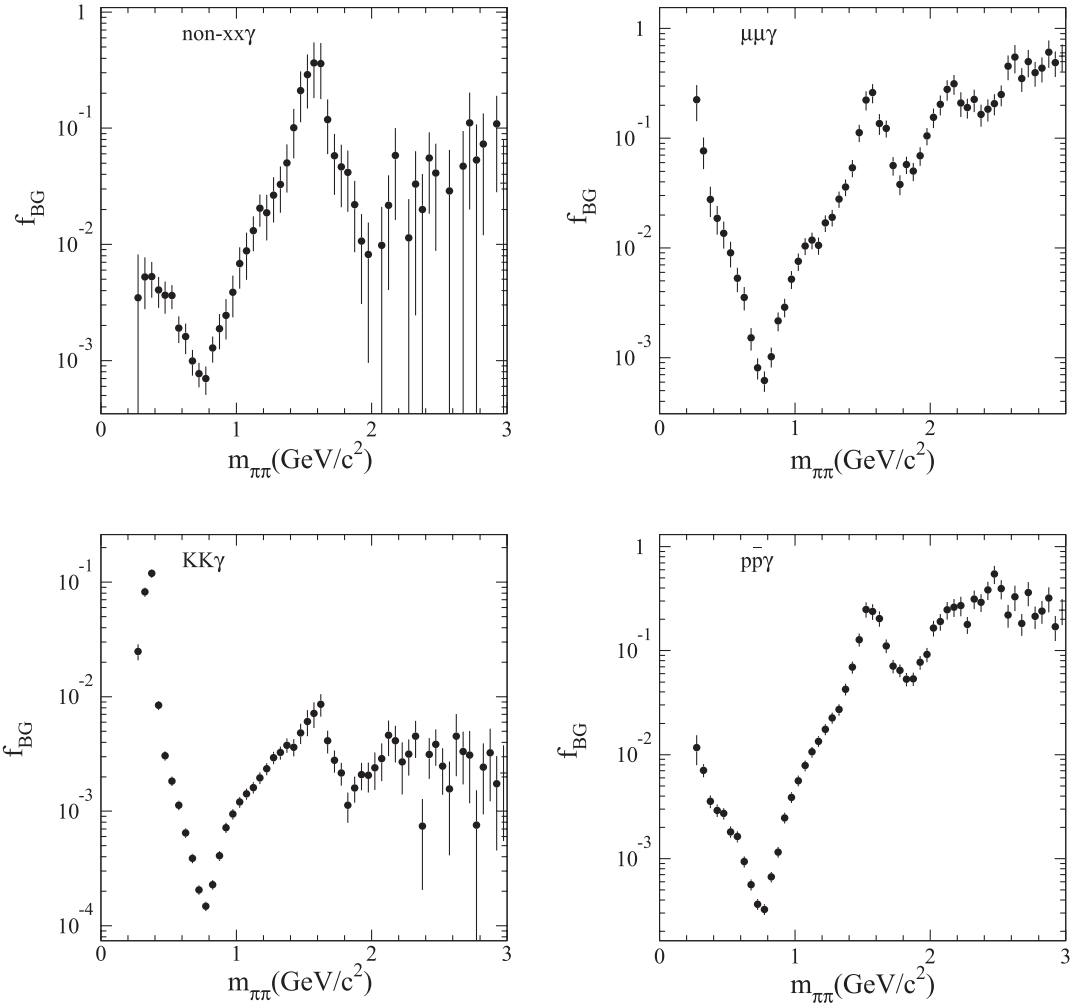


FIG. 37. The fractions of different backgrounds in the physical sample with the tight 2D- $\chi^2$  criterion and strengthened ' $\pi\pi_h$ '-ID (as used in the  $\rho$  tails region) as a function of the  $\pi\pi$  mass. (top left): Multihadrons, including  $\tau\tau$ . (top right):  $\mu\mu(\gamma)\gamma_{\text{ISR}}$  (data + measured mis-ID). (bottom left):  $KK(\gamma)\gamma_{\text{ISR}}$  (data + measured mis-ID). (bottom right):  $p\bar{p}\gamma_{\text{ISR}}$  (MC).

As discussed in Sec. VIII A, NLO approximations are made in simulation, which affect the acceptance. While the FSR prescription by PHOTOS is found to agree reasonably well with data, this is not the case for additional ISR as simulated in AfkQed. The problems have been studied in detail for muons, since they affect the absolute

measurement of the  $\mu\mu(\gamma)\gamma_{\text{ISR}}$  cross section and the comparison with QED. However here we deal with acceptance corrections that apply to the pion cross section measured from the ratio of the  $\pi\pi(\gamma)\gamma_{\text{ISR}}$  spectrum to the effective luminosity. As the additional ISR issues are common to the  $\pi\pi(\gamma)\gamma_{\text{ISR}}$  and  $\mu\mu(\gamma)\gamma_{\text{ISR}}$  channels, they

TABLE IV. Estimated background fractions (in %) in the ' $\pi\pi_h$ ' sample for  $m_{\pi\pi} = 0.325, 0.475, 0.975, 1.375, 1.975$ , and  $2.975 \text{ GeV}/c^2$ . The entries marked as “–” correspond to a negligible fraction. Processes with fractions less than 0.05% in all intervals are not listed. The quoted errors include both statistical and systematic uncertainties.

Process	$0.325 \text{ GeV}/c^2$	$0.475 \text{ GeV}/c^2$	$0.975 \text{ GeV}/c^2$	$1.375 \text{ GeV}/c^2$	$1.975 \text{ GeV}/c^2$	$2.975 \text{ GeV}/c^2$
$\mu\mu$	$7.7 \pm 2.5$	$1.4 \pm 0.4$	$0.5 \pm 0.1$	$3.6 \pm 0.6$	$10.5 \pm 1.9$	$56.2 \pm 15.8$
$KK$	$8.2 \pm 0.7$	$0.3 \pm 0.1$	$0.1 \pm 0.1$	$0.4 \pm 0.1$	$0.2 \pm 0.1$	$0.2 \pm 0.2$
$\gamma 2\pi\pi^0$	$0.4 \pm 0.2$	$0.3 \pm 0.1$	$0.1 \pm 0.1$	–	–	–
$q\bar{q}$	$0.1 \pm 0.1$	$0.1 \pm 0.1$	$0.3 \pm 0.2$	$5.0 \pm 2.2$	$0.8 \pm 0.7$	$3.4 \pm 4.5$
$\gamma p\bar{p}$	$0.7 \pm 0.1$	$0.3 \pm 0.1$	$0.4 \pm 0.1$	$4.3 \pm 0.5$	$9.2 \pm 1.4$	$24.5 \pm 6.8$
Total	$17.1 \pm 2.6$	$2.3 \pm 0.4$	$1.4 \pm 0.2$	$13.2 \pm 2.3$	$20.7 \pm 2.5$	$84.3 \pm 17.8$

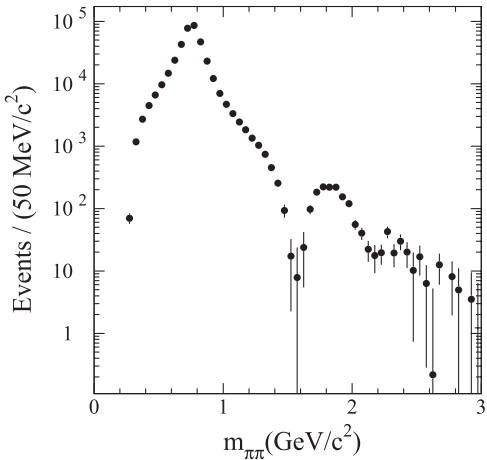


FIG. 38. The  $m_{\pi\pi}$  spectrum of  $\pi\pi(\gamma)\gamma_{\text{ISR}}$  events selected with ' $\pi\pi_h$ ' identification and the tight  $\ln(\chi^2_{\text{ISR}} + 1) < 3$  criterion, from threshold to  $3 \text{ GeV}/c^2$  in  $50 \text{ MeV}/c^2$  mass intervals.

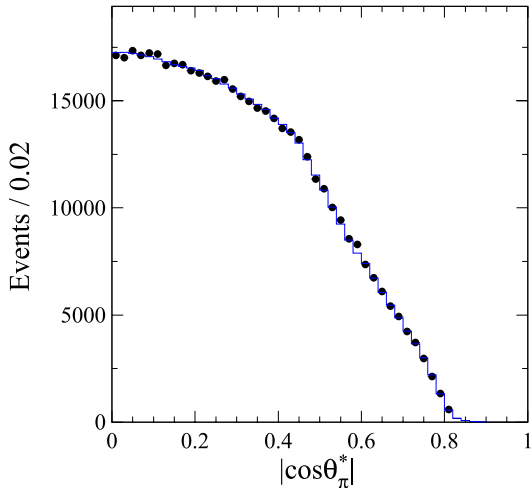


FIG. 39 (color online). The angular pion distribution in the  $\pi\pi$  system with respect to the ISR photon direction as function of  $|\cos\theta_\pi^*|$  for background-subtracted  $\pi\pi(\gamma)\gamma_{\text{ISR}}$  data (points) in the  $\rho$  central region ( $0.5 < m_{\pi\pi} < 1 \text{ GeV}/c^2$ ). The blue histogram is the shape obtained in the simulation, normalized to the data.

cancel in the  $R_{\text{exp}}(\sqrt{s'})$  ratio, except for second-order effects addressed below. Thus the  $\pi\pi$  measurement does not rely on the accurate description of NLO effects by the MC generator, a fact that is a strength of this analysis method.

Acceptance, including preselection efficiency, is mainly affected by kinematics, i.e., the angular and energy distributions of the hard additional ISR photon. We study these effects for the pion channel as we have done for the muon channel, using AfkQed and Phokhara at the generator level and fast simulation with parametrized efficiencies and resolutions. The resulting data/MC correction on acceptance for pions is consistent with the correction obtained

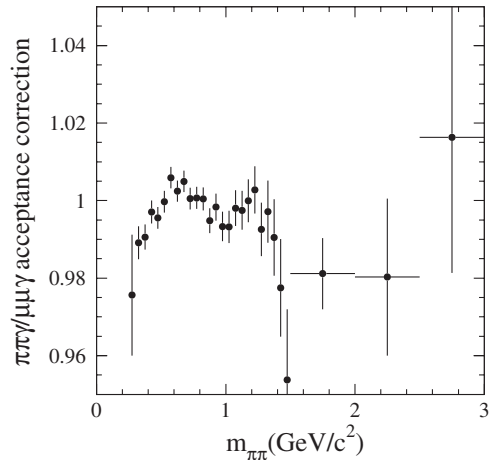


FIG. 40. The full correction to the  $\epsilon_{\pi\pi(\gamma)\gamma_{\text{ISR}}} / \epsilon_{\mu\mu(\gamma)\gamma_{\text{ISR}}}$  acceptance ratio for noncanceling effects (see text).

for muons. Second-order corrections induced by pion secondary interactions are investigated, using the full simulation. The total acceptance correction amounts to a few  $\times 10^{-3}$  in the  $\rho$  mass region. It is shown as a function of the  $\pi\pi$  mass in Fig. 40. As for the other corrections, the statistical uncertainties are included in the final cross section errors. Since part of the correction is derived using the fast simulation at the generator level, a significant fraction of the correction  $\sim 25\%$  is taken as a systematic uncertainty,  $10^{-3}$  in the  $0.6\text{--}0.9 \text{ GeV}/c^2$  region and larger outside.

## E. Summary of the treatment of statistical uncertainties

The statistical covariance matrix of the cross section includes the bin-to-bin correlations affecting the  $\pi\pi$  spectrum and the luminosity.

The statistical covariance matrix of the  $\pi\pi$  spectrum is not diagonal, due firstly to correlations introduced by the transfers of events in the unfolding process. In addition, the data/MC efficiency corrections and subtracted background spectra are initially computed in  $50 \text{ MeV}/c^2$  bins, but applied to spectra with  $2 \text{ MeV}/c^2$  bins (in the central  $\rho$  region) or  $10 \text{ MeV}/c^2$  bins (in the  $\rho$  tail regions) using splines. The resulting covariance matrix is obtained from a large series of toy experiments.

The ratio of the measured luminosity to the LO luminosity including vacuum polarization is initially computed in (almost) uncorrelated bins of  $50 \text{ MeV}$ . The procedure of sliding bins, used for smoothing this distribution, introduces correlations between the final values (Sec. VIII F 3). The luminosity errors for the final cross section (2 or  $10 \text{ MeV}$ ) bins are 100% correlated within a  $50 \text{ MeV}$  bin, whereas additional correlations occur between the  $50 \text{ MeV}$  bins because of the bin-sliding procedure. Finally, the correlation effect from unfolding the  $\mu\mu$  spectrum is rather weak, but it is however propagated to the final correlation matrix.

TABLE V. Systematic uncertainties (in  $10^{-3}$ ) on the cross section for  $e^+e^- \rightarrow \pi\pi(\gamma_{\text{FSR}})$  from the determination of the various efficiencies in different  $\pi\pi$  mass ranges (in  $\text{GeV}/c^2$ ). The statistical part of the efficiency measurements is included in the total statistical error in each mass bin. The last line gives the total systematic uncertainty on the  $\pi\pi$  cross section, including the systematic error on the ISR luminosity from muons.

Sources	0.3–0.4	0.4–0.5	0.5–0.6	0.6–0.9	0.9–1.2	1.2–1.4	1.4–2.0	2.0–3.0
Trigger/filter	5.3	2.7	1.9	1.0	0.7	0.6	0.4	0.4
Tracking	3.8	2.1	2.1	1.1	1.7	3.1	3.1	3.1
$\pi$ -ID	10.1	2.5	6.2	2.4	4.2	10.1	10.1	10.1
Background	3.5	4.3	5.2	1.0	3.0	7.0	12.0	50.0
Acceptance	1.6	1.6	1.0	1.0	1.6	1.6	1.6	1.6
Kinematic fit ( $\chi^2$ )	0.9	0.9	0.3	0.3	0.9	0.9	0.9	0.9
Correl. $\mu\mu$ ID loss	3.0	2.0	3.0	1.3	2.0	3.0	10.0	10.0
$\pi\pi/\mu\mu$ non-cancel.	2.7	1.4	1.6	1.1	1.3	2.7	5.1	5.1
Unfolding	1.0	2.7	2.7	1.0	1.3	1.0	1.0	1.0
ISR luminosity	3.4	3.4	3.4	3.4	3.4	3.4	3.4	3.4
Sum (cross section)	13.8	8.1	10.2	5.0	6.5	13.9	19.8	52.4

### F. Systematic errors

Systematic uncertainties affecting the  $\pi\pi$  sample in different mass regions are now summarized. The statistical errors of the measured efficiencies are included with the main statistical uncertainty on the  $\pi\pi$  mass spectrum. However, in some cases, remaining systematic uncertainties are attached to the efficiency measurement process and quoted as such. Details have been given for each efficiency study in Secs. IV and VB. The results for all systematic uncertainties are listed in Table V.

The overall relative systematic uncertainty on the  $\pi\pi(\gamma_{\text{FSR}})$  cross section is  $5.0 \times 10^{-3}$  in the 0.6–0.9  $\text{GeV}$  range, but significantly larger below and above the central region. For comparison, the statistical error of the measured efficiency corrections amounts to  $4.7 \times 10^{-3}$  at the  $\rho$  peak, while the statistical error of the raw spectrum is 1.35% at that mass.

A full treatment of the systematic uncertainties is implemented, using a covariance matrix. To achieve this we consider the individual systematic errors (for each source, as given in Table V) to be 100% correlated in all the mass bins. Then the total systematic covariance matrix is built as the sum of the covariance matrices corresponding to each individual systematic source.

### G. Consistency check with tight and loose $\chi^2$ selection

The loose  $\chi^2$  criterion is used in the  $\rho$  central region, while the tight one is used in the tails where backgrounds are larger. However it is possible to compare the results obtained with the two selections in the central region. This provides a test of the  $\chi^2$  selection efficiency and of the multihadronic background. The test is also sensitive to unfolding, as mass resolutions are different in different 2D- $\chi^2$  regions. For this test, events are selected with the “ $\rho$  central” conditions, and with either the tight or loose  $\chi^2$  criterion.

The result of the test is expressed as the ratio of the efficiency-corrected and unfolded spectra for the loose

over the tight  $\chi^2$  selections. The fitted value of this ratio over the full central range ( $0.5$ – $1.0$   $\text{GeV}/c^2$ ) is found to be consistent with unity within errors,  $0.9983 \pm 0.0049$  with a  $\chi^2/\text{DF}$  of  $53.6/49$  for  $10 \text{ MeV}/c^2$  bins. Fits in  $100 \text{ MeV}/c^2$  intervals, given in Fig. 41, do not show any significant trend for a resolution mismatch between data and corrected MC. Deviations from unity are at a much smaller level than the resolution correction applied to the MC in the intermediate region (Sec. VII A, shown by the dashed histogram). They are also within the range of estimated uncertainties between the two  $\chi^2$  conditions (background and  $\chi^2$  selection efficiencies). We thus conclude that the procedure used for correcting the MC mass-transfer matrix is consistent within the quoted systematic uncertainties.

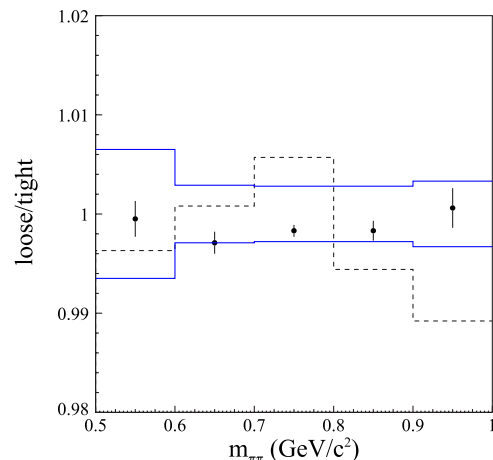


FIG. 41 (color online). The ratio of the corrected and unfolded mass spectra (data points) for loose over tight 2D- $\chi^2$  selection in the central  $\rho$  region fitted in  $100 \text{ MeV}/c^2$  bins, compared to the band of independently estimated uncertainties (solid lines). The MC mass-matrix resolution correction is shown as the dashed histogram.

## H. Cross section results

### 1. Estimates of LO FSR in the $\pi\pi(\gamma)\gamma$ process

In Eq. (3) it is assumed that the contribution of LO FSR to the  $\pi\pi(\gamma)\gamma$  cross section is negligible. This approximation is supported by calculations using specific models.

The simplest model uses an extrapolation of the pion form factor to the large value of  $s \sim 112$  GeV<sup>2</sup>, and assumes pointlike pions to compute LO FSR photon emission, as for additional FSR. This procedure, questionable for large energies  $E_\gamma^* > 3$  GeV, yields a very small relative contribution from  $|\mathcal{A}_{\text{FSR}}|^2$ ,  $\delta_{\text{FSR}}^{\pi\pi} \sim 10^{-7}$ . A more realistic model [29] considers radiation from quarks and recombination into a pion pair, with the parametrization of the produced even-spin states based on Ref. [30]. In this case the contribution is at a few  $\times 10^{-4}$  level for masses below 1 GeV. However the FSR rate could be enhanced on specific resonances that are not explicitly taken into account in the model. Estimates [31] using a  $\gamma^*\gamma f_2(1270)$  transition form factor evaluated in the asymptotic regime by perturbative QCD indicate a FSR contribution of about 0.9% on the  $f_2(1270)$  resonance. Contributions from  $f_0(980)$  and  $f_0(1370)$  are expected to be lower.

Finally, a direct test with *BABAR* data has been performed with a measurement of charge asymmetry, which is proportional to the interference between LO ISR and FSR amplitudes. This work in progress, which will be published separately, yields results that do not exceed the estimates above.

The estimated LO FSR contributions are at levels smaller than the quoted systematic uncertainties on the  $\pi\pi(\gamma)\gamma$  cross section, much smaller actually for the  $\rho$  region. No subtraction has been applied to the measured cross section.

### 2. Results on the bare cross section with FSR

The results for the  $e^+e^- \rightarrow \pi^+\pi^-(\gamma_{\text{FSR}})$  bare cross section including FSR,  $\sigma_{\pi\pi(\gamma_{\text{FSR}})}^0$ , are given in Figs. 42–44 as a function of  $\sqrt{s'}$ . The cross section is

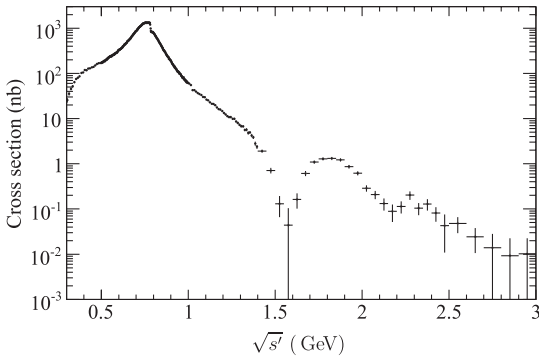


FIG. 42. The measured cross section for  $e^+e^- \rightarrow \pi^+\pi^-(\gamma)$  over the full mass range. Systematic and statistical uncertainties are shown, but based only on the diagonal elements of the covariance matrix (see text).

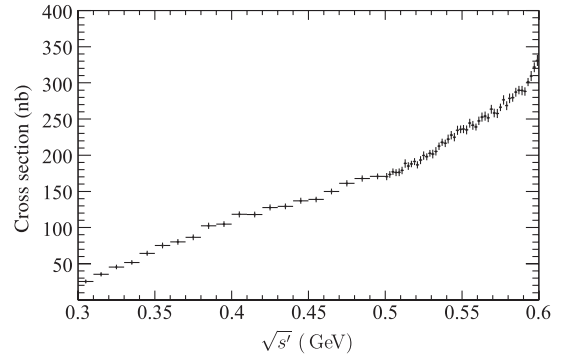


FIG. 43. The measured cross section for  $e^+e^- \rightarrow \pi^+\pi^-(\gamma)$  in the lower mass range. Systematic and statistical uncertainties are shown, but based only on the diagonal elements of the covariance matrix (see text).

dominated by the wide  $\rho$  resonance, with structures at larger masses. The dip region near 1.6 GeV, usually interpreted as resulting from interference between the  $\rho'$  and  $\rho''$  amplitudes, is mapped with a much increased precision compared to previous experiments. There is also an indication for a structure in the 2.2–2.25 GeV region, which could be due to a still higher-mass  $\rho'''$  vector meson.

Files containing the cross section data and their covariance matrices are provided in the Supplemental Material repository [32].

### I. Pion form factor fits

The square of the pion form factor is defined as usual by the ratio of the dressed cross section without FSR, divided by the lowest-order cross section for pointlike spin 0 charged particles. Thus,

$$|F_\pi|^2(s') = \frac{3s'}{\pi\alpha^2(0)\beta_\pi^3} \sigma_{\pi\pi}(s'), \quad (24)$$

with

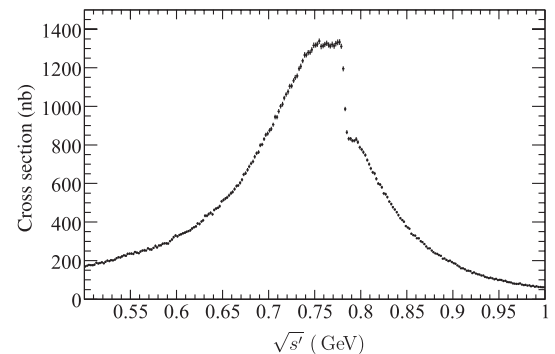


FIG. 44. The measured cross section for  $e^+e^- \rightarrow \pi^+\pi^-(\gamma)$  in the  $\rho$  region. Systematic and statistical uncertainties are shown, but based only on the diagonal elements of the covariance matrix (see text).

$$\sigma_{\pi\pi}(s') = \frac{\sigma_{\pi\pi}^0(s')}{1 + \delta_{\text{add.FSR}}^{\pi\pi}} \left( \frac{\alpha(s')}{\alpha(0)} \right)^2, \quad (25)$$

and  $\beta_\pi$  the pion velocity. The FSR correction [25,26],  $\delta_{\text{add.FSR}}^{\pi\pi} = \alpha(0)/\pi\eta(s')$ , decreases slowly with  $s'$  and amounts to  $8.0 \times 10^{-3}$  at the  $\rho$  mass.

A vector-dominance model is used to fit the *BABAR* pion form factor. It is a way to interpret the observed

$$F_\pi(s) = \frac{\text{BW}_\rho^{\text{GS}}(s, m_\rho, \Gamma_\rho) \frac{1 + c_\omega \text{BW}_\omega^{\text{KS}}(s, m_\omega, \Gamma_\omega)}{1 + c_\omega} + c_{\rho'} \text{BW}_{\rho'}^{\text{GS}}(s, m_{\rho'}, \Gamma_{\rho'}) + c_{\rho''} \text{BW}_{\rho''}^{\text{GS}}(s, m_{\rho''}, \Gamma_{\rho''}) + c_{\rho'''} \text{BW}_{\rho'''}^{\text{GS}}(s, m_{\rho'''}, \Gamma_{\rho'''})}{1 + c_{\rho'} + c_{\rho''} + c_{\rho'''}}, \quad (26)$$

which satisfies  $F_\pi(0) = 1$ . The amplitudes of the Breit-Wigner (BW) functions are complex:  $c_\omega = |c_\omega| e^{i\phi_\omega}$ ,  $c_{\rho'} = |c_{\rho'}| e^{i\phi_{\rho'}}$ ,  $c_{\rho''} = |c_{\rho''}| e^{i\phi_{\rho''}}$  and  $c_{\rho'''} = |c_{\rho'''}| e^{i\phi_{\rho'''}}$ . The BW of the  $\omega$  is taken as

$$\text{BW}_\omega^{\text{KS}}(s, m, \Gamma) = \frac{m^2}{m^2 - s - im\Gamma}. \quad (27)$$

The wide  $\rho$ ,  $\rho'$ ,  $\rho''$  and  $\rho'''$  resonances are described by the Gounaris-Sakurai (GS) model [33], which takes into account the variation of their width with energy:

$$\text{BW}^{\text{GS}}(s, m, \Gamma) = \frac{m^2(1 + d(m)\Gamma/m)}{m^2 - s + f(s, m, \Gamma) - im\Gamma(s, m, \Gamma)}, \quad (28)$$

with

$$\Gamma(s, m, \Gamma) = \Gamma \frac{s}{m^2} \left( \frac{\beta_\pi(s)}{\beta_\pi(m^2)} \right)^3, \quad (29)$$

where  $\beta_\pi(s) = \sqrt{1 - 4m_\pi^2/s}$ . In principle this energy dependence is justified only below 1 GeV, as 4-pion final states dominate at larger energies, but it is used for simplicity. Detailed studies of the high mass states cannot be performed only on the basis of pion form factor fits, and require complex coupled-channel analyses. Such studies are beyond the scope of this paper, but the present  $2\pi$  data constitute a very useful ingredient for them.

The auxiliary functions used in the GS model are

$$d(m) = \frac{3}{\pi} \frac{m_\pi^2}{k^2(m^2)} \ln \left( \frac{m + 2k(m^2)}{2m_\pi} \right) + \frac{m}{2\pi k(m^2)} - \frac{m_\pi^2 m}{\pi k^3(m^2)}, \quad (30)$$

$$f(s, m, \Gamma) = \frac{\Gamma m^2}{k^3(m^2)} [k^2(s)(h(s) - h(m^2)) + (m^2 - s)k^2(m^2)h'(m^2)], \quad (31)$$

where

$$k(s) = \frac{1}{2}\sqrt{s}\beta_\pi(s), \quad (32)$$

$$h(s) = \frac{2}{\pi} \frac{k(s)}{\sqrt{s}} \ln \left( \frac{\sqrt{s} + 2k(s)}{2m_\pi} \right). \quad (33)$$

and  $h'(s)$  is the derivative of  $h(s)$ .

structures beyond the  $\rho$  resonance in terms of higher-mass isovector vector mesons. The fit also provides a convenient means to interpolate through the *BABAR* data points in order to facilitate the comparison to other experiments.

The VDM parameterization, including  $\rho - \omega$  interference, is given by:

The form factor data is fitted in the full energy range, from 0.3 to 3.0 GeV, involving 18 free parameters: the mass and width of the  $\rho$ , and for each other resonance ( $\omega$ ,  $\rho'$ ,  $\rho''$ ,  $\rho'''$ ) the amplitude (modulus and phase) with respect to the  $\rho$ , and mass and width. According to a well-known effect [34], the  $\chi^2$  minimization returns fitted values that are systematically shifted with respect to the data points when the full covariance matrix is used in the fit, while the fit using diagonal errors is verified to be bias-free. This feature is due to correlations, which here arise from both statistical and systematic origins, but mostly from the ISR-luminosity 50 MeV sliding bins (Sec. VIII F 3) and systematic errors. To circumvent the problem, we fit the data with only diagonal errors to obtain the central values of the fitted parameters. The error on each parameter is taken as the largest error obtained from the fit either with the full covariance matrix or with only diagonal errors. The biases on the mass scale calibration and the resolution obtained in Secs. VII B and VII C are included in the fit results on the  $\rho$  and  $\omega$  resonance parameters in Table VI, with the corresponding systematic uncertainties indicated.

As shown in Fig. 45, the VDM fit provides an adequate description of the *BABAR* data over the full 0.3–3 GeV range ( $\chi^2/\text{DF} = 351/319$ ). The goodness of the fit shows that the GS parametrization of the dominant  $\rho$  resonance describes the data in a reasonable manner, as well as the contributions from the higher  $\rho'$ ,  $\rho''$  and  $\rho'''$  resonances. In particular the strong interference dip near 1.6 GeV is well reproduced. Beyond 2 GeV, the  $\rho'''$  is required in order to reproduce the structure seen in the data. The quality of the fit is shown in more detail in Fig. 46 in the low-mass range and in the  $\rho$  peak region with the  $\rho - \omega$  interference.

The relative ratio ( $|F_\pi|_{\text{data}}^2 / |F_\pi|_{\text{VDM}}^2 - 1$ ) is shown in Fig. 47 over the full energy range. Some deviation is observed in the low-mass region where the fit underestimates the data. Some oscillation is also observed between 0.9 and 1.2 GeV. This shows that the GS function, the parameters of which are mainly determined in the  $\rho$  peak region, together with the constraint at  $s' = 0$ , does not accurately describe the resonance tails. At higher masses, the validity of the VDM description that involves the parametrization of very

TABLE VI. Parameters obtained for the VDM fit (described in the text) to the *BABAR* pion form factor data. The errors include both statistical and systematic uncertainties. The errors shown in parentheses for the  $\rho$  and  $\omega$  parameters stem from the mass calibration and resolution uncertainties (see text).

Parameter	Value $\pm$ Error
$m_\rho$ (MeV/c $^2$ )	$775.02 \pm 0.31 (\pm 0.16)$
$\Gamma_\rho$ (MeV)	$149.59 \pm 0.67 (\pm 0.02)$
$m_\omega$ (MeVc $^2$ )	$781.91 \pm 0.18 (\pm 0.16)$
$\Gamma_\omega$ (MeV)	$8.13 \pm 0.36 (\pm 0.27)$
$ c_\omega $	$(1.644 \pm 0.061) \times 10^{-3}$
$\phi_\omega$ (rad)	$-0.011 \pm 0.037$
$m_{\rho'}$ (MeV/c $^2$ )	$1493 \pm 15$
$\Gamma_{\rho'}$ (MeV)	$427 \pm 31$
$ c_{\rho'} $	$0.158 \pm 0.018$
$\phi_{\rho'}$ (rad)	$3.76 \pm 0.10$
$m_{\rho''}$ (MeV/c $^2$ )	$1861 \pm 17$
$\Gamma_{\rho''}$ (MeV)	$316 \pm 26$
$ c_{\rho''} $	$0.068 \pm 0.009$
$\phi_{\rho''}$ (rad)	$1.39 \pm 0.20$
$m_{\rho'''}$ (MeV/c $^2$ )	$2254 \pm 22$
$\Gamma_{\rho'''}$ (MeV)	$109 \pm 76$
$ c_{\rho'''} $	$0.0051^{+0.0034}_{-0.0019}$
$\phi_{\rho'''}$ (rad)	$0.70 \pm 0.51$

broad resonances with large inelasticity, is somewhat arguable. However the overall agreement is satisfactory, notably in the 0.5–1.0 GeV region.

We compare the results for the resonance parameters (Table VI) to those obtained by other experiments, noting that the comparison can be biased if the mass range or the parametrizations are different. The fitted  $\rho$  parameters are compared to the results from CMD-2 [35] and SND [36]: for the mass  $m_\rho$ , these two experiments obtain  $(776.0 \pm 0.8)$  MeV/c $^2$  and  $(774.6 \pm 0.6)$  MeV/c $^2$ , respectively, while for the width  $\Gamma_\rho$ , they obtain  $(146.0 \pm 0.9)$  MeV and  $(146.1 \pm 1.7)$  MeV. The fitted value of the phase  $\phi_\omega$  of the  $\rho - \omega$  interference is not in good agreement with the CMD-2 value  $(0.182 \pm 0.067)$  rad; SND uses a different parametrization. However in the CMD-2 fit, the  $\omega$  mass is

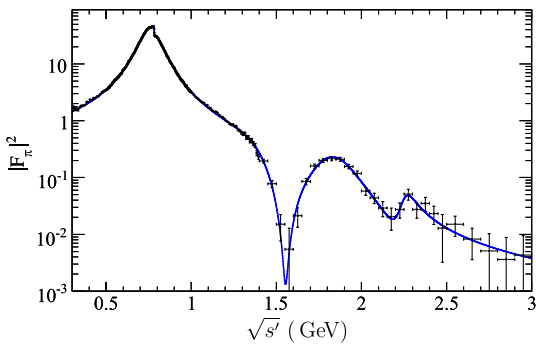


FIG. 45 (color online). The pion form factor-squared measured by *BABAR* as a function of  $\sqrt{s'}$  from 0.3 to 3 GeV and the VDM fit described in the text.

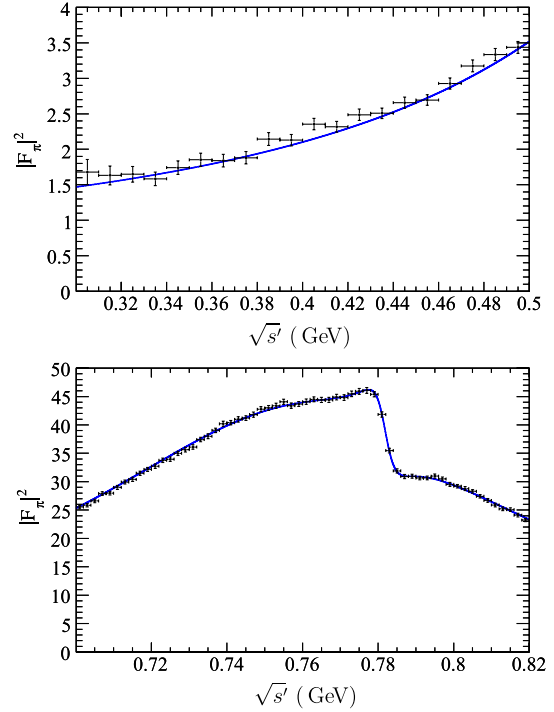


FIG. 46 (color online). The pion form factor-squared measured by *BABAR* as a function of  $\sqrt{s'}$  and the VDM fit from 0.3 to 3 GeV described in the text. (top): Low-mass region (0.3–0.5 GeV). (bottom):  $\rho$  peak region with  $\rho - \omega$  interference (0.70–0.82 GeV).

fixed to the world-average value  $m_\omega = 782.65$  MeV/c $^2$  [24]. If we fix  $m_\omega$  to this value in the *BABAR* fit, the phase comes out to be  $(0.137 \pm 0.023)$  rad, in agreement with CMD-2. In fact in the 18-parameter fit the fitted values for  $m_\omega$ ,  $\phi_\omega$ , and  $c_\omega$  are strongly correlated (80%). The fitted  $\omega$  width  $\Gamma_\omega$  is found to be consistent with the world-average value  $(8.49 \pm 0.08)$  MeV obtained from the dominant  $\pi^+ \pi^- \pi^0$  decay mode [24].

As the CMD-2 and SND experiments at Novosibirsk are well calibrated in energy with the resonant depolarization method, one can use the VDM fit to check the mass calibration by leaving the  $\omega$  mass free, and using the CMD-2 result for the  $\rho - \omega$  phase. One obtains

$$m_\omega = (782.68 \pm 0.12 \pm 0.27) \text{ MeV/c}^2, \quad (34)$$

where the first error is from the fit to the data and the second from the uncertainty on the CMD-2 value for  $\phi_\omega$ . The absolute difference with the world average  $\omega$  mass is

$$m_\omega^{\text{fit}} - m_\omega^{\text{PDG}} = (0.03 \pm 0.29) \text{ MeV/c}^2, \quad (35)$$

consistent with the calibration from the  $J/\psi$  study reported in Sec. VII B,  $(-0.16 \pm 0.16)$  MeV/c $^2$ .

## J. Comparison to other experiments

### 1. Pion form factor from $e^+ e^- \rightarrow \pi^+ \pi^-$ cross section

The measured form factor  $F_\pi(s')$  is compared to published data from the CMD-2 [35], SND [36], and KLOE

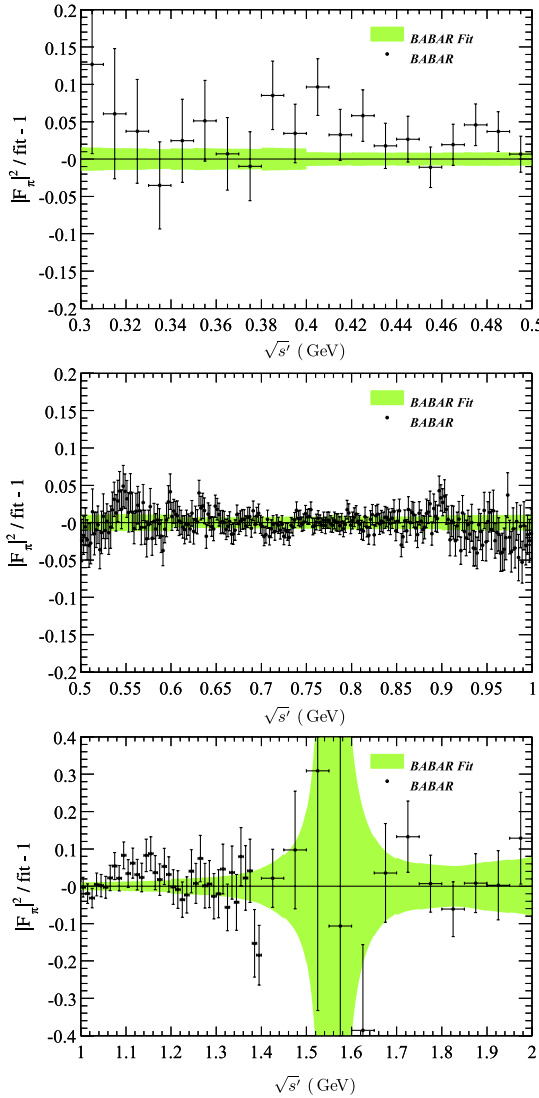


FIG. 47 (color online). The relative difference between the pion form factor-squared from *BABAR* data and the 18-parameter phenomenological fit in three mass regions. Systematic and statistical uncertainties are included for data (diagonal errors). The width of the band shows the propagation of statistical errors from the fit and the quoted systematic uncertainties, added quadratically.

experiments. While the Novosibirsk results are obtained in the scan mode at fixed energy points, KLOE, like *BABAR* uses the ISR method, albeit at a much smaller energy ( $\sqrt{s} = 1.02$  GeV). The KLOE [37] data are obtained without direct detection of the ISR photon. More recently, KLOE has performed a new analysis [38] where the ISR photon is detected at large angles, allowing them to collect data down to the threshold region.

The data of the other experiments are compared with the result from the *BABAR* form factor fit, which was shown in the previous section to describe well the *BABAR* data itself. Each plot shows the relative difference between the form factor-squared of the other experiment and *BABAR* as data

points, while the width of the band around zero is the result of the propagation of statistical errors from the *BABAR* fit with systematic uncertainties in each mass region (Table V) added quadratically.

The comparisons with other experiments are shown in Figs. 48 and 50, where the errors on the data points include both statistical and systematic uncertainties. The agreement looks rather reasonable with the CMD-2 and SND measurements within systematic errors, the *BABAR* results lying generally above on the lower side of the  $\rho$  resonance. The discrepancy is larger with KLOE on and above the  $\rho$  peak.

The region of the  $\rho - \omega$  interference is examined in more detail in Fig. 49. No evidence is found for a significant variation in the steep part of the interference pattern around the  $\omega$  mass, showing that the *BABAR* mass calibration is not shifted with respect to CMD-2 and SND by more than 0.3 MeV/ $c^2$ .

The comparison of the form factor-squared in the low-mass region is made in Fig. 51. The agreement is reasonable, with some systematic departure with respect to the NA7 experiment at CERN. A direct cross section comparison is made in the large mass region in Fig. 52. The *BABAR* results agree with CMD-2 up to 1.4 GeV, while the DM2 cross section [28] appears to be larger by about 30–40%.

The comparison in relative terms of *BABAR* to other experiments is presented in Figs. 53 and 54 for masses lower than 0.5 GeV and between 1.0 and 1.4 GeV, respectively. The small discrepancy noticed between the *BABAR* fit and CMD-2 is in fact also observed in Fig. 47 where *BABAR* data are compared to the fit. So it points to a problem in the VDM parametrization rather than in the data.

## 2. $\tau$ spectral functions

It is also appropriate to compare the present results to the  $\tau \rightarrow \nu_\tau \pi\pi^0$  spectral function. Taking isospin-breaking (IB) into account, the conserved vector current (CVC) relation between the  $e^+ e^- \rightarrow \pi^+ \pi^- (\gamma)$  bare cross section with FSR  $\sigma_{\pi^+ \pi^- (\gamma)}^0$  and the normalized hadronic invariant mass distribution in  $\tau \rightarrow \nu_\tau \pi\pi^0$  decays is modified [39,40] as follows:

$$\sigma_{\pi^+ \pi^- (\gamma)}^0 = \frac{1}{D(s)} \frac{B_{\pi\pi}}{B_e} \left( \frac{1}{N_{\pi\pi}} \frac{dN_{\pi\pi}}{ds} \right) \frac{R_{IB}}{S_{EW}} \left( 1 + \frac{\alpha(0)}{\pi} \eta(s) \right), \quad (36)$$

where

$$D(s) = \frac{3|V_{ud}|^2 s}{2\pi\alpha(0)^2 m_\tau^2} \left( 1 - \frac{s}{m_\tau^2} \right)^2 \left( 1 + \frac{2s}{m_\tau^2} \right), \quad (37)$$

and

$$R_{IB}(s) = \frac{1}{G_{EM}(s)} \left( \frac{\beta_0}{\beta_-} \right)^3 \frac{|F_0(s)|^2}{|F_-(s)|^2}. \quad (38)$$

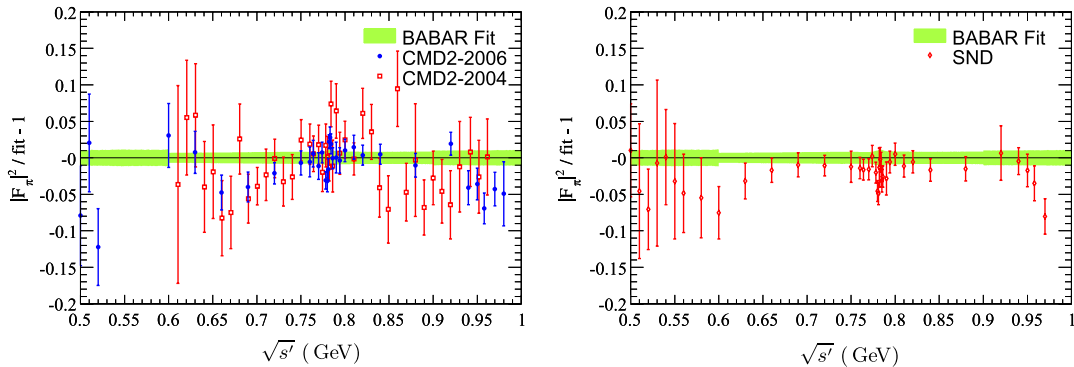


FIG. 48 (color online). The relative difference of pion form factor-squared from the *BABAR* fit in the 0.5–1 GeV region with CMD-2 (left) and with SND (right). Systematic and statistical uncertainties are included in the data points. The width of the *BABAR* band shows the propagation of statistical errors from the fit and the quoted systematic uncertainties, added quadratically.

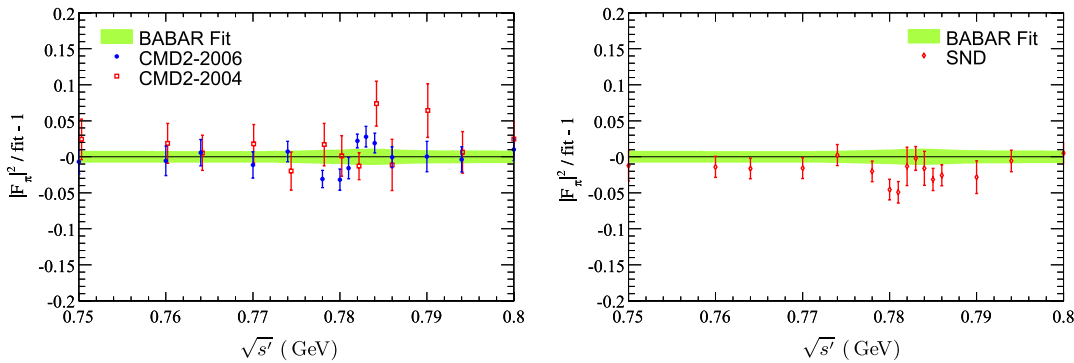


FIG. 49 (color online). The relative difference of pion form factor-squared from the *BABAR* fit in the  $\rho - \omega$  mass region with CMD-2 (left) and with SND (right). Systematic and statistical uncertainties are included in the data points. The width of the *BABAR* band shows the propagation of statistical errors from the fit and the quoted systematic uncertainties, added quadratically.

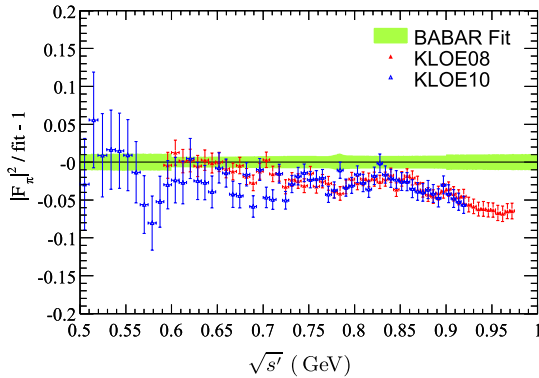


FIG. 50 (color online). The relative difference of pion form factor-squared from KLOE and the *BABAR* fit in the 0.5–1 GeV region. Systematic and statistical uncertainties are included in the data points. The width of the *BABAR* band shows the propagation of statistical errors from the fit and the quoted systematic uncertainties, added quadratically.

$B_{\pi\pi}$  and  $B_e$  are the branching fractions for  $\tau$  decay into the  $\nu_\tau\pi\pi^0$  and  $\nu_\tau e\bar{\nu}_e$  final states.  $G_{\text{EM}}(s)$  is the long-distance QED radiative correction and  $S_{\text{EW}}$  the short-distance electroweak radiative correction.  $F_0(s)$  and  $F_-(s)$  are the

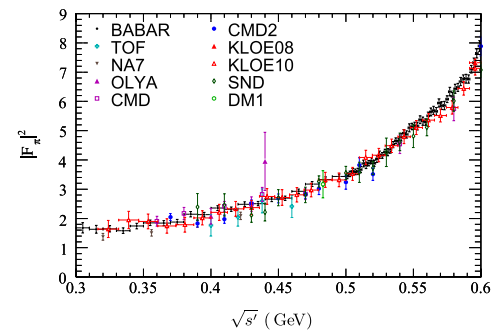


FIG. 51 (color online). The measured pion form factor-squared compared to published results from other experiments. Systematic and statistical uncertainties are shown for all results, with the diagonal elements of the *BABAR* covariance matrix.

electromagnetic and weak form factors, while  $\beta_0$  and  $\beta_-$  are the pion velocities in the  $\pi^+\pi^-$  and  $\pi\pi^0$  center-of-mass systems, respectively.

Isospin-breaking corrections have been recently reevaluated [6], and a new  $\tau$  analysis for the muon  $g - 2$  presented, taking advantage of the Belle data. It updates the

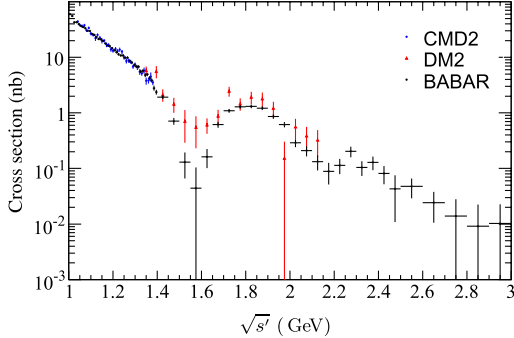


FIG. 52 (color online). The measured cross section for  $e^+e^- \rightarrow \pi^+\pi^-(\gamma)$  compared to published results from CMD-2 up to 1.4 GeV and DM2 above. Systematic and statistical uncertainties are shown for all results, with the diagonal elements of the *BABAR* covariance matrix.

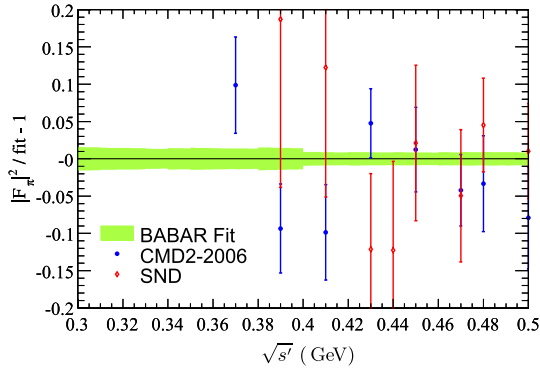


FIG. 53 (color online). The relative difference of pion form factor-squared from CMD-2 and SND and the *BABAR* fit in the region below 0.5 GeV. Systematic and statistical uncertainties are included in the data points. The width of the *BABAR* band shows the propagation of statistical errors from the fit and the quoted systematic uncertainties, added quadratically.

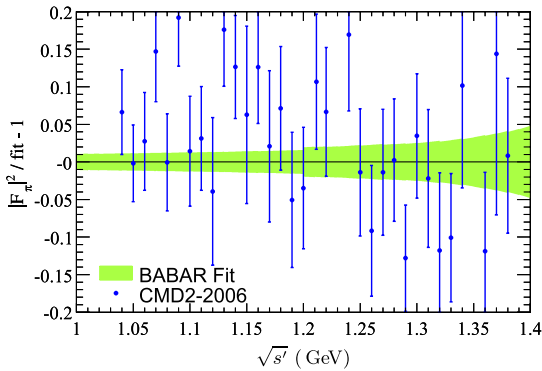


FIG. 54 (color online). The relative difference of pion form factor-squared from CMD-2 and the *BABAR* fit in the region above 1 GeV. Systematic and statistical uncertainties are included in the data points. The width of the *BABAR* band shows the propagation of statistical errors from the fit and the quoted systematic uncertainties, added quadratically.

previous analysis [2]. The  $G_{EM}$  factor takes also into account  $\rho - \omega$  interference, and the charged and neutral  $\rho$  mass difference, a charged and neutral  $\rho$  width difference from radiative decays, and the  $m_{\pi^\pm} - m_{\pi^0}$  mass difference in the form factor [41]. Other recent approaches to IB breaking have been considered, often based on specific models [42,43].

Using the results from Ref. [6] the corrected  $\tau$  and *BABAR* data can be compared directly. This is achieved

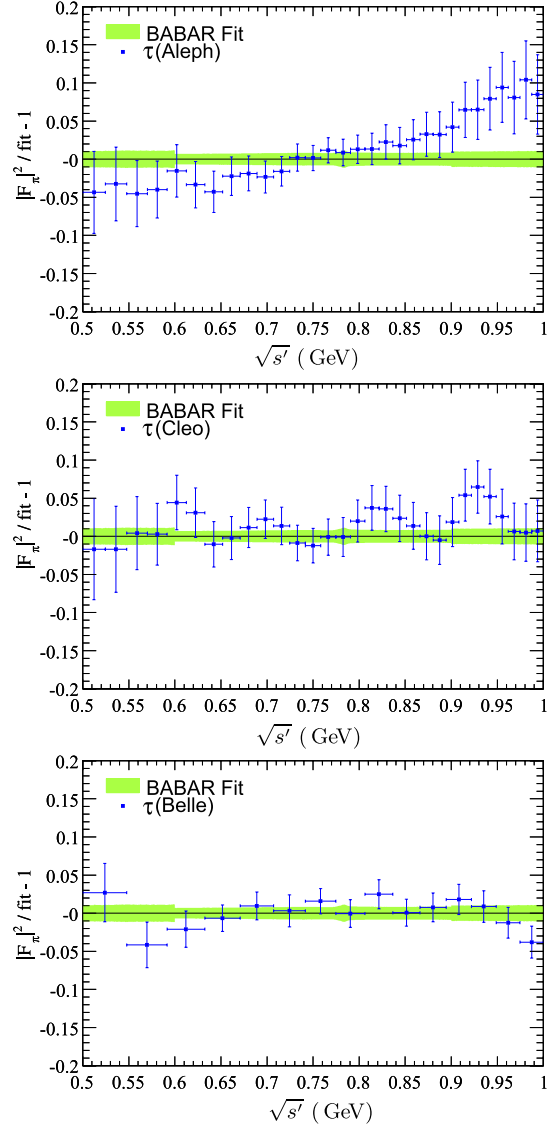


FIG. 55 (color online). The relative difference of the form factor-squared from the  $\tau$  data of ALEPH (top), CLEO (middle) and Belle (bottom) with respect to the  $e^+e^- \rightarrow \pi^+\pi^-$  *BABAR* measurements in the 0.5–1 GeV region. Systematic and statistical uncertainties are included in the data points. The width of the *BABAR* band shows the propagation of statistical errors from the fit and the quoted systematic uncertainties, added quadratically. The  $\tau$  data are normalized to the value of  $B_{\pi\pi}$  measured by each experiment independently.

in Figs. 55, for the ALEPH [44], CLEO [45], and Belle [46] experiments, in a manner similar to the  $e^+e^-$  comparisons. Here there is another uncertainty resulting from the IB theoretical corrections, corresponding roughly to a scale uncertainty of 0.3%. For this comparison the spectral functions are normalized by the  $B_{\pi\pi} \equiv B(\tau \rightarrow \pi\pi^0\nu_\tau)$  value measured by each experiment, rather than using the world average as usually done. In this way the spectral functions are really independent. The errors on the  $\tau$  data points include all sources of statistical and systematic uncertainties,  $B_{\pi\pi}$  and IB corrections.

The comparison with ALEPH shows consistency within the systematic uncertainties up to the  $\rho$  peak and some slope above, with the remark that the ALEPH points are strongly correlated. Agreement is also observed within errors with the results of CLEO and Belle, CLEO being somewhat in between ALEPH and Belle above 0.8 GeV.

## X. THE $\pi\pi$ CONTRIBUTION TO THE ANOMALOUS MUON MAGNETIC MOMENT

### A. The *BABAR* result

The lowest-order loop contribution of the  $\pi\pi(\gamma)$  intermediate state to the muon magnetic anomaly is given by [47]

$$a_\mu^{\pi\pi(\gamma),\text{LO}} = \frac{1}{4\pi^3} \int_{4m_\pi^2}^\infty ds K(s) \sigma_{\pi\pi(\gamma)}^0(s), \quad (39)$$

where  $K(s)$  is the QED kernel [48],

$$K(s) = x^2 \left(1 - \frac{x^2}{2}\right) + (1+x)^2 \left(1 + \frac{1}{x^2}\right) \left[ \ln(1+x) - x + \frac{x^2}{2} \right] + x^2 \ln x \frac{1+x}{1-x}, \quad (40)$$

with  $x = (1 - \beta_\mu)/(1 + \beta_\mu)$  and  $\beta_\mu$  the muon velocity.

The integration is carried out numerically over the measured cross section per mass bins. The statistical and systematic errors are computed using the corresponding covariance matrices described in Secs. IXE and IXF.

Several tests are performed.

- (i) When the integral is performed with the original 50 MeV bins of ISR luminosity the result is  $(514.40 \pm 2.54 \pm 3.11) \times 10^{-10}$  in the range 0.3–1.8 GeV, while the value  $(513.54 \pm 2.22 \pm 3.11) \times 10^{-10}$  is obtained with the chosen sliding-bin method. The difference is consistent with the statistical fluctuations of the luminosity in the 50 MeV bins (Fig. 34) and the  $K(s)$  kernel weighting effect in the  $a_\mu$  integral.
- (ii) In the 0.5–1.0 GeV range one compares the results obtained with the “ $\rho$  central” and the “ $\rho$  tails” conditions. The main difference is the  $\chi^2$  selection, which affects the background level, the  $\chi^2$  efficiency, and the mass resolution, hence the performance of the unfolding. For the 0.5–1.0 GeV range, the result of the integration with the “central”

TABLE VII. Evaluation of  $a_\mu^{\pi\pi(\gamma),\text{LO}}$  using the *BABAR* data in different mass regions (see text for details). The first error is statistical and the second systematic.

$m_{\pi\pi}$ range (GeV)	$a_\mu^{\pi\pi(\gamma),\text{LO}} (\times 10^{-10})$
0.28–0.30	$0.55 \pm 0.01 \pm 0.01$
0.30–0.50	$57.62 \pm 0.63 \pm 0.55$
0.50–1.00	$445.94 \pm 2.10 \pm 2.51$
1.00–1.80	$9.97 \pm 0.10 \pm 0.09$
0.28–1.80	$514.09 \pm 2.22 \pm 3.11$

conditions is  $445.94 \times 10^{-10}$  in 2 MeV bins, and  $446.56 \times 10^{-10}$  with the “tails” conditions in 10 MeV bins. Thus the effect of different resolution and efficiencies has little effect on the integral. The difference of  $0.62 \times 10^{-10}$  between the two analyses is consistent with their estimated noncommon systematic errors and noncommon statistical errors, which induce an uncertainty on the integral of  $1.8 \times 10^{-10}$ .

The evaluation of the integral in the threshold region was performed in previous estimates [2] using a polynomial expansion in  $s'$  for the pion form factor, incorporating constraints on the normalization that  $F_\pi(0) = 1$  and that the derivative of the form factor at  $s' = 0$  be given by the known quadratic charge radius of the pion. This procedure also compensated for the relatively poorer quality of data in this region. The *BABAR* continuous low-mass data permit a direct evaluation, consistent with the constrained method. The very small contribution  $(0.55 \pm 0.01) \times 10^{-10}$  between the  $2\pi$  threshold and 0.3 GeV is evaluated using the extrapolation of the constrained fit to the data between 0.3–0.5 GeV.

The *BABAR* results are given in Table VII in different mass ranges. The upper boundary (1.8 GeV) is chosen in accordance with previous evaluations [2], in which the contribution of the higher energy region was computed using QCD. The contribution in the 1.8–3 GeV range, obtained with the present *BABAR* data, is indeed only  $(0.21 \pm 0.01) \times 10^{-10}$ , thus negligible with respect to the uncertainty in the main region. The contribution from threshold to 1.8 GeV is obtained for the first time from a single experiment:

$$a_\mu^{\pi\pi(\gamma),\text{LO}} = (514.09 \pm 2.22 \pm 3.11) \times 10^{-10}, \quad (41)$$

where the first error is statistical and the second systematic. The total uncertainty is  $3.82 \times 10^{-10}$ , so that the precision of the measurement is 0.74%.

### B. Comparison to other determinations using $e^+e^-$ and $\tau$ data

Direct comparison to the results from other experiments is complicated by two facts: (i)  $e^+e^-$  scan experiments

provide cross section measurements at discrete and unequally spaced energy values, while the ISR method provides a continuous spectrum, (ii) unlike *BABAR*, other experiments do not all cover the complete mass spectrum from threshold up to energies where the contributions become negligible. The latter problem is alleviated by appropriately combining different sets of measurements performed by the same experiment. Where gaps remain, they are filled by using the weighted-average cross section values from the other experiments. This approach has been thoroughly treated in Ref. [7], from which we extract the relevant integrals. The fraction of contributions to the integrals estimated in this way ranges from 3% for KLOE to 11% for CMD-2 (7% for SND), engendering some correlations between the total values (given in the energy range from  $2m_\pi$  to 1.8 GeV).

Correlations between systematic uncertainties have also been taken into account in Ref. [7], particularly for radiative corrections, when combining the results from all experiments. The combination is achieved locally at the cross section level, taking into account possible disagreements leading to an increased uncertainty of the resulting average. The results are summarized in Table VIII and Fig. 56 and allow a direct comparison of all the determinations. They are indeed consistent within the errors, *BABAR* and CMD-2 being almost a factor of 2 more precise than SND and KLOE. Internal discrepancies between the measurements increase the final uncertainty to  $3.2 \times 10^{-10}$ , whereas the ideal value would be  $2.4 \times 10^{-10}$  for fully consistent experiments.

Similarly, the *BABAR* result is compared to determinations using  $\tau$  decays with IB corrections [6] in Table VIII

TABLE VIII. Evaluation of LO hadronic VP  $2\pi$  contributions to the muon magnetic anomaly in the energy range [ $2m_\pi$ , 1.8 GeV] from *BABAR*, other  $e^+e^-$  experiments [7], and  $\tau$  experiments [6] (see text for details). The errors are from both statistical and systematic sources. For the values derived from  $\tau$  decays, a common systematic error of 1.9 is included to account for uncertainties in the isospin-breaking corrections. Note that the combined results are not the weighted average of the different values, but originate from a proper local combination of the respective spectral functions [6,7].

Experiment	$a_\mu^{\pi\pi(y),\text{LO}} (\times 10^{-10})$
<i>BABAR</i>	$514.1 \pm 3.8$
CMD-2	$506.6 \pm 3.9$
SND	$505.1 \pm 6.7$
KLOE	$503.1 \pm 7.1$
Combined $e^+e^-$	$507.8 \pm 3.2$
ALEPH	$508.7 \pm 5.9 \pm 1.9$
CLEO	$514.2 \pm 10.4 \pm 1.9$
OPAL	$526.9 \pm 12.3 \pm 1.9$
Belle	$513.7 \pm 8.2 \pm 1.9$
Combined $\tau$	$515.2 \pm 3.0 \pm 1.9$

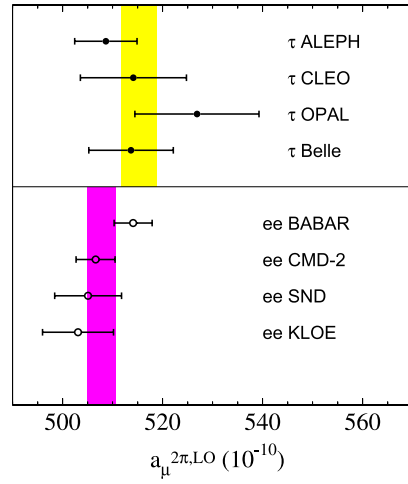


FIG. 56 (color online). The LO hadronic VP  $2\pi$  contributions to the muon magnetic anomaly, evaluated in the  $2m_\pi - 1.8$  GeV range from the present analysis and other analyses using  $e^+e^-$  data [7] and  $\tau$  data [6]. The vertical bands show the values obtained for each data set by combining the respective spectral functions.

and Fig. 56. The agreement is found to be satisfactory, so the *BABAR* data reduces the previous tension between the  $e^+e^-$  and  $\tau$ 's values [2]. Regarding the consistency of all results, it is notable that the four inputs (CMD-2/SND, KLOE, *BABAR*,  $\tau$ ) have completely independent systematic uncertainties.

### C. Impact of this result on the comparison of the Standard Model prediction and the direct measurement of the muon magnetic anomaly

Even though the  $2\pi$  contribution is the dominant part of the hadronic LO VP component in the Standard Model prediction for the muon magnetic anomaly, all the contributions must be evaluated. The *BABAR* experiment has measured most of the relevant cross sections by the ISR method. Except for a few channels still unmeasured, *BABAR* results bring a new level of precision and dominate the picture. We follow here the recent analysis of Ref. [49] that uses all these measurements and those from other experiments. More recently, similar results have been obtained [50].

Adding all contributions (QED, electroweak, hadronic LO VP other than  $2\pi$ , hadronic higher-order VP, hadronic light-by-light [51]) to the present  $2\pi$  result alone, one obtains the predicted value of the muon magnetic anomaly:

$$a_\mu = (11\,659\,186.5 \pm 5.4) \times 10^{-10}, \quad (42)$$

to be compared to the direct measurement [1], slightly updated [52]:

$$a_\mu^{\text{exp}} = (11\,659\,208.9 \pm 6.3) \times 10^{-10}. \quad (43)$$

The experimental value exceeds the prediction by  $(22.4 \pm 8.3) \times 10^{-10}$ , i.e., 2.7 standard deviations. When

the present *BABAR* cross section is combined with all available  $2\pi$  data from  $e^+e^-$  experiments [49], the deviation increases to  $(28.7 \pm 8.0) \times 10^{-10}$ , i.e., 3.6 standard deviations. Although the deviation is not significant enough to claim a departure from the Standard Model, it confirms the trend of earlier results using previous  $e^+e^-$  data [2–4].

## XI. CONCLUSION

The cross sections for the processes  $e^+e^- \rightarrow \mu^+\mu^-(\gamma)\gamma_{\text{ISR}}$  and  $e^+e^- \rightarrow \pi^+\pi^-(\gamma)\gamma_{\text{ISR}}$  have been measured by the *BABAR* experiment, where the additional photon may be produced either by FSR or ISR. Thanks to the properties of the ISR method, the corresponding  $e^+e^- \rightarrow \mu^+\mu^-(\gamma)$  and  $e^+e^- \rightarrow \pi^+\pi^-(\gamma)$  cross sections have been determined from their thresholds to 3 GeV, thus covering completely the interesting region for calculating hadronic vacuum polarization in the  $\pi^+\pi^-$  channel.

For  $e^+e^- \rightarrow \mu^+\mu^-(\gamma)$  the cross section is measured using the  $e^+e^-$  luminosity, while the cross section for  $e^+e^- \rightarrow \pi^+\pi^-(\gamma)$ , for which the highest precision is required, is obtained from the ratio of the radiative  $\pi^+\pi^-(\gamma)\gamma_{\text{ISR}}$  to  $\mu^+\mu^-(\gamma)\gamma_{\text{ISR}}$  mass spectra. In this way the pion results are independent of the  $e^+e^-$  luminosity and important systematic effects cancel. As a major asset of the method, the pion-pair cross section is not sensitive to the model of radiative corrections in the generator used for MC simulation.

The measured absolute  $e^+e^- \rightarrow \mu^+\mu^-(\gamma)\gamma_{\text{ISR}}$  cross section is found to agree with QED at NLO from threshold to 3 GeV, with a precision of 1.1% dominated by the  $e^+e^-$  luminosity determination.

The cross section for  $e^+e^- \rightarrow \pi^+\pi^-(\gamma)$  is obtained for the first time continuously in the energy range from threshold to 3 GeV. Its precision exceeds that of previous experiments in most of this range. The achieved systematic uncertainty is 0.5% in the dominant  $\rho$  region from 0.6 to 0.9 GeV.

Fits of the pion form factor have been performed using a sum of contributions from isovector vector mesons: besides the dominant  $\rho$  resonance and isospin-violating  $\rho - \omega$  interference, three higher states are needed to reproduce the structures observed in the measured spectrum.

The results are in fair agreement with previous data from CMD-2 and SND, but some discrepancies are observed when compared to the KLOE data, particularly on the  $\rho$  peak (3%) and above (up to 6% at 0.95 GeV). These differences exceed the uncertainties quoted by either experiment. The *BABAR* results are in agreement with

the spectral functions derived from  $\tau \rightarrow \nu_\tau \pi^- \pi^0$  data, although some local deviations are seen in the line shape at the 2% level with Belle.

Finally, the *BABAR* results are used as input to the dispersion integral yielding the  $\pi^+\pi^-(\gamma)$  vacuum polarization contribution at LO to the muon magnetic anomaly. This contribution amounts to  $(514.1 \pm 2.2_{\text{stat}} \pm 3.1_{\text{syst}}) \times 10^{-10}$ , the most precise result yet from a single experiment. This result brings the contribution estimated from all  $e^+e^- \rightarrow \pi^+\pi^-(\gamma)$  data combined in better agreement with the  $\tau$  estimate. When adding all other Standard Model contributions to the present  $2\pi$  result, in particular, using all available *BABAR* data on multihadronic processes, the predicted muon magnetic anomaly is found to be  $(11\,659\,186.5 \pm 5.4) \times 10^{-10}$ , which is smaller than the direct measurement at BNL by  $2.7\sigma$ . Adding all previous  $2\pi$  data increases the deviation to  $3.6\sigma$ .

A claim for a breakdown of the Standard Model requires even more precise data, both for the direct anomaly measurement and the hadronic cross sections. But since a deviation of the observed size could be mediated by new physics at a scale of a few 100 GeV, the present direct exploration for new phenomena performed at the Tevatron and the LHC will certainly bring valuable and complementary information.

## ACKNOWLEDGMENTS

We are grateful for the extraordinary contributions of our PEP-II colleagues in achieving the excellent luminosity and machine conditions that have made this work possible. The success of this project also relies critically on the expertise and dedication of the computing organizations that support *BABAR*. The collaborating institutions wish to thank SLAC for its support and the kind hospitality extended to them. This work is supported by the US Department of Energy and National Science Foundation, the Natural Sciences and Engineering Research Council (Canada), the Commissariat à l’Energie Atomique and Institut National de Physique Nucléaire et de Physique des Particules (France), the Bundesministerium für Bildung und Forschung and Deutsche Forschungsgemeinschaft (Germany), the Istituto Nazionale di Fisica Nucleare (Italy), the Foundation for Fundamental Research on Matter (The Netherlands), the Research Council of Norway, the Ministry of Education and Science of the Russian Federation, Ministerio de Ciencia e Innovación (Spain), and the Science and Technology Facilities Council (United Kingdom). Individuals have received support from the Marie-Curie IEF program (European Union) and the A. P. Sloan Foundation (USA).

- [1] G. W. Bennett *et al.* (Muon  $g - 2$  Collaboration), *Phys. Rev. D* **73**, 072003 (2006).
- [2] M. Davier, S. Eidelman, A. Höcker, and Z. Zhang, *Eur. Phys. J. C* **27**, 497 (2003); **31**, 503 (2003).
- [3] M. Davier, *Nucl. Phys. B, Proc. Suppl.* **169**, 288 (2007).
- [4] K. Hagiwara *et al.*, *Phys. Lett. B* **649**, 173 (2007).
- [5] B. Aubert *et al.* (*BABAR* Collaboration), *Phys. Rev. Lett.* **103**, 231801 (2009).
- [6] M. Davier *et al.*, *Eur. Phys. J. C* **66**, 127 (2010).
- [7] M. Davier, A. Hoecker, B. Malaescu, C. Z. Yuan, and Z. Zhang, *Eur. Phys. J. C* **66**, 1 (2010).
- [8] V. N. Baier and V. S. Fadin, *Phys. Lett.* **27B**, 223 (1968).
- [9] A. B. Arbuzov *et al.*, *J. High Energy Phys.* **12** (1998) 009.
- [10] S. Binner, J. H. Kühn, and K. Melnikov, *Phys. Lett. B* **459**, 279 (1999).
- [11] M. Benayoun *et al.*, *Mod. Phys. Lett. A* **14**, 2605 (1999).
- [12] H. Czyż *et al.*, *Eur. Phys. J. C* **33**, 333 (2004).
- [13] B. Aubert *et al.* (*BABAR* Collaboration), *Nucl. Instrum. Methods Phys. Res., Sect. A* **479**, 1 (2002).
- [14] H. Czyż and J. H. Kühn, *Eur. Phys. J. C* **18**, 497 (2001).
- [15] M. Caffo, H. Czyż, and E. Remiddi, *Nuovo Cimento Soc. Ital. Fis. A* **110**, 515 (1997).
- [16] E. Barberio, B. van Eijk, and Z. Was, *Comput. Phys. Commun.* **66**, 115 (1991).
- [17] H. Czyż *et al.*, *Eur. Phys. J. C* **35**, 527 (2004); **39**, 411 (2005).
- [18] T. Sjöstrand, *Comput. Phys. Commun.* **82**, 74 (1994).
- [19] S. Jadach and Z. Was, *Comput. Phys. Commun.* **85**, 453 (1995).
- [20] S. Agostinelli *et al.*, *Nucl. Instrum. Methods Phys. Res., Sect. A* **506**, 250 (2003).
- [21] M. Davier, *Nucl. Phys. B, Proc. Suppl.* **189**, 222 (2009).
- [22] B. Aubert *et al.* (*BABAR* Collaboration), *Phys. Rev. D* **73**, 012005 (2006).
- [23] B. Malaescu, *Nucl. Instrum. Methods Phys. Res.* (to be published).
- [24] K. Nakamura *et al.* (Particle Data Group), *J. Phys. G* **37**, 075021 (2010).
- [25] Yu. M. Bystritskiy *et al.*, *Phys. Rev. D* **72**, 114019 (2005).
- [26] H. Czyż *et al.*, *Eur. Phys. J. C* **39**, 411 (2005).
- [27] T. Kinoshita, *J. Math. Phys. (N.Y.)* **3**, 650 (1962); T. D. Lee and M. Nauenberg, *Phys. Rev.* **133**, B1549 (1964).
- [28] D. Bisello *et al.* (*DM2* Collaboration), *Phys. Lett. B* **220**, 321 (1989).
- [29] Z. Lu and I. Schmidt, *Phys. Rev. D* **73**, 094021 (2006); **75**, 099902 (2007).
- [30] M. Diehl, T. Gousset, and B. Pire, *Phys. Rev. D* **62**, 073014 (2000).
- [31] Private communication from V. Chernyak (BINP, Novosibirsk, Russia).
- [32] See Supplemental Material at <http://link.aps.org/supplemental/10.1103/PhysRevD.86.032013> for files containing the cross section data and their covariance matrices.
- [33] G. J. Gounaris and J. J. Sakurai, *Phys. Rev. Lett.* **21**, 244 (1968).
- [34] G. D'Agostini, *Nucl. Instrum. Methods Phys. Res., Sect. A* **346**, 306 (1994).
- [35] V. M. Aulchenko *et al.* (*CMD-2* Collaboration), *JETP Lett.* **82**, 743 (2005); **84**, 413 (2006); R. R. Akhmetshin *et al.*, *Phys. Lett. B* **648**, 28 (2007).
- [36] M. N. Achasov *et al.* (*SND* Collaboration), *JETP* **103**, 380 (2006).
- [37] F. Ambrosino *et al.* (*KLOE* Collaboration), *Phys. Lett. B* **670**, 285 (2009).
- [38] F. Ambrosino *et al.* (*KLOE* Collaboration), *Phys. Lett. B* **700**, 102 (2011).
- [39] V. Cirigliano, G. Ecker, and H. Neufeld, *Phys. Lett. B* **513**, 361 (2001); *J. High Energy Phys.* **08** (2002) 002.
- [40] A. V. Flores-Baéz *et al.*, *Phys. Rev. D* **74**, 071301 (2006); A. Flores-Tlalpa *et al.*, *Nucl. Phys. B, Proc. Suppl.* **169**, 250 (2007).
- [41] A. V. Flores-Baéz *et al.*, *Phys. Rev. D* **76**, 096010 (2007).
- [42] M. Benayoun *et al.*, *Eur. Phys. J. C* **72**, 1848 (2012).
- [43] F. Jegerlehner and R. Szafron, *Eur. Phys. J. C* **71**, 1632 (2011).
- [44] S. Schael *et al.* (*ALEPH* Collaboration), *Phys. Rep.* **421**, 191 (2005).
- [45] S. Anderson *et al.* (*CLEO* Collaboration), *Phys. Rev. D* **61**, 112002 (2000).
- [46] M. Fujikawa *et al.* (*Belle* Collaboration), *Phys. Rev. D* **78**, 072006 (2008).
- [47] C. Bouchiat and L. Michel, *J. Phys. Radium* **22**, 121 (1961).
- [48] S. J. Brodsky and E. de Rafael, *Phys. Rev.* **168**, 1620 (1968).
- [49] M. Davier, A. Hoecker, B. Malaescu, and Z. Zhang, *Eur. Phys. J. C* **71**, 1515 (2011).
- [50] K. Hagiwara *et al.*, *J. Phys. G* **38**, 085003 (2011).
- [51] J. Prades, E. de Rafael, and A. Vainshtein, *Lepton Dipole Moments*, edited by B. L. Roberts and W. J. Marciano, Advanced Series on Directions in High Energy Physics Vol. 20 (World Scientific, Singapore, 2009).
- [52] A. Hoecker and W. Marciano, “The Muon Anomalous Magnetic Moment,” in Ref. [24].